MAX-PLANCK-INSTITUT
FÜR METEOROLOGIE

Sedimentation Effects in Subtropical Stratocumulus

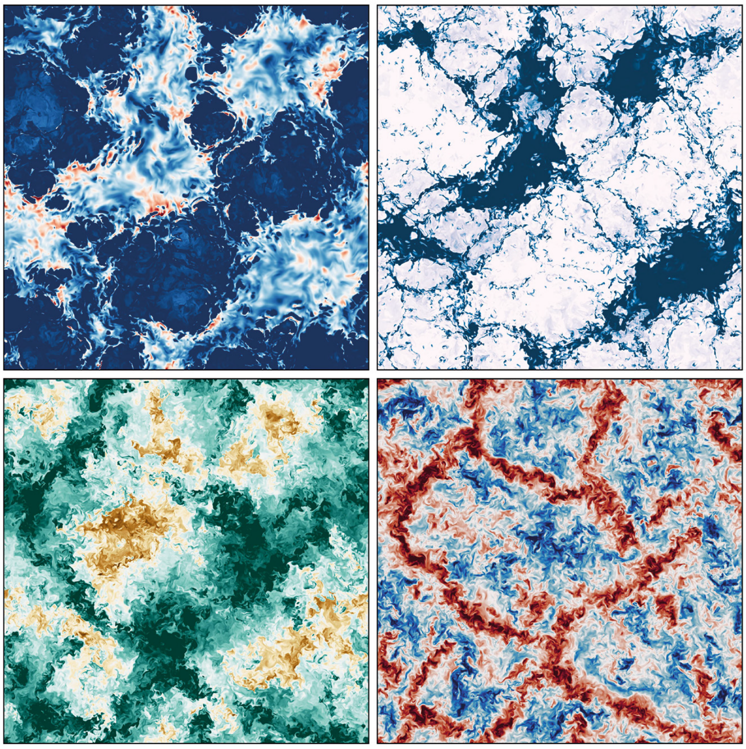

Raphael Pistor

Hamburg 2026

Berichte zur Erdsystemforschung 297
Reports on Earth System Science 2026

Hinweis

Die Berichte zur Erdsystemforschung werden vom Max-Planck-Institut für Meteorologie in Hamburg in unregelmäßiger Abfolge herausgegeben.

Sie enthalten wissenschaftliche und technische Beiträge, inklusive Dissertationen.

Die Beiträge geben nicht notwendigerweise die Auffassung des Instituts wieder.

Die "Berichte zur Erdsystemforschung" führen die vorherigen Reihen "Reports" und "Examensarbeiten" weiter.

Anschrift / Address

Max-Planck-Institut für Meteorologie
Bundesstrasse 53
20146 Hamburg
Deutschland

Tel./Phone: +49 (0)40 4 11 73 - 0
Fax: +49 (0)40 4 11 73 - 298

name.surname@mpimet.mpg.de
www.mpimet.mpg.de

Notice

The Reports on Earth System Science are published by the Max Planck Institute for Meteorology in Hamburg. They appear in irregular intervals.

They contain scientific and technical contributions, including PhD theses.

The Reports do not necessarily reflect the opinion of the Institute.

The "Reports on Earth System Science" continue the former "Reports" and "Examensarbeiten" of the Max Planck Institute.

Layout

Bettina Diallo and Norbert P. Noreiks
Communication

Copyright

Photos below: ©MPI-M
Photos on the back from left to right:
Christian Klepp, Jochem Marotzke,
Christian Klepp, Clotilde Dubois,
Christian Klepp, Katsumasa Tanaka

Raphael Pistor
Mainz, Deutschland

Max-Planck-Institut für Meteorologie
The International Max Planck Research School on Earth System Modelling
(IMPRS-ESM)
Bundesstrasse 53
20146 Hamburg

Tag der Disputation: 12. Dezember 2025

Folgende Gutachter empfehlen die Annahme der Dissertation:
Prof. Dr. Juan Pedro Mellado
Prof. Dr. Bjorn Stevens

Vorsitzender des Promotionsausschusses:
Prof. Dr. Hermann Held

Dekan der MIN-Fakultät:
Prof. Dr.-Ing. Norbert Ritter

Titelgrafik: *The title figure depicts horizontal cross-sections of a DNS-simulated stratocumulus cloud layer, illustrating the distributions of temperature, liquid water content, water vapor, and vertical velocity distribution (from left to right, top to bottom).*

Berichte zur Erdsystemforschung / Max-Planck-Institut für Meteorologie 297
Reports on Earth System Science / Max Planck Institute for Meteorology 2026

ISSN 1614-1199 - doi: 0.17617/2.3691281

Sedimentation Effects in Subtropical Stratocumulus

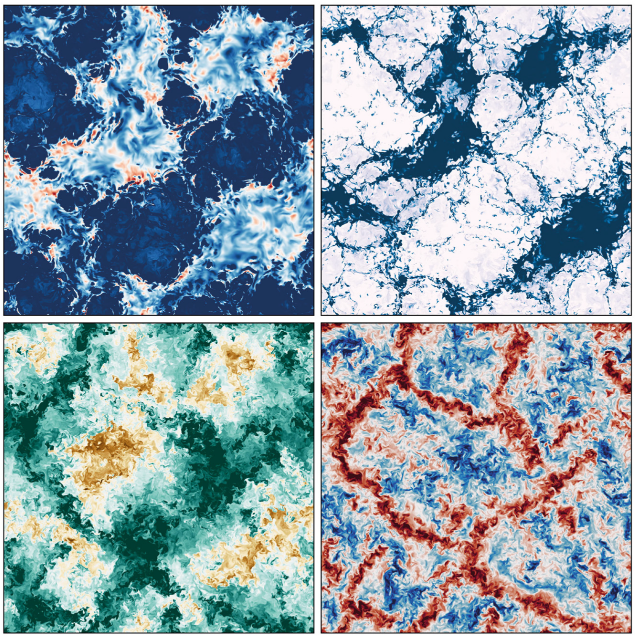

Raphael Pistor

Hamburg 2026

Raphael Pistor

Sedimentation Effects in Subtropical Stratocumulus

ABSTRACT

Stratocumulus clouds are climatically important because their widespread presence over subtropical oceans and their high albedo help to cool Earth's surface. Their structure and longevity are governed by turbulence dynamics, particularly the entrainment of warm, dry air from the free troposphere. Microphysical processes, such as droplet sedimentation, can modify these dynamics by reducing entrainment, though the magnitude of this effect remains uncertain. Representing these turbulence-entrainment interactions is particularly challenging due to the wide separation of length scales over which turbulence operates. This dissertation addresses this challenge by quantifying the effects of droplet sedimentation on turbulence and entrainment under varying environmental conditions, including those associated with climate change, using direct numerical simulations at meter-scale resolution that span the full boundary layer depth.

In my first study, I show that at a vertical grid spacing of 1.1 m (reference Reynolds number: $\mathrm{Re}_0 = 12500$), sedimentation reduces the mean entrainment velocity by at least 20%. At this Reynolds number, sedimentation has a larger effect on entrainment than further increases in Reynolds number, suggesting that turbulence and sedimentation effects can be disentangled. Interestingly, turbulence intensity increases even as mean entrainment decreases. To reconcile this apparent contradiction, I use the flux-jump relation to decompose mean fluxes of the liquid-water static energy, showing that as sedimentation strength intensifies, the magnitude of the sedimentation flux grows faster than the turbulent flux, effectively compensating for the increase in turbulent flux. To explain the increase in turbulence intensity, I show that sedimentation enhances the contrast between descending dry, warm air in cloud holes and moist, cold air in cloud cores. This enhanced contrast intensifies evaporative cooling near cloud-hole edges, accelerates downdrafts, and redistributes moisture more evenly between the cloud and subcloud layers. These findings highlight the importance of resolving meter-scale turbulence in both cloud and subcloud layers to understand how moisture redistribution shapes turbulence organization.

In my second study, I explore how sedimentation interacts with low-cloud adjustment mechanisms in the context of warming-related environmental changes, specifically: (i) thermodynamic warming, (ii) reduced downwelling longwave radiation, and (iii) increased inversion strength. A moderate Reynolds number ($\mathrm{Re}_0 = 5000$) simulation reproduces the sign and approximate magnitude of low-cloud responses reported in existing large-eddy simulation (LES) studies (Bretherton et al., 2013), demonstrating its potential as a turbulence-parameterization-free modeling tool. Sedimentation effects are comparable in magnitude to those of adjustment mechanisms, with the potential for amplifying and compensating interactions. The relative low-cloud thinning response is robust and independent of sedimentation strength, but the absolute cloud amount depends on sedimentation strength, indicating that droplet sedimentation is a non-negligible source of uncertainty in cloud feedbacks under warming scenarios.

ZUSAMMENFASSUNG

Stratocumulus-Wolken sind klimatisch bedeutsam, da sie über Ozeanen weit verbreitet sind und durch ihre hohe Albedo zur Kühlung der Erdoberfläche beitragen. Ihre Struktur und Langlebigkeit werden durch turbulente Dynamik bestimmt, insbesondere durch Entrainment warmer, trockener Luft aus der freien Troposphäre. Mikrophysikalische Prozesse wie Sedimentation können diese Dynamik durch eine Verringerung der Entrainmentrate verändern, wobei das Ausmaß dieses Effekts ungewiss bleibt. Die Darstellung dieser Wechselwirkungen zwischen Turbulenz und Entrainment ist aufgrund der vielen Längenskalen, auf denen Turbulenz wirkt, besonders schwierig. Diese Dissertation befasst sich mit dieser Herausforderung, indem sie die Auswirkungen von Sedimentation auf Turbulenzen unter Einbeziehung verschiedenen Umweltbedingungen, einschließlich derjenigen, die mit dem Klimawandel zusammenhängen, quantifiziert. Dies geschiet mithilfe direkter numerischer Simulationen mit einer Auflösung im Meterbereich, die die gesamte Grenzschicht abdecken.

In meiner ersten Studie zeige ich, dass bei einem vertikalen Gitterabstand von 1.1 m (Referenz-Reynolds-Zahl: $\mathrm{Re}_0 = 12500$) die Sedimentation die mittlere Mitreißgeschwindigkeit (auch mittlere Entrainmentgeschwindigket) um mindestens 20% verringert. Bei dieser Reynolds-Zahl hat die Sedimentation einen größeren Einfluss auf die Mitreißgeschwindigkeit als eine weitere Erhöhung der Reynolds-Zahl, was darauf hindeutet, dass Turbulenz- und Sedimentationseffekte voneinander getrennt betrachtet werden können. Interessanterweise nimmt die Turbulenzintensität sogar zu, wenn die mittlere Entrainmentrate abnimmt. Um diesen offensichtlichen Widerspruch aufzulösen, verwende ich die Flux-Jump-Beziehung, um die liquid-water static energy zu zerlegen, und zeige, dass mit zunehmender Sedimentationsstärke die Größe des Sedimentationsflusses schneller wächst als der turbulente Fluss, wodurch der Anstieg des turbulenten Flusses kompensiert wird. Um die Zunahme der Turbulenzintensität zu erklären, zeige ich, dass die Sedimentation den Kontrast zwischen der absteigenden trockenen, warmen Luft in Wolkenlöchern und der feuchten, kalten Luft in Wolkenkernen verstärkt. Dieser verstärkte Kontrast intensiviert die Verdunstungskühlung in der Nähe der Wolkenlochränder, beschleunigt die Abwinde und verteilt die Feuchtigkeit gleichmäßiger zwischen der Wolke und den Schichten unterhalb der Wolke. Diese Ergebnisse unterstreichen, wie wichtig es ist, Turbulenzen im Meterbereich sowohl in der Wolke als auch in den Schichten unterhalb der Wolke aufzulösen, um zu verstehen, wie die Feuchtigkeitsverteilung die Turbulenzorganisation beeinflusst.

In meiner zweiten Studie untersuche ich, wie Sedimentation auf Anpassungsmechanismen niedriger Wolken im Zusammenhang mit klimawandelbedingten Umweltveränderungen reagiert und mit diesen interagiert, insbesondere: (i) thermodynamische Erwärmung, (ii) reduzierte nach unten gerichtete langwellige Strahlung und (iii) erhöhte Inversionsstärke. Eine Simulation mit moderater Reynolds-Zahl ($\mathrm{Re}_0 = 5000$) reproduziert das Vorzeichen und die ungefähre Größe der in bestehenden Large-Eddy-Simulationsstudien (LES) (Bretherton u. a., 2013) berichteten Reaktionen niedriger Wolken und demonstriert damit ihr Potenzial als turbulenzparametrisierungsfreies Modellierungswerkzeug. Die Auswirkungen der Sedimentation sind in ihrer Größenord-

nung mit denen der Anpassungsmechanismen vergleichbar, mit dem Potenzial für verstärkende und kompensierende Wechselwirkungen. Die Mechanismen selbst reagieren ebenfalls nicht empfindlich auf Sedimentation. Wie in der ersten Studie gezeigt, nimmt diese Empfindlichkeit bei höheren Reynolds-Zahlen wahrscheinlich zu, was darauf hindeutet, dass die Sedimentation von Tröpfchen einen nicht zu vernachlässigenden Beitrag zur Unsicherheit der Wolkenrückkopplung unter Erwärmungsszenarien leistet.

PUBLICATIONS

The following first-author publications are part of this dissertation and are included in the appendices:

Appendix A

Pistor, R. & Mellado, J. P. (2025). Resolving droplet sedimentation effects in stratocumulus clouds. Journal of Advances in Modeling Earth Systems, 17(8), e2025MS004966.

Appendix B

Pistor, R. & Mellado, J. P. Linking Droplet Sedimentation to Stratocumulus Adjustment Mechanisms: A Finer Look. *In preparation.*

ACKNOWLEDGEMENTS

It's worth taking a moment to pause and reflect on the strange, winding journey that is a PhD. While structured and formal in many regards, it is also filled with the informal: emotions, self-discovery, and people who make the endeavor meaningful. Some of whom I'd like to acknowledge.

I first want to thank Juan Pedro for being an outstanding supervisor. Over the past four years, I learned a great deal through his example: his meticulous attention to detail, his strive towards elegance in science, and his artistry and patience in teaching. Working with him has been both humbling and rewarding.

When I began this work, the return to offices after Covid was still provisional. Since then, the community on the 16th floor has really bloomed. It's been a pleasure to witness colleagues like Raphaela, Kay, and Victor cultivate their own paths. Within that space, a heartfelt thank-you goes to Ian, for sharing an office jungle and being a companion throughout these years. What I'll carry most from my time at the MPI is the experience of having been part of a buzzing hive of bright and kind people—thank you all. The close-knit atmosphere owes much to people like Antje, who made me feel at home from day one, and to Cornelia, Michaela, Florian, and Sabine, whose work behind the scenes kept things running smoothly. I'm also grateful to Moritz G., Malena, and Helene for their thoughtful feedback on this dissertation. Thanks to Dallas and Jochem for a fruitful education in academic writing, to Bjorn and Stefan for keeping our panel meetings honest and open, and to Johanna and Alexa for their role on the committee.

In the broader context, I am aware and thankful of the privilege I've had in being able to pursue research. To study in a country that upholds stable institutions and offers free education is a privilege built on many layers of support—from cleaning staff to administrators, directors, politicians, journalists, bus drivers, and activists.

Outside the academic bubble, I owe much to my friends. To Alex, for the years. To Christine, Kubi, Ryan and Nils, and many others, for our ritual game and dinner nights. To Luca (S. & K.) for meaningful conversations about life's bigger picture. To Hernán, for inspiring me to stay committed with analog photography. To Gualtiero, for rekindling a remembrance of literature and time. And to Jan Niklas, for countless cycling adventures... trying my best to hold his wheel.

My upbringing gave me a broad cultural perspective, and I thank my parents for that foundation and sensitivity. It has kept me centered. This journey was shared with, each in our own way, my brothers Lucas and Tobias. To my grandmother, Viola, for being a close friend. Much of what I value and care about, I can relate to her. And of course, to my partner, Malena: these last years wouldn't have been the same without her presence and care. Through our shared values, travels, and connections, it's been a joy to grow together.

CONTENTS

Part I

UNIFYING ESSAY

1

MOTIVATION

The sensitivity of the Earth's climate system to perturbations in its radiation balance—whether driven by anthropogenic or natural variability—remains a central focus of climate science due to its profound socio-economic implications (Cooke et al., 2014; Rennert et al., 2022; Christensen et al., 2022; Bilal and Känzig, 2024; Kotz et al., 2024; Kallis et al., 2025). A central metric in this context is equilibrium climate sensitivity (ECS): the steady-state response in global surface temperature in response to a doubling of pre-industrial atmospheric CO_2 (Nuijens and Siebesma, 2019). A key contributor to ECS is low-latitude stratocumulus clouds. These clouds cover vast areas of the subtropical oceans and reflect a large portion of incoming solar radiation, thereby exerting a cooling effect on Earth's radiation balance (Wood, 2012). Through various lines of evidence, researchers have sought to quantify how changes in stratocumulus clouds can amplify or dampen climate sensitivity (Sherwood et al., 2020; Christensen et al., 2022), showing that cloud coverage is highly sensitive to environmental conditions like sea surface temperature and large-scale subsidence. Their environmental sensitivity has sparked interest in geoengineering approaches, particularly aerosol-based approaches like marine cloud brightening, as a potential means for mitigating climate change (Latham, 1990; Feingold et al., 2024; Hoffmann et al., 2024).

Despite their critical role, the magnitude of stratocumulus cloud responses to changing environmental conditions remains uncertain, largely due to the complex, multiscale interactions that govern these clouds. A central constraint lies in our ability to represent small-scale processes like turbulent mixing and cloud-top entrainment, which together control boundary layer depth and cloud thickness. This is especially true at the cloud-top interface, where sharp temperature, humidity, and density gradients control turbulent mixing between the cloud and environmental air (Wood, 2012). Further complicating matters, microphysical processes like droplet sedimentation have been shown to meaningfully alter cloud properties (Bretherton et al., 2007; Lozar and Mellado, 2017; Schulz and Mellado, 2019). Yet most existing studies rely on coarse-resolution models that use simplified parameterizations or are restricted to domains too limited to encompass the full boundary layer. This gap in representation hinders our ability to predict how stratocumulus clouds will respond to future climate scenarios.

To address these challenges, this dissertation investigates how droplet sedimentation influences turbulence and entrainment in stratocumulus clouds, and how these processes affect cloud adjustments under warming conditions. To quantify these effects, direct numerical simulations at meter-scale resolution are used, explicitly resolving both small-scale turbulent mixing and larger-scale moisture transport processes.

2

BACKGROUND

This chapter provides the scientific background for this dissertation. It begins with an overview of the structure and key processes of the stratocumulus-topped boundary layer (STBL), followed by a discussion of how aerosol-cloud interactions lead to sedimentation and entrainment feedbacks that vary cloud liquid water. I then describe how process-resolving models, specifically direct numerical simulations, can be used to better understand small-scale turbulent processes in the STBL. The chapter closes by zooming back out to the large-scale perspective with a brief review of stratocumulus adjustment mechanisms in a warming climate. The subsequent chapters present the main findings of this dissertation, followed by an overall summary.

2.1 STRATOCUMULUS-TOPPED BOUNDARY LAYER

Stratocumulus clouds extend over nearly one-fifth of the globe, often forming sheets over oceans that span hundreds to thousands of kilometers (Wood, 2012). Their climatic importance arises from this vast horizontal extent and their strong albedo (Hartmann et al., 1992), reflecting up to 60% of incoming solar radiation back to space (Schween et al., 2022), far more than the darker ocean below, which reflects only about 6% (Payne, 1972). Even small variations in coverage can offset the warming expected from a doubling in atmospheric carbon dioxide (Randall et al., 1984). Forming at low altitudes, stratocumulus clouds are of similar temperature as the surface and therefore emit nearly the same amount of longwave radiation, unlike higher, colder clouds that trap outgoing longwave radiation and warm the planet through the greenhouse effect. Combined, these shortwave and longwave properties allow stratocumulus clouds to effectively mediate Earth's radiation balance by cooling the global-mean surface temperature (Hartmann and Short, 1980; Klein and Hartmann, 1993; Wood, 2012).

The environmental conditions conducive to stratocumulus cloud formation are typically found in regions with pronounced thermal contrasts between the surface and the atmosphere, such as coastal upwelling zones and storm tracks (Stevens, 2005). Under such conditions, the STBL is compressed to a depth of about 1 km, with the cloud layer ranging from $200 - 400$ m in thickness (Wood, 2012). Evaporation from the ocean provides a continuous source of moisture through boundary-layer mixing, making stratocumulus clouds relatively uncommon over land. Strong stratification in such environments helps preserve the large-scale structure of the cloud deck intact, whereas equatorward advection over warmer waters and weaker subsidence allows convective eddies to grow vigorous enough to penetrate the inversion, deepen the cloud, and gradually break up the cloud deck into scattered shallow cumulus clouds (Nicholls, 1984; Bretherton, 1997; Bony et al., 2004; Erfani et al., 2022). These favorable conditions are typically found along the

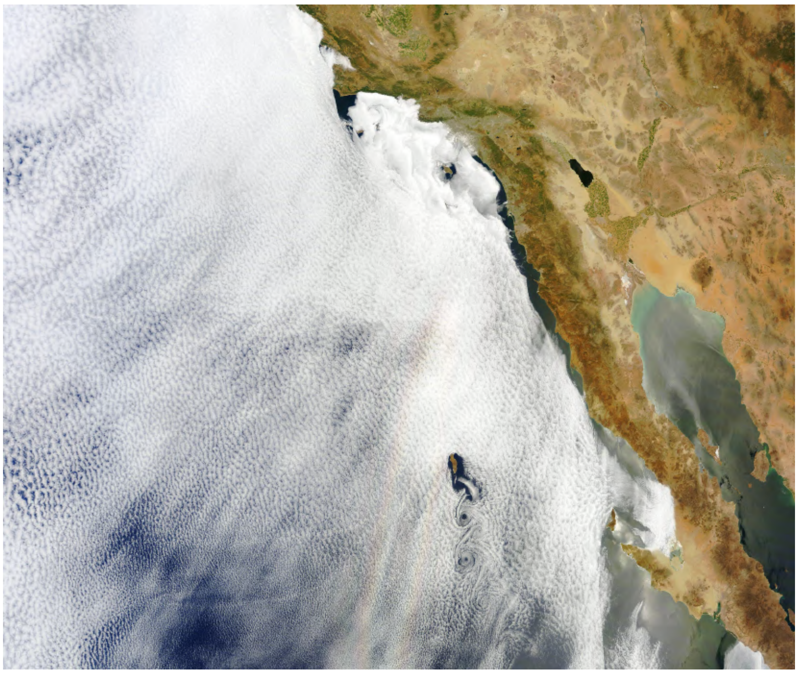

Figure 2.1: Stratocumulus clouds over the Pacific Ocean near Baja California, Mexico. Credit: NASA Goddard Space Flight Center, Terra satellite (NASA, 2012).

eastern ocean basins of the subtropical highs. In these regions, large-scale subsidence from the descending branch of the Hadley circulation overlies coastal upwelling regions, which produce cold sea-surface temperatures (SST) (Wood, 2012; Muhlbauer et al., 2014). Structurally, the STBL consists of a cold, moist layer that includes both a subcloud and a cloud layer, and is capped by a warm, dry free troposphere (Wood, 2012).

Within the STBL, meter- and submeter-scale processes drive the turbulence that sustains the cloud layer. Cloud formation begins when surface winds lift moisture past the lifting condensation level, saturating air parcels and forming liquid water droplets, which then immediately emit longwave radiation (Paluch and Lenschow, 1991). Inside the newly formed cloud, this radiation is nearly isotropic, resulting in a net radiative flux close to zero. At the cloud boundaries, especially at the top where incoming longwave radiation is low, the net flux causes substantial cooling (Caldwell and Bretherton, 2009). Radiative cooling is most intense in the upper meters of the cloud, with cooling rates on the order of $5 - 10$ K h^{-1} (Larson et al., 2007). The resulting convective instability at the cloud top drives turbulent mixing and condensation, which organizes into large eddies that act as conveyor belts for moisture transport, ultimately sustaining the cloud layer with liquid water (Moeng et al., 1996; Bretherton and Wyant, 1997). This feature of cloud-top-generated turbulence distinguishes the STBL from other boundary-layer cloud regimes, where turbulence is typically surface-driven. It also explains why stratocumulus clouds are confined to low altitudes: at higher altitudes, the radiative-cooling-driven turbulence can no longer sustain moisture transport throughout the STBL (Bretherton, 1997).

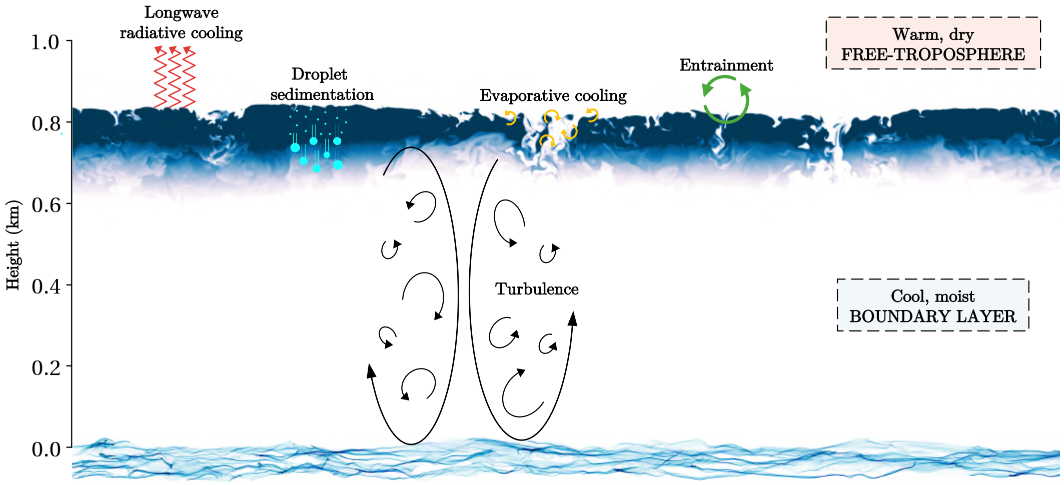

Figure 2.2: Schematic of the vertical structure and main processes in the marine stratocumulus-topped boundary layer. In the cloud deck, darker blue shading indicates higher liquid water content, based on DNS output from this study at a Reynolds number of 12500. Figure adapted from Wood, 2012.

In addition to radiative effects, evaporative cooling creates convective instability that generates turbulence and filamentary structures of varying sizes along cloud boundaries (Lozar and Mellado, 2015a). Evaporative cooling is a small-scale process that occurs when air containing water droplets mixes with unsaturated environmental air. Through a process known as buoyancy reversal, this mixing renders the resulting air parcel negatively buoyant relative to its surroundings, setting it into motion (Mellado, 2010). The effective cooling rate depends on environmental factors, particularly the humidity contrast and the mixing rate between the two air masses (Deardorff, 1980). Historically, it was proposed that evaporative cooling could trigger a feedback loop, termed cloud-top entrainment instability, in which turbulence generated would lead to further mixing, more evaporation, and eventually cloud desiccation (Randall, 1980). However, observational and model support for this feedback is lacking (Albrecht et al., 1985; Kuo and Schubert, 1988; Wang and Albrecht, 1994; Gerber et al., 2005; Yamaguchi and Randall, 2008). Moreover, evaporative cooling rates are typically an order of magnitude smaller than radiative cooling rates, since they are limited by transport processes at the molecular level, which tend to be slow. For this reason, cloud-top dynamics are not controlled by evaporative cooling alone; nevertheless, it remains a key factor in regulating turbulence at localized scales.

The STBL is best understood as a balance between processes such as cloud-top radiative cooling, which generates turbulence that sustains the cloud by transporting moisture upward, and entrainment, which introduces air from the free troposphere, warming and drying the cloud. Entrainment is typically considered a one-way mixing process at the cloud top, where it draws warm, dry air from the free troposphere into the turbulent STBL (Mellado, 2017). This process is quantified by the mean entrainment velocity $w_e = \mathrm{d}z_i/\mathrm{d}t - \langle w \rangle_{z_i}$, where z_i is the inversion height and $\langle w \rangle_{z_i}$ represents the background subsidence velocity (Lilly, 1968). It is a key determinant of boundary layer growth and cloud longevity. Combined with surface convective heating, in-cloud latent heating, and wind shear, these processes modulate turbulence levels within the STBL (Hogan et al., 2009; Mellado, 2010; Malinowski et al., 2013; De Roode et al., 2016; Kopec et al., 2016; Haghshenas and Mellado, 2019; Schulz and Mellado, 2019; Fodor et al., 2022). The vertical structure and key processes of the STBL are illustrated in Figure. 2.2.

One of the main challenges in understanding STBL dynamics lies in how turbulence and other processes interact across the wide range of interconnected spatial scales. For instance, turbulence is initiated by processes such as radiative and evaporative cooling, and then subsequently organize into larger coherent structures, eventually forming boundary-layer eddies. Turbulence then promotes vertical mixing and helps homogenize the STBL, producing well-mixed profiles of moisture and energy that connect the surface to the cloud top. At any point in the development of turbulence, energy continuously cascades back down to progressively smaller scales, ultimately dissipating as thermal energy at the Kolmogorov scale through viscous effects (Richardson, 1920). Particularly challenging are the sharp gradients in temperature, humidity, and density that occur over a layer as thin as a few tens of meters near the cloud top, where longwave radiative cooling strengthens the temperature inversion, also known as the capping inversion (Kurowski et al., 2009; Wood, 2012; Mellado, 2017). In this way, the STBL encompasses motions spanning several orders of magnitude: from kilometer-scale energy-containing motions, to meter-scale turbulence, down to submillimeter dissipation scales and micrometer droplet processes (Khain and Pinsky, 2018). Representing this range of scales is further compounded by the experimental and practical challenges of obtaining fine-resolution observational data. Taken together, the STBL is characterized by the interplay between small-scale mixing and larger boundary-layer dynamics.

2.2 AEROSOL–CLOUD INTERACTIONS AND LINKS TO SEDIMENTATION

The reflectivity of stratocumulus clouds is determined not only by macrophysical properties, such as cloud horizontal extent and thickness, but also by microphysical processes that unfold at the droplet scale. Microphysical processes govern droplet formation and growth, and their sensitivity to ambient aerosol concentrations introduces an additional layer of complexity to our physical understanding of stratocumulus clouds. As a starting point, increases in aerosol concentrations supply additional cloud condensation nuclei, leading to higher cloud droplet number concentrations and redistributing the same liquid water over more numerous but smaller droplets (Twomey, 1974). By assuming cloud water amount and coverage remain unchanged, aerosol-driven increases in droplet concentrations increase the total droplet surface area, thereby brightening the cloud. Therefore, changes in mean droplet number and size *directly* alter the way clouds reflect and absorb sunlight. This instantaneous effect, known as the Twomey effect, produces a negative radiative forcing on the climate (Twomey, 1977). For decades, the aerosol imprint on the atmosphere of the Twomey effect has been made visible in brightened cloud lines appearing downwind of ship tracks, wildfires, and volcanoes. Observational and modeling evidence suggests that anthropogenic aerosols, emitted by human activities and dispersed globally through circulation, have contributed a net global cooling of approximately -1.3 ± 0.7 W m^{-2} (Forster et al., 2023), with low clouds responsible for about -1.0 W m^{-2} of this effect (Diamond et al., 2020).

This has motivated interest in deliberate aerosol seeding of clouds as a potential, albeit temporary, climate mitigation measure (Latham, 1990; Glassmeier et al., 2021; Haywood et al., 2023; Hoffmann et al., 2024). One proposed method, marine cloud brightening, involves spraying saltwater at the surface, where it evaporates into fine particles by convection to the cloud layer. The economic feasibility, risks, and social costs of these interventions are only beginning to be explored (Diamond et al., 2022; Feingold et al., 2024; Bronsther and Xu, 2025; Gristey and Feingold, 2025). However, aerosol-cloud interactions extend beyond simple brightening. They can also modify cloud liquid water, precipitation, dynamics, and cloud lifetime in complex ways and sometimes competing ways. Therefore, quantifying the anthropogenic effect on climate remains challenging, as cloud amount adjustments can be positive or negative depending on regional meteorological conditions. These interactions cause macrophysical and microphysical signals to become intertwined (Coakley Jr and Walsh, 2002; Stevens and Feingold, 2009; Rosenfeld et al., 2019; Christensen et al., 2020; Toll et al., 2019; Wood, 2021).

Cloud liquid water adjustments that emerge through modifications to the droplet size distribution are categorized as *indirect* aerosol-cloud interactions. These adjustments are difficult to constrain in measurements, as aerosol concentrations vary greatly in space and time compared to greenhouse gases (Manavi et al., 2025). Indirect effects are of particular interest because they can potentially offset the Twomey effect on cloud albedo (Possner et al., 2020; Glassmeier et al., 2021). Stratocumulus regimes are often distinguished by background aerosol number concentrations: precipitating clouds (pristine, $\approx 20 - 50$ cm^{-3}) and non-precipitation clouds (polluted, > 130 cm^{-3}) (Chun et al., 2023). In pristine precipitating regimes, aerosol perturbations reduce the efficiency of rain droplet formation through collision-coalescence and suppress drizzle, leading to positive liquid water adjustments (Albrecht, 1989; Pincus and Baker, 1994; Xue and Feingold, 2006; Sandu et al., 2008). If this were the only response, clouds would always thicken as aerosol concentrations increase. Yet measurements in marine stratocumulus clouds, including ship tracks, often show the opposite (Ackerman et al., 2000; Lebsock et al., 2008; Christensen and Stephens, 2011; Toll et al., 2019; Diamond et al., 2020).

Cloud liquid water adjustments can be negative, especially in polluted, non-precipitating regimes (Gryspeerdt et al., 2019). In such conditions, precipitation suppression is weak, and the response stems from feedbacks tied to entrainment events, particularly the accelerated evaporation of smaller and more numerous droplets in the presence of dry air aloft. A multitude of mechanisms have been identified. The first is the evaporation-entrainment feedback: higher aerosol concentrations increase the droplet number, producing smaller droplets with greater curvature and shorter evaporation timescales (Wang et al., 2003; Xue and Feingold, 2006). The resulting evaporative cooling generates negatively buoyant air at the cloud top, intensifying entrainment and thinning the cloud (Stevens et al., 1998; Wood, 2007). A recent study on Arctic mixed-phased clouds also suggests that smaller droplets shift the peak of radiative cooling upward, which in turn increases cloud-top entrainment (Williams and Igel, 2021; Igel, 2024).

A third mechanism, referred to as the sedimentation-entrainment feedback, involves droplet sedimentation, or the rate at which water droplets fall under gravity. Larger droplets fall faster because their lower surface-area-to-weight ratios reduce air resistance. For droplets with radii of $10 - 30\ \mu\mathrm{m}$, sedimentation velocities are comparable to typical mean entrainment velocities, which have been estimated to be in the range $3.9 - 4.7\ \mathrm{mm\ s}^{-1}$ (Faloona et al., 2005; Stevens et al., 2003). Sedimentation acts as a proxy for aerosol concentration because, at higher aerosol concentrations, droplets become smaller and lighter, causing them to fall more slowly (Shaw, 2003). This increased suspension time makes them more susceptible to turbulent updrafts. As sedimentation velocities decrease, more liquid water is retained near the cloud top in the form of smaller droplets, where mixing with dry free-tropospheric air increases the likelihood of evaporation (Ackerman et al., 2004; Bretherton et al., 2007; Ackerman et al., 2009; Hill et al., 2009; Lozar and Mellado, 2014). Although small in magnitude, this downward flux of liquid water due to sedimentation is dynamically important to the STBL because it can counteract the upward flux associated with entrainment mixing (Lozar and Mellado, 2017). Indeed, Schulz and Mellado, 2019 showed that the strength of entrainment reduction with increasing sedimentation strength is sufficient to offset the increase in entrainment produced by wind shear. Diminished entrainment warming subsequently fosters a cooler, moister, and more coupled STBL (Hoffmann et al., 2020).

While there is consensus on the mechanisms through which sedimentation reduces cloud-top entrainment (Wood, 2012; Ackerman et al., 2009; Lozar and Mellado, 2017; Schulz and Mellado, 2019), important gaps remain. Notably, the magnitude of entrainment reduction by sedimentation, a question examined in detail in Chapter 3. Another gap is the impact of sedimentation on turbulence within both the cloud and boundary layer. One mechanism is precipitation suppression, which limits the stabilizing effect in the subcloud layer by preventing evaporative cooling during rainfall (Pincus and Baker, 1994; Stevens et al., 1998; Chun et al., 2023). Another possibility is that sedimentation redirects evaporation into downdrafts, resulting in generating turbulence in those regions (Stevens et al., 1998; Bretherton et al., 2007; Lozar and Mellado, 2017). In this regard, simulations have shown mixed results when it comes to commonly-used indicators of turbulence intensity, such as the vertical velocity variance: some report an increase in variance (Bretherton et al., 2007; Ackerman et al., 2009), while others observe a decrease (Hill et al., 2009).

A thorough understanding of how sedimentation affects both the mean entrainment velocity and turbulence is thus needed. These gaps motivate the use of models capable of resolving fine-scale turbulent processes across the full STBL domain.

2.3 PROCESS-RESOLVING MODELS: DNS

This section outlines the challenges of modeling cloud-turbulence interactions and introduces direct numerical simulations (DNS) as a well-suited tool for tackling these complexities.

Since the advent of global circulation models (GCMs) in the 1960s, climate modeling has matured considerably. While the fundamental scientific concepts related to climate change, whether anthropogenic or natural, are now well established, certain components, including cloud-aerosol interactions, turbulence and boundary layer dynamics, storm-resolving models, and coupling of climate with human systems for socioeconomic implications (Cooke et al., 2014; Rennert et al., 2022), remain in their relative youth. Reducing the physical and numerical uncertainties in these areas is critical for preparing reliable climate projections, which would then form the basis for effective climate mitigation and adaptation strategies. Even with the current advances in computational power, as well as those anticipated in the foreseeable future, the task of resolving the full spectrum of the scales involved in cloud formation within a single model remains impossible. This does not mean, however, that efforts to simulate and investigate clouds such as stratocumulus are in vain. Rather, climate system models and process-resolving models occupy distinct regions on the plane of spatial and temporal scales, with areas of overlap between them. While no single model can represent all scales simultaneously, taken together they yield a more complete picture of the climate system.

At the larger end of the spatiotemporal spectrum, GCMs provide a global representation of the climate system, making them useful for understanding and predicting atmospheric motions across meso-, synoptic-, and global horizontal length scales. However, many processes unfold at scales smaller than GCM grid spacings, necessitating parameterization and motivating continued model development. In the last decade, advances in high-performance computing have borne a new generation of models, global cloud resolving models (GCRMs), which can explicitly simulate the growth and evolution of cloud systems (Schär et al., 2020). Their strength lies in their closer comparability to satellite observations and no longer needing certain parameterizations, such as those for deep convection and orographic drag (Satoh et al., 2019). Still, the spatiotemporal spectrum is long. At kilometer-scale grid spacing, GCRMs leave unresolved variability in cloud properties associated with turbulent mixing, surface processes, radiation, and microphysics (Neumann et al., 2019; Richter, 2015).

In moving further down the spatiotemporal spectrum, high-resolution atmospheric simulations such as large-eddy simulations (LES) were developed to address boundary-layer-sized turbulent motions. This is particularly relevant for the STBL, an incredibly turbulent, space-filling structure characterized by fractal-like variability across scales. By resolving the dominant cloud-forming eddies, LES largely account for the vertical transport of heat, moisture, and momentum within the boundary layer, greatly aiding our understanding of boundary-layer dynamics (Deardorff, 1972; Bretherton et al., 1999; Savic-Jovcic and Stevens, 2008; Ackerman et al., 2009; Yamaguchi and Randall, 2012). LES also serve as benchmarks for developing and validating subgrid parameterizations in coarser-resolution models, including schemes for cloud-top entrainment and shallow convection.

Despite these strengths, LES faces limitations. Their high resolution often comes at the expense of domain size, which is typically limited to $\mathcal{O}(10-100\,\mathrm{km})$ (Schlemmer and Hohenegger, 2014; Schalkwijk et al., 2015; Ovchinnikov et al., 2022), with larger domains possible in some cases (Heinze et al., 2017). Even with vertical grid spacings as fine as 5 m, motions below the grid scale remain unresolved and must be parameterized. These limitations in subgrid-scale variability are especially consequential for representing mixing at cloud boundaries. Observational comparisons suggest that LES often introduce numerical dissipation, a bias that leads to overestimated mixing rates and underpredicted cloud liquid water content (Stevens and Bretherton, 1999; Stevens, 2005; Stevens et al., 2005; Cheng et al., 2010; Lozar and Mellado, 2017; Mellado et al., 2018; Hoffmann and Feingold, 2019; Schulz and Mellado, 2019). In practice, LES outputs often need calibration or tuning to match observed cloud properties. Combined with the difficulty of obtaining reliable high-resolution measurements near the sharp cloud-top inversion, this makes it challenging to evaluate how clouds respond to changes in environmental conditions.

Direct numerical simulations (DNS) offer a means to reduce uncertainties of subgrid-scale variability in stratocumulus clouds by explicitly resolving turbulence at meter or sub-meter scales. In contrast to LES, DNS solve the governing equations for mass, momentum, and energy directly, thereby avoiding the parameterization of turbulence altogether. This approach allows for repeated, controlled experiments in which differences in outcomes can be attributed with greater confidence to prescribed environmental conditions rather than to ambiguities in parameter tuning. DNS also help fill gaps where observational data are sparse and assist in the interpretation of in-situ and remote sensing measurements. In the context of sedimentation, LES and coarser-resolution models often suffer from numerical artifacts that generate an upward flux of liquid (Krueger, 1993; Stevens et al., 2000). This upward bias partially opposes the downward motion of falling droplets and weakens the simulated effect of sedimentation on cloud-top entrainment. DNS can reduce this diffusion-related bias.

One of the main constraints of DNS is the limited domain size, a direct consequence of the high computational cost at fine resolutions. Nevertheless, DNS is particularly well-suited for the STBL, as closed-cell stratocumulus clouds are largely homogeneous in the horizontal, with variations occurring primarily in the vertical (Feingold et al., 2010). This allows horizontal averaging to serve as a practical alternative to ensemble averaging. The resulting smooth vertical profiles of mean quantities reveal deterministic properties from chaotic turbulence. Small domain sizes also mean that DNS do not directly interact with global-scale dynamics, instead relying on idealized or simplified boundary conditions to represent the surrounding environment. This approach is justified because small-scale turbulence and boundary-layer processes evolve on much shorter time scales than larger

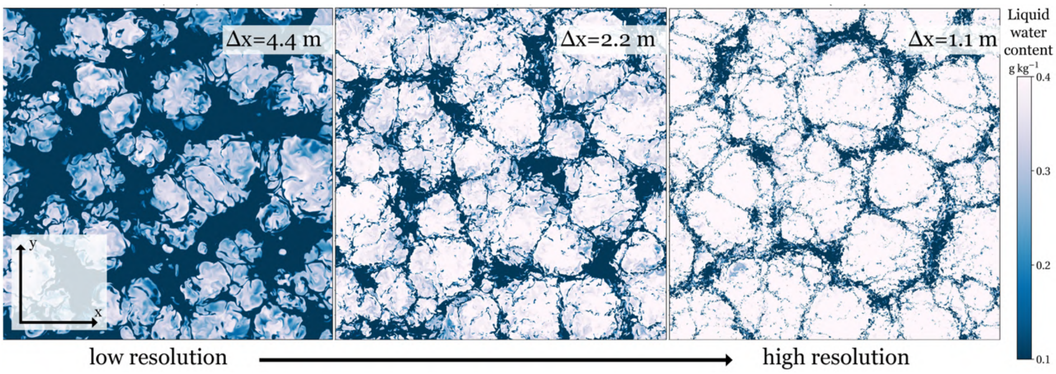

Figure 2.3: Horizontal cross-sections of cloud liquid water for DNS at varying reference Reynolds numbers (left to right: $Re_0 = 2000$, $Re_0 = 5000$, $Re_0 = 12500$) with corresponding grid spacings Δx, illustrating reduced cloud-top mixing as molecular viscosity decreases.

mesoscale motions. For reference, the temporal scales of the STBL are bounded by the average turnover time of the largest eddies, about 20 min (Wyngaard, 2010).

The Reynolds number, $Re = U_0 L_0 / \nu$, is the standard measure of hydrodynamic instability, where L_0 and U_0 are characteristic length and velocity scales, respectively, and μ is the molecular viscosity (Wyngaard, 2010). For subtropical STBL, the Reynolds number typically reaches $\mathcal{O}(10^8)$, which is far above what current computational capabilities permit, where models like DNS are limited to $\mathcal{O}(10^4)$ (LeMone et al., 2019). For this reason, the problem must be scaled down to more feasible Reynolds numbers, which then opens up two equally valid interpretations. One could view the system as a boundary layer with reduced length and velocity scales, similar to a laboratory experiment scaled down to one or two meters, or alternatively as a fluid with increased viscosity, but at the boundary-layer length scales. In this second interpretation, the rate and total amount of dissipation remain unchanged, while the energy cascade dissipates at larger length scales. As a result, the range of length scales in the inertial cascade is shortened while remaining fully resolved. In numerical simulations, this scaling shifts the Kolmogorov length scale from millimeter-scale values characteristic of real stratocumulus clouds to larger, domain-dependent values. In DNS, as the grid spacings are tailored to the newly-scaled Kolmogorov scale, the reduction in the mixing rate between fluid gradients is a physical consequence of reduced diffusion, rather than being due to numerical effects. This distinction helps explain why low-Reynolds-number models often overestimate cloud loss. As illustrated in Figure. 2.3, higher Reynolds numbers and lower molecular viscosities reduce mixing in regions with strong gradients, such as the interface between cloudy and dry air at the cloud top.

Given that the resolution in DNS in this case is still approximately 100 times larger than the actual Kolmogorov scale, it raises concerns about the reliability of DNS results. Fortunately, many key turbulence and statistical properties become independent of Re once it surpasses a critical threshold. When a variable reaches statistical convergence with respect to Re, this is referred to as Reynolds number similarity (Moin and Mahesh, 1998; Monin and Yaglom, 2013; Mellado et al., 2018). Exploiting this self-similarity allows results from currently feasible Reynolds numbers, like meter-scale simulations, to be extrapolated to higher Re, potentially providing a reliable portrayal of atmospheric turbulence. It should be noted that processes below the Kolmogorov scale, including cloud microphysics and radiation, still require parameterization. These are typically represented using bulk or bin schemes, or through clever Lagrangian frameworks such as the probabilistic super-droplet model, which tracks the evolution of representative droplets (Shima et al., 2009) and circumvents numerical diffusion distortions (Yin et al., 2024). In the case of DNS, most of the computational resources are concentrated on reducing uncertainties related to turbulence.

In combination with an efficient microphysics scheme, DNS thus makes a powerful process-resolving tool for investigating the interactions of turbulent motions across small and large scales of the STBL, and serves as the primary modeling approach in this dissertation.

2.4 LOW-CLOUD FEEDBACKS AND CLIMATE IMPLICATIONS

Building on the processes reviewed above, the climate relevance of stratocumulus clouds lies at the confluence of meter-scale turbulence and microphysical processes such as sedimentation. Their interactions with one another regulate cloud-top entrainment, thereby controlling cloud amount and radiative properties. Representing these interactions is particularly pressing for climate modelers, who must rely on high-resolution grids, such as those used in DNS, to represent the multiscale dynamics and sharp capping inversions that define stratocumulus clouds. In addition, while replicating present-day conditions is already demanding enough, predicting and evaluating the behavior of stratocumulus clouds in future warming scenarios inherently adds a degree of difficulty. In particular, indirect aerosol-related feedbacks that involve sedimentation and entrainment can mimic the signatures of an external forcing, producing negative adjustments that blur the distinction between intrinsic cloud dynamics and environmental perturbations. How small-scale processes collectively shape low-cloud feedbacks thus carries major implications for global climate sensitivity.

Enormous efforts have been devoted to quantifying equilibrium climate sensitivity (ECS), defined as the amount of global surface warming necessary to offset the initial radiative imbalance caused by a doubling of atmospheric CO_2 relative to pre-industrial levels. Despite decades of research and new computational technologies—including satellite observations from CERES (2000–present), radar-lidar measurements from CloudSat and CALIPSO (2006–present), and most recently EarthCARE (2024-present) with its Doppler cloud profiling radar—current generation CMIP6 Earth system models have not been able to narrow the ECS range of 1.5–4.5 °C over the last 45 years (Forster et al., 2023). Astonishingly, this range remains close to the first prediction of 4 °C made by Swedish Nobel laureate Svante Arrhenius over a century ago (Arrhenius, 1908). The most recent estimates, drawing heavily on non-model evidence, place ECS in the range of 2.3–4.7 °C (Sherwood et al., 2020; Meehl et al., 2020). Within this persistent uncertainty, evidence strongly suggests that marine stratocumulus clouds remain the leading-order contributor to the spread in climate sensitivity (Bony and Dufresne, 2005; Soden and Held, 2006; Sherwood et al., 2014; Ceppi et al., 2017; Zelinka et al., 2020).

Despite substantial attention devoted to stratocumulus clouds through various lines of evidence (Webb et al., 2006; Nuijens and Siebesma, 2019; Schneider et al., 2019; Sherwood et al., 2020; Christensen et al., 2022), their precise contribution to ECS remains poorly constrained, with simulated estimates often comparable to intramodel variability (Pressel et al., 2017; Myers et al., 2021; Koshiro et al., 2022). Quantification is notoriously difficult, owing not only to computational and observational limitations but also to the many ways in which clouds respond to environmental conditions. In a warming climate, the response of stratocumulus clouds depends on adjustment mechanisms that either amplify (positive feedback) or dampen (negative feedback) the initial radiative imbalance (Siebesma et al., 2020). Three dominant mechanisms have been identified for subtropical marine low clouds (Bretherton et al., 2013; Blossey et al., 2013; Bretherton and Blossey, 2014; Bretherton, 2015; Nuijens and Siebesma, 2019). First, a thermodynamic mechanism, in which elevated sea surface temperatures enhance convective mixing and increase cloud-top entrainment of dry free-tropospheric air, thereby reducing cloud amount. Second, a radiative mechanism, wherein a more emissive free troposphere, due to elevated CO_2 or H_2O concentrations, weakens longwave radiative cooling, reduces turbulence and vertical moisture transport, and thins the clouds. Third, a stability mechanism, in which warming of the free troposphere strengthens the inversion lid, suppressing vertical mixing across the inversion, and promotes thicker clouds.

Although the relative importance of these environmental perturbations under future climate scenarios remains speculative, some responses can be confidently predicted. For example, the Hadley circulation is expected to weaken with climate change, reducing subsidence in the subtropics (Held and Soden, 2006; Vecchi and Soden, 2007; Dussen et al., 2016). With this in mind, a range of studies, including satellite observations and LES, show the robustness of a positive low-cloud feedback when the previously mentioned mechanisms are considered collectively, leading to additional warming of the climate system (Qu et al., 2015; Klein et al., 2018; Schneider et al., 2019; Scott et al., 2020; Sherwood et al., 2020; Myers et al., 2021; Koshiro et al., 2022; Schiro et al., 2022; Forster et al., 2023). What remains uncertain, however, is the extent to which these mechanisms are shaped by microphysical processes such as sedimentation, and how their coupling with meter-scale turbulence affects cloud adjustment. DNS provide a reductionist framework to probe these questions.

3

PAPER I: RESOLVING DROPLET SEDIMENTATION EFFECTS IN STRATOCUMULUS CLOUDS

There is broad consensus on the mechanism of sedimentation on entrainment in stratocumulus clouds, namely, it restricts the amount of liquid water available during entrainment events by moving droplets away from the dry, warm free tropospheric air, thereby decreasing the potential for evaporation at the cloud top. However, the magnitude of this effect remains uncertain. Various LES with bulk and bin-microphysics models, using vertical grid spacings of $5-10$ m, have estimated that sedimentation reduces entrainment rates by $7-15\%$ (Ackerman et al., 2004; Bretherton et al., 2007; Savic-Jovcic and Stevens, 2008; Ackerman et al., 2009; Hill et al., 2009). In contrast, local DNS studies focusing exclusively on the cloud-top region, with much finer grid spacings of 20 cm, reported reductions of up to 40% (Lozar and Mellado, 2017; Schulz and Mellado, 2019). These DNS studies assumed vertically infinite clouds as boundary conditions, which may have masked feedbacks from sedimentation occurring within and below the cloud layer. Only recently have advances in computing power and numerical algorithms made it feasible to simulate the full vertical extent of the STBL at meter-scale resolution. This now provides a means to investigate how microphysical processes such as sedimentation alter the coupling between cloud-top entrainment and boundary-layer turbulence, and, by extension, vertical moisture transport via large-eddy structures throughout the STBL. The motivation for this study, therefore, is to determine whether the sedimentation effects observed in idealized cloud-only DNS also hold when the entire STBL is simulated at high resolution.

The first part of this dissertation summarizes work published in Pistor and Mellado, 2025, which quantifies the effect that droplet sedimentation has on the STBL. Building on previous works of cloud-top entrainment in stratocumulus clouds (Lozar and Mellado, 2015b; Mellado et al., 2018), I use DNS to reduce uncertainties associated with turbulence parameterizations and numerical artifacts related to subgrid-scale diffusion. The analysis simulates the full vertical extent of the STBL, thereby encompassing both ends of the length-scale spectrum relevant for representing turbulence in stratocumulus clouds, from meter-scale motions at the cloud top to large, energy-containing eddies comparable in size to the boundary layer itself.

In particular, this study addresses the following research questions:

1. **What is the magnitude of entrainment reduction by sedimentation in the full STBL?**
2. **How does this mechanism depend on the Reynolds number?**
3. **How does the decrease in mean entrainment velocity link to changes in the turbulence intensity?**

To answer these questions, I conduct sensitivity experiments to assess how variations in sedimentation strength affect the mixing rate between the cloud and environmental air, quantified by the mean entrainment velocity. As a reference case, I use conditions from the first research flight of the DYCOMS-II campaign (Stevens, 2005). To simplify microphysics, I combine DNS with a one-moment bulk microphysics scheme, as done in Lozar and Mellado, 2017; Schulz and Mellado, 2019. This simplification frees up computational resources for a more in-depth study of turbulence processes and allows for direct comparison with earlier studies using the same scheme (Ackerman et al., 2004; Bretherton et al., 2007; Ackerman et al., 2009). Among the several flux terms is the sedimentation flux, which in this bulk scheme appears as the liquid water content multiplied by a single parameter, the bulk sedimentation coefficient c_s, which conveniently then encompasses a spectrum of microphysical parameters, such as the mean droplet size and droplet number density. Since only c_s needs to be modified, it simplifies the setup and reduces the number of simulations. Three sedimentation strengths are examined: none, reference (Sed-Ref), and 2×Sed-Ref. Because results also depend on the Reynolds number, Re, I perform three sensitivity experiments varying Re to evaluate Reynolds number similarity and explore the feasibility of extrapolating conditions from DYCOMS-II to those of the atmosphere. The domain size remains constant across all simulations, while the dynamic viscosity varies by a factor of 2 between the three Reynolds-number cases. For the largest Reynolds number, $Re_0 = 12500$, corresponding to a Kolmogorov scale of $\eta_0 = 0.7$ m, the dynamic viscosity is $\mu_g = 9.27 \times 10^{-2}$ kg m^{-1} s^{-1}. For reference, grid spacings for ascending Reynolds numbers are $\Delta x = 4.4, 2.2, 1.1$ m.

3.1 SEDIMENTATION EFFECTS ACROSS REYNOLDS NUMBERS

The first part of my analysis is to understand how DNS simulations represent the effect of sedimentation. For each combination of sedimentation strength and Reynolds number, DNS solves the full governing equations, resolving the STBL at the respective Kolmogorov scale at all points and times. I calculate the temporal evolution of important bulk properties, such as the vertically integrated liquid water content (LWP), and compare them to available observations and previous LES studies. Consistently, the best agreement with the measurement-based estimate of 60 g m^{-2} is found for the highest Reynolds number case, $\eta_0 = 0.7$ m. Increasing the Reynolds number leads to higher LWP due to reduced mixing in the cloud-top region, which then enhances longwave radiative cooling, strengthens turbulence, and increases moisture transport. The agreement with measurements also holds true for mean profiles, notably, DNS comes closest to matching the observed region of negative skewness in the upper boundary layer, a signature of downdrafts. The DNS estimates of the mean entrainment velocity, w_e, lean toward the upper bound of the observational range, $3.9 - 4.7$ mm s^{-1} (Faloona et al., 2005; Stevens et al., 2003). These results give confidence that the DNS simulations can represent the effect of sedimentation. Even at the intermediate Reynolds number ($\eta_0 = 1.4$ m), DNS results fall within the spread of previous LES studies.

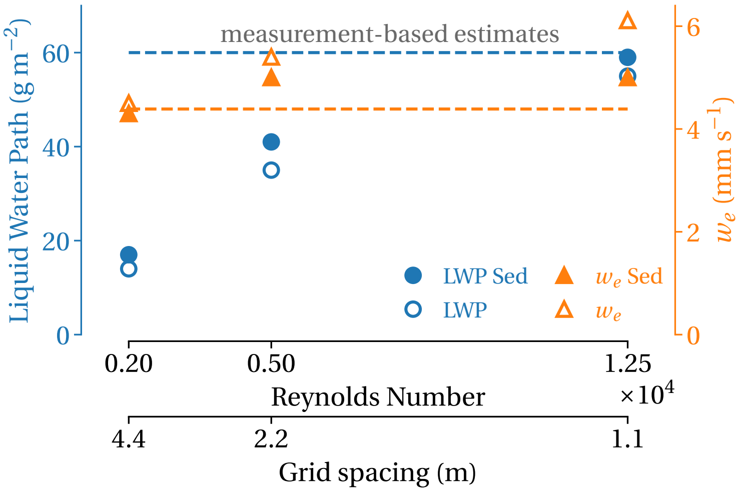

Figure 3.1: Dependence of LWP and mean entrainment velocity on sedimentation strength and Reynolds number. Filled shapes: reference sedimentation strength from DYCOMS-II; hollow shapes indicate no sedimentation. Dotted lines show measurement-based estimates of LWP (blue) and w_e (orange), with w_e as the mean of the estimated range $3.9 - 4.8$ mm s^{-1}.

To quantify the magnitude of entrainment reduction by sedimentation, the time series of LWP and w_e are temporally averaged to yield a single value per simulation, shown in Figure 3.1. For each Reynolds number, the sedimentation effect is indicated as the difference between the no-sedimentation and reference cases, indicated by hollow and filled shapes, respectively. At meter-scale resolution ($\eta_0 = 0.7$ m), sedimentation causes at least a 20% decrease in mean entrainment velocity. This estimate lies between the $7 - 15$% range reported by LES studies and the 40% found in the local-cloud DNS studies. It should be noted that the 40% reduction reported in Schulz and Mellado, 2019 corresponds to a strong sedimentation case; our 20% estimate, which is based using the reference case, is consistent with this trend and accounts for the lower magnitude.

While Reynolds number sensitivity is evident in bulk properties, convergence begins to emerge at $Re_0 = 12500$ ($\eta_0 = 0.7$ m). The relative differences in LWP and w_e between $\eta_0 = 2.8$ m and $\eta_0 = 1.4$ m are larger than those between $\eta_0 = 1.4$ m and $\eta_0 = 0.7$ m. This convergence of LWP and w_e toward their respective measurement-based estimates as Re_0 increases suggests Reynolds number similarity. However, the sensitivity to Reynolds number differs between these two quantities. While the effect of sedimentation on LWP remains relatively constant, its effect on w_e grows with increasing Re. This is why the phrasing *at least* is used in the previous paragraph. At higher Re, the sedimentation-induced reduction in w_e becomes comparable to, or even exceeds, changes caused by Reynolds number effects alone. Notably, at $\eta_0 = 0.7$ m, sedimentation effects outweigh Reynolds number effects on the mean entrainment velocity. This lends confidence that DNS at this scale can begin to disentangle the interactions between sedimentation and turbulence.

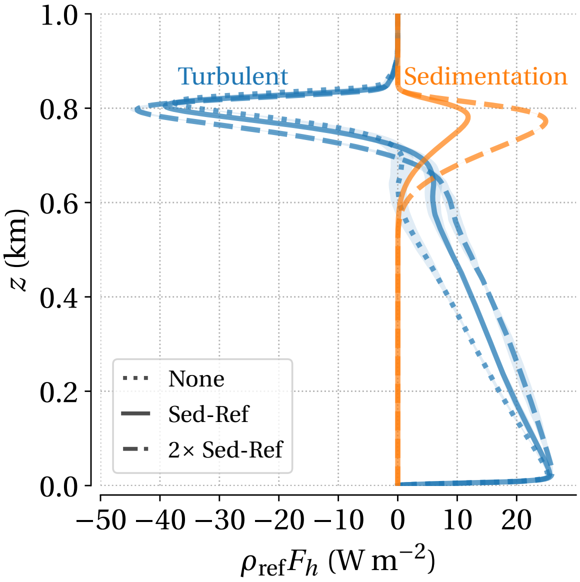

Figure 3.2: Vertical profiles of the turbulent and sedimentation fluxes for the liquid water static energy. The Kolmogorov scale is fixed at $\eta_0 = 1.4$ m, and all profiles are averaged both horizontally and temporally, with the standard deviation indicated by shaded regions. The radiative and molecular fluxes are omitted for presentation purposes.

3.2 TURBULENCE AND MOISTURE ORGANIZATION

Turbulence intensity, measured by the variance of vertical velocity, increases with sedimentation strength throughout the entire STBL. Counterintuitively, this occurs alongside a reduction in the mean entrainment velocity, prompting the question: how does turbulence intensity increase while the mean entrainment velocity simultaneously decreases?

To answer this, I decompose the mean entrainment velocity into its various flux constituents. In DNS, w_e can be estimated by tracking a reference inversion height, z_i, such as the minimum turbulent flux of liquid-water static energy, h, relative to large-scale subsidence. But, because computing the derivative of $z_i(t)$ introduces unwanted noise, I use the analytically derived mean entrainment-rate equation (Mellado, 2017; Mellado et al., 2018), which, to a good approximation, can be simplified to:

$$w_e\left(\langle \phi \rangle_{z_i} - \phi_{\mathrm{bg},z_i}\right) \approx F_{\phi,z_i} \,. \tag{1}$$

Here, ϕ is a fluid property per unit volume, typically representing energy or moisture. F_ϕ is the average flux of ϕ and $\langle \phi \rangle_{z_i} - \phi_{\mathrm{bg},z_i}$ is the jump in ϕ across the inversion as it ascends. It is also known as the flux-jump relation. The equation is exact, as it is derived from integral analysis; the challenge lies in accurately measuring the individual terms. As w_e is the most difficult term to measure, focusing on the jump and fluxes allow one to infer w_e (Nicholls and Turton, 1986). For this study, the entrainment rate equation is used to decompose w_e into contributions from the various flux components: turbulent, molecular, radiative, and sedimentation.

The decomposition of h fluxes in Figure 3.2 shows that both turbulent and sedimentation fluxes increase with sedimentation strength. As the droplet size distribution shifts towards larger, heavier droplets (Grabowski and Abade, 2017), these droplets sediment farther from the cloud top and are less effectively transported upward by turbulent motions. This reduces liquid water near the cloud top and removes $\langle h \rangle$ from the STBL, since water vapor contains more energy than liquid water. Crucially, the turbulent and sedimentation contributions to the static energy flux are similar in magnitude but opposite in sign. Because they can offset each other, both are energetically significant. While the turbulent flux of h tends to smooth the mean gradient, the sedimentation flux reinforces it. This suggests that the two fluxes scale differently with increasing sedimentation strength. What matters is not their absolute values, but their incremental change. We now understand that the mean entrainment velocity decreases because the sedimentation flux compensates for the turbulent flux of h, with the former increasing more rapidly as sedimentation strengthens.

As evaporative cooling at the cloud top weakens with sedimentation, the increase in turbulence intensity calls for a deeper look into the underlying mechanisms. The first clue appears in the vertical velocity skewness profile (see Appendix A), which points to the organization of moisture between rising and sinking motions (Tillman, 1972; Moeng and Rotunno, 1990). Positive skewness indicates strong, narrow updrafts surrounded by weak and broad downdrafts, and vice versa for negative skewness. As sedimentation increases, positive skewness in the lower STBL decreases, suggesting that downdrafts are intensifying. To explore this further, I examine how liquid water and water vapor are vertically redistributed with sedimentation. The idea is that, while total water content remains fixed, since surface fluxes are prescribed, sedimentation alters the partitioning between liquid and vapor phases, which reshapes the organization of turbulence.

We begin the analysis at the cloud top, where entrainment brings warm, dry air from the free troposphere down into the boundary layer; a process visible in the temperature cross-sections (top row of Figure 3.3). Sedimentation weakens this entrainment by pulling the cloud downwards, which reduces the evaporation rate of water droplets near the inversion. As a result, cloud liquid water increases with sedimentation (second row). Conditioning the vertical velocity into downdrafts and updrafts reveals that, as sedimentation strength increases, the dry downdrafts become even drier due to less evaporation at cloud top, while the cloud cores become denser with liquid water (Figure A.8). This growing contrast between moist cloud cores and dry downdrafts fuels evaporative cooling at the cloud edges, accelerating the downdrafts and acting as a source of turbulence. At the same time, reduced entrainment of warm, dry air results in more water vapor accumulating in the subcloud layer (third row). These moisture-rich regions coincide with the updrafts (bottom row). As turbulence intensifies, the downdrafts more forcefully displace the warm, near-surface air, driving convective updrafts via the pressure gradient force (Bretherton et al., 2007; Ackerman et al., 2009; Lozar and Mellado, 2017).

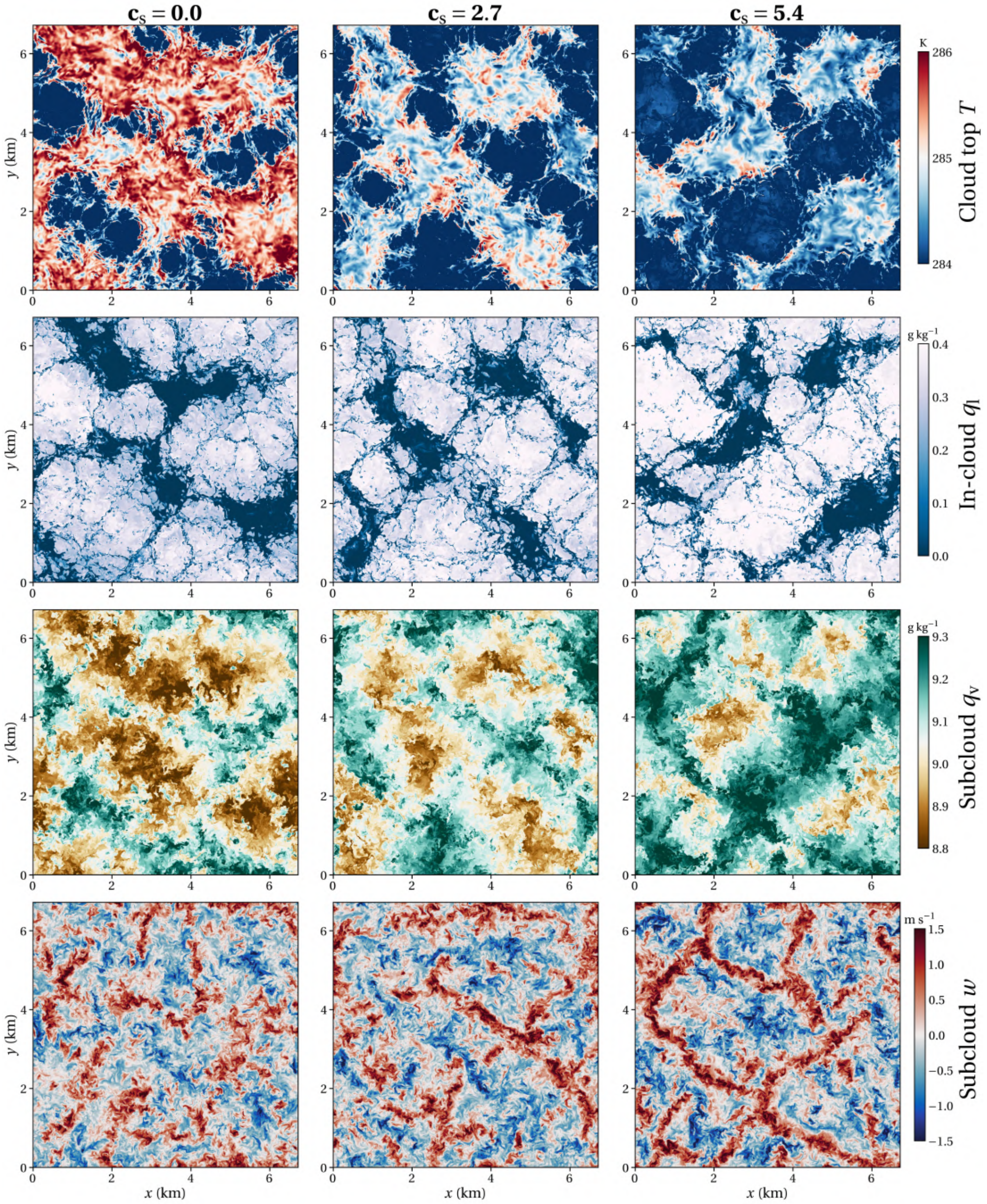

Figure 3.3: Horizontal cross-sections of the temperature, liquid water and water vapor specific humidity, and vertical velocity are shown from top to bottom, respectively. Columns correspond to increasing sedimentation strengths: $c_s = 0.0$, $c_s = 2.7$, and $c_s = 5.4$ mm $s^{-1}/(kg\ m^{-3})^{2/3}$. All cross-sections are obtained for $Re_0 = 5000$ at $t = 4$ h. Specific heights at which each variable is evaluated, listed from left to right: temperature at the cloud top at 847 m, 829 m, and 809 m; liquid water in the cloud layer at 793 m, 780 m, and 760 m; water vapor and vertical velocity in the subcloud layer at 363 m, 386 m, and 365 m.

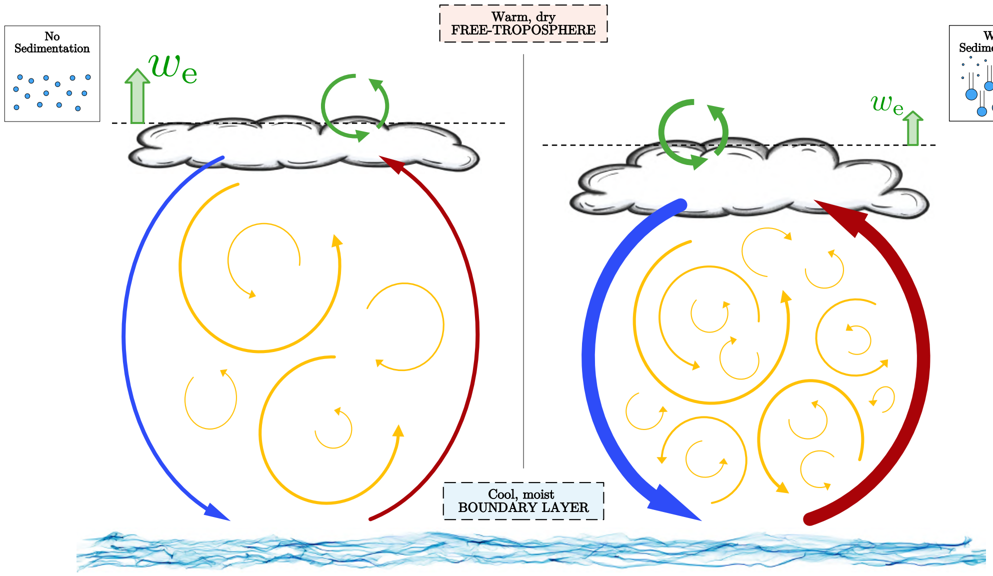

Figure 3.4: Schematic showing how droplet sedimentation affects cloud amount (cloud size), cloud-top height (dashed line), turbulence (yellow arrows), the mean entrainment velocity, w_e (size of the straight arrow connected to the cloud-top height line), and vertical motions (blue/red arrows for downdrafts/updrafts). Line thickness indicates intensity; green circular arrows indicate the entrainment turbulent flux of $\langle h \rangle$.

Sedimentation therefore plays a key role in reshaping the vertical distribution of moisture and the organization of turbulence into more coherent large-scale structures within the full STBL, influencing both cloud and subcloud dynamics. These findings are summarized in Figure 3.4.

In summary, the first study yields the following key findings:

1. Sedimentation reduces the mean entrainment velocity by at least 20%, with the magnitude growing with increasing Reynolds numbers.

2. A vertical resolution of 2 m is needed to capture this reduction and prevent the overestimation common in LES studies.

3. Increasing sedimentation strength increases the sedimentation flux more rapidly than the turbulent flux of $\langle h \rangle$, compensating the turbulent flux and thereby reducing the mean entrainment velocity.

4. Sedimentation intensifies turbulence by increasing moist-dry contrasts, promoting moisture redistribution; capturing these dynamics and their organization requires meter-scale resolution.

4

PAPER II: LINKING DROPLET SEDIMENTATION TO STRATOCUMULUS ADJUSTMENT MECHANISMS: A FINER LOOK

The previous chapter showed that sedimentation effects on cloud-top entrainment and turbulence are sensitive to the effective Reynolds number. By simulating the full vertical extent of the STBL using DNS, I found that localized evaporative cooling events in the cloud layer can accelerate large-scale downdrafts, which in turn intensify turbulence throughout the STBL. Notably, at vertical grid spacings near 1 m, the impact of sedimentation on cloud-top entrainment exceeded that of further increases in the Reynolds number. These findings suggest that subgrid-scale variability—often relegated to parameterization in coarse LES models—is dynamically important and should not be overlooked in boundary layer studies.

While the previous chapter focused on viscosity-tied changes associated with the Reynolds number, the environmental background conditions were held constant. This raises a broader question: within the same DNS modeling framework, to what extent do microphysical processes like sedimentation contribute to large-scale stratocumulus adjustments triggered by environmental forcing? A natural next step is to explore how sedimentation interacts with variations in environmental conditions, particularly those anticipated under climate change. Known as low-cloud adjustment mechanisms, these responses include: (i) thermodynamic warming, (ii) reduced downwelling longwave radiation, and (iii) increased inversion strength (Bretherton, 2015). While a myriad of studies has examined sedimentation effects and low-cloud adjustment mechanisms separately, their interplay remains largely unexplored.

This study is framed around the following research questions:

1. **How does the magnitude of sedimentation effects compare to that of low-cloud adjustment mechanisms?**
2. **What is the sensitivity of low-cloud adjustments to sedimentation?**

As in the first study, I use DNS to simulate the full vertical structure of the STBL. This time, I investigate how droplet sedimentation affects various adjustment mechanisms of stratocumulus clouds. The reference control case (CTL) again follows the environmental conditions from the first research flight of the DYCOMS-II observational campaign (Stevens, 2005), representing a non-precipitating, nocturnal marine stratocumulus layer over a warm subtropical ocean. Sedimentation is modeled using the same one-moment bulk microphysics scheme. I test three sedimentation strengths: none, reference (Sed-Ref), and 2×Sed-Ref, quantified by the bulk sedimentation coefficient, c_s (units: m $s^{-1}/(kg\ m^{-3})^{2/3}$). All simulations use a DYCOMS-II-based reference Kolmogorov scale of $\eta_0 = 1.4$ m, corresponding to a Reynolds number of $Re_0 = 5000$ and an isotropic grid spacing of 2.2 m.

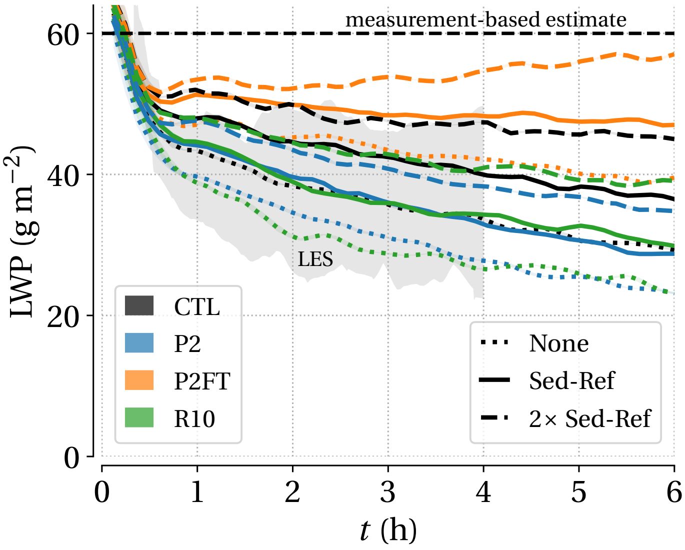

Figure 4.1: Temporal evolution of vertically integrated liquid water content (LWP) for CTL, P2, P2FT and R10 cases under three sedimentation strengths. The gray shading indicates the LES ensemble range from Stevens, 2005, and the dashed black line indicates measurement-based estimates.

To test low-cloud adjustment mechanisms, I compare the CTL case to a set of perturbed simulations designed to represent idealized climate change scenarios, following Blossey et al., 2013; Bretherton et al., 2013; Bretherton, 2015; Nuijens and Siebesma, 2019. These include: (i) P2, a uniform 2 K increase in SST with moist-adiabatic warming throughout the air column; (ii) P2FT, the same warming applied only to the free-troposphere; and (iii) R10, a 10% reduction in the radiative flux profile above the cloud layer, mimicking increased concentrations of H_2O or CO_2. Altogether, 9 sensitivity experiments are run to span combinations of sedimentation strength and environmental perturbations.

4.1 VALIDATION AND SENSITIVITY TO ENVIRONMENTAL FORCING

To answer my research questions, my first step is to assess how well the CTL simulation compares with previous LES-based modeling efforts. Fortunately, this comparison has been made in the first study, as the same moderate-Reynolds-number configuration is used here, with identical initial conditions, boundary conditions, and domain configuration. Figure 4.1 shows the temporal evolution of LWP for the CTL case across all three sedimentation strengths, along with the perturbed simulations (P2, P2FT, R10). All simulations begin with a fully saturated cloud deck and a measurement-based LWP of 60 g m^{-2}. Compared to the LES ensemble reported by Stevens, 2005 (gray region), the CTL simulations sit closer to measurement-based estimates. This agreement lends confidence that the moderate-Reynolds-number DNS captures the cloud evolution realistically, providing a trustworthy, parameterization-free baseline for further analysis.

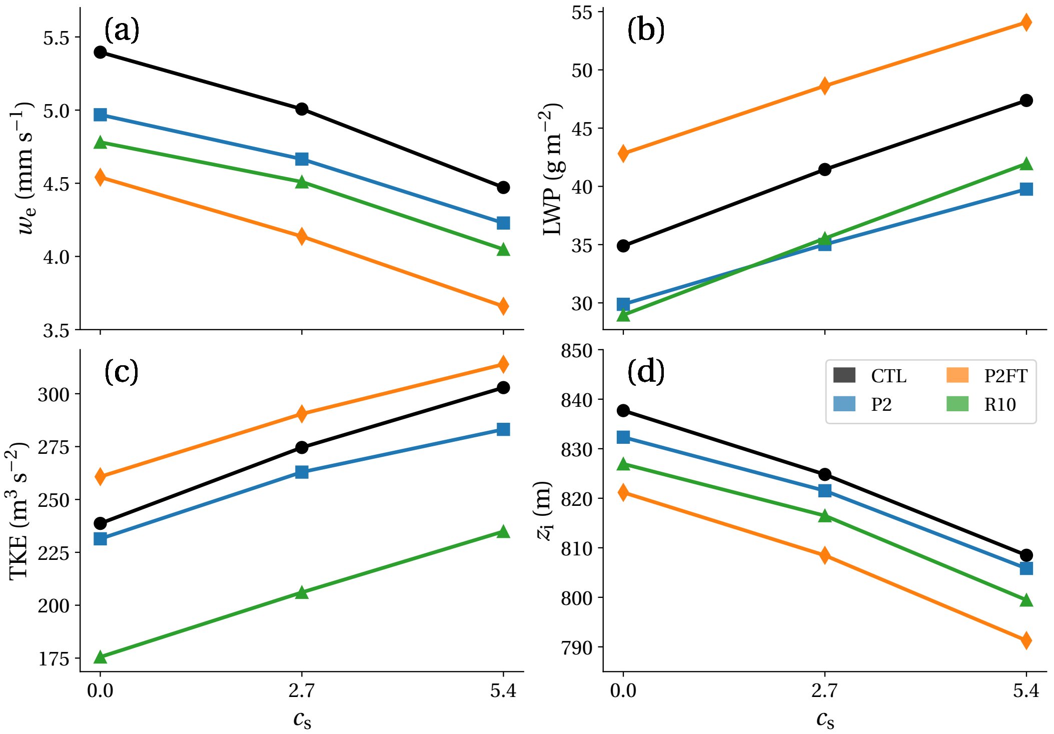

Figure 4.2: Time-averaged values (from the first hour onward) of: (a) mean entrainment velocity w_e, (b) liquid water path (LWP) (c) vertically integrated turbulence kinetic energy (TKE) and (d) inversion height z_i, for the CTL, P2, P2FT and R10 cases under three sedimentation strengths: $c_s = 0.0$, $c_s = 2.7$, and $c_s = 5.4$ mm s^{-1}/(kg m^{-3})$^{2/3}$.

In addition to LWP, the temporal evolution of TKE, mean entrainment velocity (w_e), and inversion height (z_i) is computed for all simulations. However, the time series alone makes it difficult to identify clear patterns across cases. To facilitate comparison, I time-average each variable from the first hour onward, giving a single value per simulation (see Figure 4.2). Consistent with findings from the first study, increasing sedimentation strength, regardless of environmental conditions (CTL, P2, P2FT, R10), leads to a reduction in w_e, an increase in both LWP and TKE, and a lowering of z_i. The largest responses are seen in w_e, LWP, and TKE, while those in z_i are comparatively smaller.

To analyze the sensitivity of adjustment mechanisms to sedimentation, I adopt a relative change perspective. Figure 4.3 shows the percentage changes resulting from sedimentation and environmental perturbations. The effects of environmental changes alone were computed as the difference between each perturbed case (P2, P2FT, R10) and the CTL. These are shown by bar plots with different line styles (dotted, solid, and dashed) representing increasing sedimentation strength. Sedimentation effects alone are shown as symbols, calculated as the difference between no-sedimentation ($c_s = 0.0$) and Sed-Ref ($c_s = 2.7$) for each environment (CTL, P2, P2FT, R10).

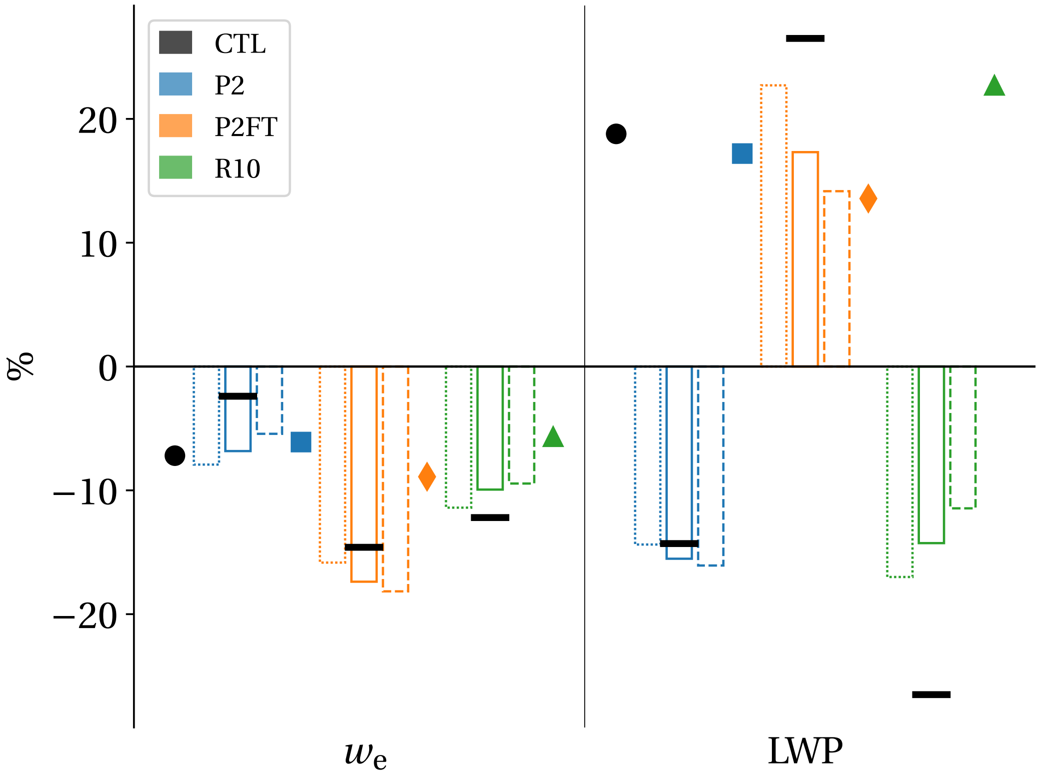

Figure 4.3: Relative changes in time-averaged values of (a) mean entrainment velocity (w_e), (b) liquid water path (LWP) (c) vertically integrated turbulence kinetic energy (TKE), and (d) inversion height (z_i) for CTL, P2, P2FT and R10 cases under varying sedimentation strengths, c_s (units: m $s^{-1}/(\text{kg m}^{-3})^{2/3}$). Symbols show percentage changes from the no-sedimentation case to the Sed-Ref case within each environment (color-coded). Bar plots show changes in the perturbed environments relative to CTL. Black lines show results from LES simulations in Bretherton et al., 2013.

What becomes discernible is that sedimentation effects (symbols) are of similar magnitude to the low-cloud adjustment mechanisms (bar plots). Because the signs of these responses sometimes differ, this similarity in magnitude suggests the potential for compensatory interactions between them. It follows that sedimentation should be accounted for when evaluating the sign and magnitude of low-cloud feedbacks. To put this in perspective, consider the relative changes in LWP for the three environmental perturbations. For all sedimentation strengths, the sum of the LWP responses yield a net cloud thinning response, consistent with a positive low-cloud feedback.

Figure 4.3 includes LES results from Bretherton et al., 2013 (described in further detail in Bretherton et al., 2013; Ackerman et al., 2009), shown as black horizontal lines superimposed on the bar plots. This study represents droplet sedimentation using a bulk log-normal droplet size distribution, as it is done in my study. For w_e, DNS and LES agree in the sign of relative changes, while in most cases, the magnitudes are approximately consistent. This suggests DNS as a more reliable modeling tool, especially now as moderate Reynolds number simulations become computationally feasible and reduce the need for tuned turbulence parametrizations. My study can therefore be regarded as a feasibility assessment of using DNS to address this question, with the results serving as a proof of concept for DNS. The implications suggest that investing additional resources to reach higher Reynolds numbers would be worthwhile, in order to better constrain and refine the conclusions. Still, notable differences between DNS and LES remain: in the P2 case, DNS shows a reduction in w_e more than twice that reported in LES; similarly, LES tends to overestimate the relative changes in LWP for P2FT and R10.

These discrepancies in magnitude point toward an underlying sensitivity of low-cloud adjustment mechanisms to unresolved Reynolds number effects. This sensitivity is shown in Figure 4.3 as differences between the bar plots within each perturbation case. For both w_e and LWP, the approximate magnitude and sign of the relative response across all three perturbed cases (P2, P2FT, R10) remain largely insensitive to sedimentation strength (i.e., small differences). Thus, regardless of the environmental perturbation, the relative adjustments of w_e and LWP are preserved. The positive low-cloud feedback is therefore robust in relative terms with respect to sedimentation strength, while the absolute magnitude of the response scales systematically with sedimentation strength (and, equivalently, aerosol concentration).

As demonstrated in the first study, w_e is sensitive to the Reynolds number. At grid spacings near 1 m, the sedimentation-induced reductions in w_e can reach up to at least 20%, and more importantly, this reduction becomes increasingly pronounced at higher Reynolds numbers. DNS, by resolving finer spatial structures, offers better mechanistic insight, such as accurately representing localized evaporative cooling events that LES might smooth out. Given both the sensitivity of adjustment mechanisms to sedimentation, and the Reynolds number dependence of sedimentation effects, it is reasonable to expect the responses shown in this study will increase at higher Reynolds numbers. In turn, this suggests that under more realistic turbulent conditions, the interplay between sedimentation and low-cloud adjustment mechanisms may play a more significant role in shaping STBL dynamics.

To summarize, the second study has the following key findings:

1. Stronger sedimentation consistently increases LWP and reduces mean entrainment velocity across all environmental perturbations.
2. Sedimentation effects are comparable in magnitude to environmental adjustments and can produce compensatory interactions that alter cloud response.
3. Positive low-cloud feedback remains robust in its relative response; the absolute response, however, depends on sedimentation strength.

5

SUMMARY, CONCLUSIONS, AND OUTLOOK

The overarching goal of this dissertation was to quantify how droplet sedimentation influences turbulence and entrainment in the STBL, and how these interactions shape cloud adjustments under climate warming conditions. The sensitivity of cloud properties—including boundary-layer height, cloudiness, and turbulence intensity—to sedimentation strength was examined across a range of Reynolds numbers (up to $\mathrm{Re}_0 = 12500$) and controlled environmental setups. DNS were used to resolve the full vertical extent of the STBL, capturing meter-scale turbulence, the thin inversion layer at the cloud top, and the larger eddies that reallocate moisture between updrafts and downdrafts. Unlike traditional LES, this DNS-based approach largely circumvents the ambiguity introduced by turbulence parameterizations and unphysical moisture diffusion, allowing for clearer isolation of sedimentation and turbulent effects.

Based on the first study, I found that increased sedimentation strength reduces the mean entrainment velocity by at least 20%. This estimate comes from the highest Reynolds number tested (Kolmogorov scale: 0.7 m), and the phrasing *at least* refers to the fact that this reduction increases with increasing Reynolds number. At moderate Reynolds numbers (grid spacing: 2 m), the DNS results reproduce LES-reported values of cloud liquid water, which is promising given that the DNS simulations do not rely on any tuning of turbulence parameterizations. At resolutions near 1 m, sedimentation effects on the mean entrainment velocity become comparable in magnitude to those of varying the Reynolds number, suggesting that sedimentation effects can be separated from purely turbulent ones. Moreover, the results converge towards measurement-based estimates, suggesting that turbulence is sufficiently resolved at the relevant Reynolds numbers, such that viscous forces do not overshadow the dynamics (Reynolds number similarity), thereby supporting the extrapolation of sedimentation-turbulence interactions to atmospheric conditions.

The apparent conundrum of increasing turbulence intensity as mean entrainment velocity decreases is resolved through the entrainment-rate equation. This framework allows me to decompose the mean entrainment velocity into its constituent fluxes. Analysis of the vertical mean fluxes of liquid water static energy at the cloud top shows that the sedimentation flux becomes similar in magnitude to the turbulent entrainment flux, as it increases more rapidly with sedimentation strength. Consequently, the change in sedimentation flux offsets the change in turbulent flux, reducing the mean entrainment velocity despite the intensification of turbulence. Importantly, this compensating effect is underestimated at coarser resolutions.

In taking a closer look at the vertical distribution of moisture, I revealed the connection between cloud-top entrainment and turbulence generation. This link becomes apparent only when simulating the full depth of the STBL and resolving entrainment events at fine scales. In brief, sedimentation reduces cloud-top evaporation, allowing cloudy regions to retain more liquid water, while concurrently promoting increased evaporation along the sides of downdrafts as air is drawn through cloud holes. This process accelerates the downdrafts, which in turn further drives additional turbulence. These findings demonstrate that resolving both the cloud and subcloud layers at meter-scale resolution is necessary to fully understand moisture redistribution and the organization of turbulence. It is not only the inversion-layer mixing that matters, but also the interactions occurring at cloud boundaries and below.

In the second study, I set out to examine the interplay between sedimentation and low-cloud adjustment mechanisms. For the first time, sedimentation and climate-relevant environmental perturbations are combined using DNS at a moderate Reynolds number ($Re_0 = 5000$, corresponding to a Kolmogorov scale of $\eta_0 = 1.4$ m). These perturbations represent variations in column temperature, inversion strength, and incoming longwave radiation. I found that, within each environmental setup, increasing sedimentation strength consistently reduces the mean entrainment velocity, while increasing cloud liquid water. When the sedimentation strength is fixed and only environmental perturbations are applied relative to the DYCOMS-II-based reference case, the DNS results reproduce both the sign and approximate magnitude of the changes reported in previous LES studies (Bretherton et al., 2013). This agreement motivates broader use of DNS, as moderate Reynolds number simulations are now more computationally feasible ($\approx$5,600 node-hours per simulated hour) and allow ad-hoc turbulence parameterizations to be gradually phased out.

When considered together, the effects of sedimentation and low-cloud adjustment mechanisms are comparable in magnitude, suggesting the potential for compensating or amplifying interactions. Because sedimentation acts as a proxy for aerosol concentration, omitting such microphysical processes risks mischaracterizing cloud responses to climate warming. I showed that the positive low-cloud feedback is robust to changes in sedimentation strength in relative terms, but not in absolute magnitude. Current global observations show that anthropogenic aerosol emissions have declined in many regions, with clear trends evident in satellite records since 2000, while natural aerosol emissions, such as from volcanic activity, biomass burning, dust, and sea salt, remain highly variable and sensitive to temperature and wind (Quaas et al., 2022). In addition, because sedimentation-induced changes strengthen with the Reynolds number, the agreement between DNS and LES at moderate Reynolds numbers may not hold at higher Reynolds numbers. Overall, the sensitivity of stratocumulus clouds to climate-relevant perturbations and sedimentation materializes through complex interactions among turbulence, entrainment, and moisture transport.

This dissertation demonstrates that sedimentation effects are as important as turbulence- and environment-driven adjustments in shaping stratocumulus dynamics, and that meter-scale resolution is needed to resolve their combined influence. Extrapolating these findings to atmospheric conditions looks favorable, given the convergence of multiple variables, such as cloud liquid water and mean entrainment velocity, toward measurement-based estimates, suggesting Reynolds number similarity. Given that marine stratocumulus clouds remain one of the leading sources of uncertainty in the spread of climate sensitivity estimates, achieving more reliable predictions will require sustained advances in modeling techniques, computational power, and observational efforts, along with improvements in the physical realism of microphysical parameterizations, particularly the accurate representation of droplet size distributions. Altogether, while this DNS approach has limitations—such as the use of a one-moment bulk microphysics scheme for sedimentation, simplified saturation-adjustment microphysics, and a one-dimensional radiative transfer model—it nonetheless provides a clear pathway toward resolving uncertainties in stratocumulus dynamics and improving our ability to predict cloud responses to ongoing climate change.

Part II

APPENDIX

A

RESOLVING DROPLET SEDIMENTATION EFFECTS IN STRATOCUMULUS CLOUDS

The work in this appendix has been published as:

Pistor, R. & Mellado, J. P. (2025). Resolving droplet sedimentation effects in stratocumulus clouds. Journal of Advances in Modeling Earth Systems, 17(8), e2025MS004966.

Resolving Droplet Sedimentation Effects in Stratocumulus Clouds

Raphael Pistor[1] and Juan Pedro Mellado [2]

[1]International Max Planck Research School on Earth System Modelling, Max Planck Institute for Meteorology, Hamburg, Germany
[2]Meteorological Institute, University of Hamburg, Hamburg, Germany

ABSTRACT

We use direct numerical simulations to quantify the effects that droplet sedimentation has on the stratocumulus-topped boundary layer. Our analysis includes both ends of the length-scale spectrum that are deemed important for representing turbulence in stratocumulus clouds, spanning from meter scales at the cloud top to large energy-containing eddies the size of the boundary layer. We conduct sensitivity experiments that involve varying the droplet sedimentation strength and the Reynolds number. Consistent with previous studies, we find that increasing sedimentation causes a decrease in mean entrainment velocity, with an observed effect of at least 20%. Interestingly, the turbulence kinetic energy and the turbulent entrainment flux are enhanced by sedimentation. To reconcile the apparent contradiction of turbulent flux increasing and mean entrainment velocity decreasing, we quantify the various mean fluxes of the liquid water static energy in the cloud-top region, as needed for the evaluation of the entrainment-rate equation. As sedimentation strength intensifies, the magnitude of the sedimentation flux undergoes a more rapid increase than the turbulent flux, effectively compensating for the increase in turbulent flux. To explain the increase in turbulence intensity, we show that sedimentation increases the contrast between descending dry, warm air in cloud holes and the moist, cold air within cloudy puffs. This increased contrast intensifies evaporative cooling near the cloud hole edges, which accelerates the downdrafts, drives turbulence, and distributes moisture more evenly between the cloud and subcloud layers. Overall, we show that microphysical effects are as important as turbulent effects at meter-scale resolution.

A.1 INTRODUCTION

Stratocumulus clouds extend over vast areas of the subtropical ocean, inducing a negative radiative forcing by reflecting incoming solar radiation and effectively influencing the Earth's radiation balance (Klein and Hartmann, 1993; Wood, 2012; Schween et al., 2022). Even small variations in low cloud cover can offset the warming effect of a doubling in atmospheric carbon dioxide (Randall et al., 1984), therefore considerable efforts have been devoted to better quantify climate feedbacks associated with stratocumulus clouds (Nuijens and Siebesma, 2019; Schneider et al., 2019; Sherwood et al., 2020; Christensen et al., 2022). In addition to their climatic importance, there are strong interests in further understanding the potential of aerosol perturbations, specifically marine cloud brightening, as a climate mitigation measure (Latham, 1990; Glassmeier et al., 2021; Feingold et al., 2024; Hoffmann et al., 2024). However, the complex, multiscale interactions that govern the response of stratocumulus clouds to changes in environmental conditions remain inadequately understood, leaving the fate of these clouds in a warmer climate uncertain. This uncertainty is further underscored by observationally constrained estimates of low-cloud radiative feedback, which are three times larger than model estimates (Myers et al., 2021), and inter-model variability is as large as the mean (Pressel et al., 2017; Sherwood et al., 2020; Koshiro et al., 2022). Quantifying the dynamics and interactions of small-scale phenomena within a stratocumulus-topped boundary layer (STBL) is important for assessing the macroscopic properties of these clouds. In this study, we focus on one specific microphysical process that affects cloud lifetime—droplet sedimentation—and its impact on entrainment and turbulence in stratocumulus clouds.

Ackerman et al., 2004 showed that enhanced sedimentation rates reduce the mean entrainment velocity and, under dry inversions, increase the liquid water path (LWP). Bretherton et al., 2007 extended this finding by stating that sedimentation restricts the amount of liquid water available during entrainment events by moving droplets away from the dry and warm free tropospheric air, thereby lowering the potential for evaporation at the cloud top. As reported by Lozar and Mellado, 2017, a second effect involves the generation of a positive buoyancy flux induced by the descent of the droplets. Sedimentation also reduces the maximum radiative cooling rate at the cloud top due to the formation of larger, less numerous droplets, thereby decreasing entrainment (Williams and Igel, 2021). Diminished entrainment warming subsequently fosters a cooler, moister, and more coupled STBL, enhancing the preservation of cloud water (Hoffmann et al., 2020). Various large-eddy simulation (LES) with bulk and bin-microphysics models showed the magnitude of mean entrainment velocity reduction by sedimentation to be between $7-15\%$ (Ackerman et al., 2004; Bretherton et al., 2007; Savic-Jovcic and Stevens, 2008; Ackerman et al., 2009; Hill et al., 2009).

One question that remains open is the extent to which insufficient numerical resolution might affect these estimates of entrainment reduction by sedimentation. LES models typically use vertical grid spacings of $5-10$ m; however, higher vertical resolution is needed to properly resolve the range of spatial scales related to entrainment. This need arises because the environmental conditions of subtropical highs prompt a very thin capping inversion of temperature, humidity, and density at the cloud-top interface, which can be as thin as a few tens of meters (Wood, 2012; Mellado, 2017). More specifically, the Ozmidov scale in the cloud-top region is of the order of $0.5-1$ m (Mellado et al., 2018). The Ozmidov scale separates the smaller turbulence-dominated scales from the larger gravity-wave-dominated ones, with the latter being inefficient at mixing. Consequently, insufficient vertical resolution typically results in a spurious upward flux that directly opposes the downward motion of descending droplets. Because of this non-physical upward transport of liquid water, the influence of sedimentation on entrainment strength is weakened. Indeed, local direct numerical simulations (DNS) studies focusing exclusively on the cloud-top region, with grid spacings of 20 cm, observed a 40% reduction of the mean entrainment velocity due to droplet sedimentation, instead of $7 - 15\%$ (Lozar and Mellado, 2017; Schulz and Mellado, 2019). However, these local studies assumed infinite clouds as boundary conditions, thereby potentially masking feedbacks to changes in sedimentation within and below the cloud layer. The motivation for this work is to determine whether those results also hold when considering the entire vertical domain of the STBL, spanning from the surface level to the free troposphere.

While there is consensus on the mechanism of sedimentation reducing cloud-top evaporation (Ackerman et al., 2004; Bretherton et al., 2007; Wood, 2012; Ackerman et al., 2009; Lozar and Mellado, 2017; Schulz and Mellado, 2019), the impact on turbulence inside the cloud and the boundary layer, and thereby indirectly on the mean entrainment velocity, remains less clear. While turbulence is primarily generated at the cloud top, reduced evaporative cooling in that region due to sedimentation may not necessarily lead to decreased turbulence. For instance, more available liquid water due to reduced cloud-top evaporation can alter the distribution of moisture within downdrafts and updrafts. It has been suggested that sedimentation redirects droplet evaporation into the downdrafts, resulting in turbulence generation there (Stevens et al., 1998; Bretherton et al., 2007; Lozar and Mellado, 2017). Furthermore, reproducing the observed second- and third-order moments of the vertical velocity has posed difficulties, with some simulations showing an increase of variance of the vertical velocity (Bretherton et al., 2007; Ackerman et al., 2009), while others show a decrease (Hill et al., 2009). To the best of our knowledge, previous works have not modeled the full vertical extent of the STBL at a resolution fine enough to account for turbulent eddies in the cloud-top region, whilst adequately representing the transfer of moisture within the vertical column.

We quantify the effect of droplet sedimentation through DNS of the entire boundary layer. In doing so, we aim to capture both the interactions of small-scale processes that generate turbulence and the large-scale eddies that transport moisture into the cloud. We consider the full STBL to discern the role of radiative and evaporative cooling in entrainment reduction by sedimentation, as well as the reallocation of moisture between updrafts and downdrafts. A systematic approach is taken to test how varying strengths of droplet sedimentation affect the cloud dynamics and the mixing rate between the cloud and environmental air, quantified as the mean entrainment velocity. While recognizing that sedimentation is often studied alongside aerosol effects, here we focus exclusively on sedimentation by designating the sedimentation flux in the governing equations to a one-moment microphysics scheme. This simplification in microphysical modeling frees up computational resources for a more in-depth study of the turbulence processes. The research questions we address are the following: at meter-scale resolution, what is the magnitude of entrainment reduction by sedimentation when the whole STBL is simulated? How does the decrease in mean entrainment velocity link to changes in the turbulence intensity? How does this mechanism depend on the Reynolds number?

We use DNS to reduce the uncertainty associated with turbulent models and numerical artifacts. The disadvantage of DNS is that the Reynolds number of the simulations cannot currently match the real values of the atmospheric and engineering applications. One needs to understand the role of the lower Reynolds number and the possibility of Reynolds number similarity in some turbulence properties (Orszag and Patterson Jr, 1972; Rogallo and Moin, 1984; Moin and Mahesh, 1998; Mellado et al., 2018). From dimensional analysis and the definition of the Reynolds number, one can interpret the lower Reynolds number as a smaller length scale and velocity scale, or as a larger molecular viscosity (and correspondingly, the Kolmogorov scales in the simulation are larger than in the real application that motivates the study). We adopt this latter approach and follow previous DNS work on the topic of cloud-top entrainment in stratocumulus clouds (Mellado, 2010; Lozar and Mellado, 2015b; Mellado et al., 2018). A thorough discussion is presented in Section A.2 and Section A.3.

A.2 FORMULATION

A.2.1 *Governing equations*

To evaluate the importance of droplet sedimentation to cloud-top entrainment, we use DNS to simulate conditions representative of marine stratocumulus clouds. For this, our reference case is taken from the first research flight (RF01) of the DYCOMS-II field measurement campaign (Stevens, 2005). The environmental conditions are characteristic of upwelling regions commonly found in the subtropical highs at the eastward ends of ocean basins, where abrupt changes in temperature and moisture occur along the boundaries between the cloud and the free troposphere. At the transition zone between the turbulence and non-turbulence regions, referred to as the entrainment zone, the strong inversion counteracts convective eddies, preventing them from deepening the cloud. We exclude the effects of the diurnal cycle and shortwave radiation, and consider a cloud regime that is closed-cell, warm, non-precipitating, and in a quasi-steady state.

The evolution equations for mass, momentum, and energy are formulated using the anelastic approximation, based on the rationale that the velocities within the STBL and the density variations compared to the mean are typically small. The detailed formulation can be found elsewhere (Mellado, 2010; Lozar and Mellado, 2014; Mellado et al., 2018), but we summarize it here for convenience. The governing equations can be written as

$$\nabla \cdot (\rho_{\mathrm{ref}} \mathbf{u}) = 0 \,, \tag{2}$$

$$\rho_{\mathrm{ref}} D_t \mathbf{u} = -\nabla p + \mu_g \nabla^2 \mathbf{u} + g(\rho_{\mathrm{ref}} - \rho)\mathbf{k} + \rho_{\mathrm{ref}} \omega \partial_z \mathbf{u} \,, \tag{3}$$

$$\rho_{\mathrm{ref}} D_t h = \nabla \cdot [\rho \kappa_h \nabla h - \mathbf{j}_\mu (h_l - h) - \mathbf{j}_r] + \rho_{\mathrm{ref}} \omega \partial_z h \,, \tag{4}$$

$$\rho_{\mathrm{ref}} D_t q_t = \nabla \cdot [\rho \kappa_v \nabla q_t - \mathbf{j}_\mu (1 - q_t)] + \rho_{\mathrm{ref}} \omega \partial_z q_t \,, \tag{5}$$

where the enthalpy and potential energy are nested in the liquid-water static energy, $h \equiv [c_d + q_t(c_v - c_d)]T - q_l l_v + gz$. In line with common practice, D_t is the material derivative operator, ρ_{ref} is the reference density profile (from a reference hydrostatic balance), $\mathbf{u}$ is the velocity vector of the mixture of air and water, ω is the large-scale subsidence velocity, q_t the total-water specific humidity, q_l the liquid-water specific humidity, g the magnitude of gravitational acceleration, μ_g the dynamic viscosity of the environmental air, κ_h the thermal diffusivity, κ_v the diffusivity of water vapor in dry air, $h_l = c_v T - l_v + gz$ the static energy of liquid water only, $l_v = l_v^0 - (c_l - c_v)(T - T^0)$ is the enthalpy of vaporization, and c_d, c_v and c_l are the specific heat capacities at constant pressure for dry air, water vapor, and liquid water, respectively. We use saturation adjustment, i.e., we assume instantaneous evaporation and condensation, ensuring continuous phase equilibrium. The longwave radiative flux, $\mathbf{j}_r$, is computed using a one-dimensional, vertically aligned radiative forcing model, following the approach of Stevens, 2005; Larson et al., 2007. The explicit formulation of the radiative flux can be found in Mellado et al., 2018.

For the sedimentation, we adopt a one-moment bulk microphysics scheme similar to Ackerman et al., 2004; Bretherton et al., 2007; Ackerman et al., 2009, and combine it with DNS as done in Lozar and Mellado, 2017; Schulz and Mellado, 2019. By using a simplified microphysical model, we concentrate all computational resources on improving the resolution of turbulence. At the same time, using the same microphysical model as in those earlier cases allows for a direct comparison. If we consider the water droplets to be spherical, the bulk liquid water content can be expressed as $\rho q_l = (\pi/6)\rho_l N_d d_v^3$, where N_d is the droplet number density and ρ_l the density of liquid water. The nth moment of the droplet size distribution (DSD) is denoted as $\overline{d^n} = (\overline{d^3})^{n/3} \exp[n(n-3)(\sigma^2/2)]$, in which case, $d_v \equiv (\overline{d^3})^{1/3}$ is the volume-mean droplet diameter. If we ignore inertial effects in a first approximation, the momentum balance of the droplets is equilibrated between their weight and the drag produced in a Stokes' regime. The sedimentation mass flux density of liquid water relative to the air becomes

$$\mathbf{j}_\mu = -\pi(108\mu_g)^{-1}\rho_l^2 N_d \overline{d^5} g\mathbf{k} \,. \tag{6}$$

In the previous evolution equations, $\mathbf{u}$ is the velocity of the mixture instead of the velocity of the air only, which explains the factors $h_l - h$ and $1 - q_t$ multiplying $\mathbf{j}_\mu$ in equations (4) and (5), respectively. For convenience, we will refer to $\mathbf{j}_\mu$ simply as the sedimentation flux, unless otherwise stated. Importantly, the sedimentation flux depends on the fifth moment of the DSD, meaning that the number of large droplets, or the extent of the DSD tail, plays a crucial role in determining the strength of sedimentation.

Following the references above, we assume a log-normal distribution for the DSD, such that an analytical solution exists for the moments of distribution in the form $\overline{d^n} = (\overline{d^3})^{n/3} \exp(n(n-3)(\sigma^2/2))$. We can write the sedimentation flux as $\mathbf{j}_\mu = -\rho q_l w_s \mathbf{k}$, where the quantity

$$w_s = g\rho_l d_v^2/(18\mu_g)\exp[5(\log \sigma_{gc})^2] \tag{7}$$

can be interpreted as a bulk sedimentation velocity. The sedimentation flux is thereby determined by the product of the liquid water partial density and the

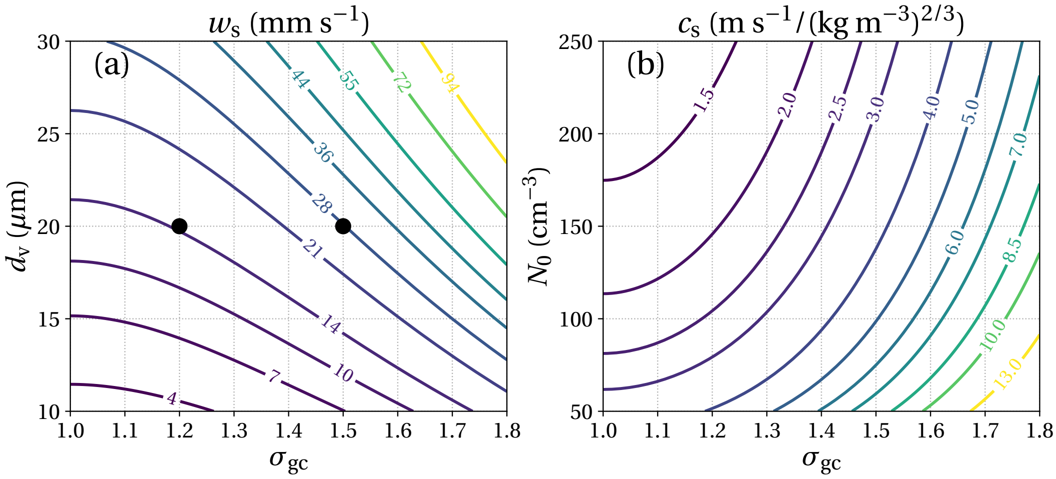

Figure A.1: Contour plots of (a) bulk sedimentation velocity w_s as a function of the volume-mean droplet diameter and the geometric standard deviation of a log-normal distribution, and (b) bulk sedimentation coefficient c_s as a function of the droplet number density and the geometric standard deviation. The markers in the left panel illustrate how typical values of σ_{gc} at a fixed d_v can double the bulk sedimentation velocity.

bulk velocity. By expressing the sedimentation flux through a single parameter like w_s, we can efficiently encompass the spectrum of all other parameters, such as the geometric standard deviation $\sigma_{gc} \equiv e^{\sigma}$ and the mean droplet size diameter d_v. Figure A.1a shows this functional relationship of w_s, with markers indicating fixed d_v values at 20 μm as characteristic of the DYCOMS-II reference case. We see that an increase in the tail of the DSD, through adjusting σ_{gc} from 1.2 to 1.5, as estimated from the observations and considered in previous studies (Ackerman et al., 2004; Bretherton et al., 2007; Schulz and Mellado, 2019), leads to a twofold increase in the bulk sedimentation velocity.

In a one-moment bulk microphysics scheme, however, setting the droplet number density equal to a constant, $N_d = N_o$, implies that $d_v = [6\rho q_l/(\pi\rho_l N_o)]^{1/3}$ and N_0 becomes the control parameter instead of d_v. The sedimentation flux may then be expressed as

$$\mathbf{j}_\mu = -c_s(\rho q_l)^{5/3}\mathbf{k}\,, \tag{8}$$

where

$$c_s = \frac{g\rho_l}{18\mu_g}\left(\frac{6}{\pi\rho_l N_0}\right)^{2/3}\exp[5(\log\sigma_{gc})^2] \tag{9}$$

is referred to as the bulk sedimentation coefficient. This formulation is convenient because for sensitivity studies, we only need to modify c_s rather than N_0 and σ_{gc} separately, thereby simplifying matters and reducing the number of simulations we need to perform. The isolines in Figure A.1b represent various combinations of N_0 and σ_{gc} for a constant c_s. For example, the case with $N_0 = 140$ cm^{-3} and $\sigma_{gc} = 1.35$ is roughly equivalent to the case with $N_0 = 100$ cm^{-3} and $\sigma_{gc} = 1.2$, as in both scenarios $c_s \approx 2.7$ m s^{-1}/(kg m^{-3})$^{2/3}$. From Figure A.1b, we choose appropriate isolines for our sensitivity studies on sedimentation strength c_s, as discussed in the next section.

A.2.2 *Description of the simulations*

Table 1: Table of experiments: Dependence of cloud properties on the Reynolds number, Re_0, and sedimentation strength, c_s.

Re_0	η_0 (m)	$\mathrm{Re}_{t,\max}$	c_s ($\mathrm{m\ s^{-1}/(kg\ m^{-3})^{2/3}}$)	LWP ($\mathrm{g\ m^{-2}}$)	w_e ($\mathrm{mm\ s^{-1}}$)	$\mathrm{CF}_{\max}$
2000	2.8	413	0	14.3	4.5	0.78
			2.7	17.3	4.3	0.82
			5.4	20.3	4.1	0.82
5000	1.4	3075	0	34.9	5.4	0.97
			2.7	41.5	5.0	0.97
			5.4	47.4	4.5	0.97
12500	0.7	11186	0	55.3	6.1	0.99
			2.7	59.5	5.0	0.99

η is the Kolmogorov scale, $\mathrm{CF}_{\max}$ represents the maximum value of the height-dependent cloud fraction, and $\mathrm{Re}_t \equiv \mathrm{TKE}^2/(\nu\epsilon)$ the turbulent Reynolds number, where TKE is the turbulence kinetic energy and ϵ is the viscous dissipation rate. The grid spacing is $\approx 1.5\ \eta_0$. DYCOMS-II based reference state is the case $\eta_0 = 1.4$ m and $c_0 = 2.7\ \mathrm{m\ s^{-1}/(kg\ m^{-3})^{2/3}}$. LWP and w_e were temporally averaged from the first hour onward. The grid dimensions (BxH) for ascending Reynolds numbers are: $1536^2 \times 384$, $3072^2 \times 768$, and $6144^2 \times 1536$.

We now outline the key parameters used in our simulations, focusing on their physical relevance and computational feasibility. In general, we use the bulk formulation described in the previous section and test scenarios where the bulk sedimentation coefficient and Reynolds number are systematically varied.

Previous works have considered $N_0 = 140\ \mathrm{cm^{-3}}$ and $\sigma_{gc} = 1.2 - 1.5$ (Ackerman et al., 2004; Bretherton et al., 2007; Schulz and Mellado, 2019). For a mean value $\sigma_{gc} = 1.35$ within that interval of geometric standard deviations, we find $c_s \approx 2.7\ \mathrm{m\ s^{-1}/(kg\ m^{-3})^{2/3}}$. Therefore, we examine the sensitivity to droplet sedimentation by evaluating three sedimentation strengths: a no-sedimentation case ($c_s = 0$), a reference case ($c_s = 2.7\ \mathrm{mm\ s^{-1}/(kg\ m^{-3})^{2/3}}$), and a high sedimentation case ($c_s = 5.4\ \mathrm{m\ s^{-1}/(kg\ m^{-3})^{2/3}}$).

The remaining parameters of the simulations are detailed in Mellado et al., 2018, which considered the cases with no sedimentation. An additional difference in this study is the slightly larger horizontal extent of the domain, with 6.7 km and a maximum of 6144 grid points per horizontal direction, instead of 5.6 km and 5120 grid points. This modification was motivated by the parallelization requirements in the supercomputer SuperMUC-NG at the Leibniz Supercomputing Centre, which needed to be a multiple of 3.

While we survey environmental conditions ordinary to the subtropical highs and use dimensional analysis to match all parameters to observations, the Reynolds number, Re, remains an exception. Current computational capabilities allow for Re values of approximately $\mathcal{O}(10^4)$, which fall far below the actual $\mathcal{O}(10^8)$ values typical of a subtropical STBL. Fortunately, a number of important statistical properties become independent of Re once it surpasses a critical threshold. When a variable reaches statistical convergence with respect to Re, we call this Reynolds number similarity (Monin and Yaglom, 2013; Mellado et al., 2018). We also conduct sensitivity experiments on Re to evaluate Reynolds number similarity and explore the feasibility of extrapolating our cloud conditions of DYCOMS-II to those in the atmosphere. In total, we perform three sets of experiments, using the DYCOMS-II case as the reference with $c_0 = 2.7\ \mathrm{mm\ s^{-1}/(kg\ m^{-3})^{2/3}}$ and a reference Reynolds number of $Re_0 = 5000$. The simulation parameters that are relevant for the following discussion are summarized in Table 2.

For convenience, the Reynolds number of our simulations will also be indicated in terms of the Kolmogorov scale η_0 corresponding to the conditions of the RF01 in DYCOMS-II. To this aim, we use the relationship $\eta_0/H = Re_0^{-3/4}$, where $H = 840$ m is the reference inversion height of the STBL. In case needed, the corresponding dynamic viscosity can be obtained from the definition of the reference Reynolds number $Re_0 = \rho_0 H U_0/\mu_g$. For this, we first need a reference velocity U_0, which is obtained using the convective velocity scale defined by Deardorff et al., 1970 as $U_0 = (B_0 H)^{1/3}$. Here, $B_0 \equiv g(\rho_0 c_0 T_0)^{-1} F_{r,ct}$ is the buoyancy flux associated with the longwave radiative flux at cloud top, $F_{r,ct} = 70\ \mathrm{W\ m^{-2}}$, according to the one-dimensional model of Stevens et al., 2005. The different Re_0 cases and their associated grid sizes, detailed in Table 2, each correspond to unique values of U_0 and μ_g. For the largest Reynolds number, $Re_0 = 12500$, and using $T_0 = 298$ K, $c_0 = 1007\ \mathrm{J\ K^{-1}\ kg^{-1}}$, and $\rho_0 = p_0/(R_0 T_0) = 1.169\ \mathrm{kg\ m^{-3}}$, where $p_0 = 10^5$ Pa and $R_0 = 287\ \mathrm{J\ K^{-1}\ kg^{-1}}$, we find $U_0 = 1.18\ \mathrm{m\ s^{-1}}$ and a dynamic viscosity of $\mu_g = 9.27 \times 10^{-2}\ \mathrm{kg\ m^{-1}\ s^{-1}}$.

The grid spacing is uniform across all directions, except where it is refined vertically near the surface to resolve the viscous sublayer, and where it is extended in the free troposphere, all without incurring an excessive number of grid points. Thanks to our use of compact, spectral-like numerical algorithms, we can achieve a grid spacing of about $1.5\eta_0$ or less, allowing the Kolmogorov scale to be $\eta_0 = 0.7$ m. If $\Delta x \gg \eta_0$, energy dissipation at small scales would be poor, leading to energy accumulation and divergence of the DNS. For ascending Reynolds numbers, Δx decreases from 4.4 m to 2.2 m to 1.1 m, and the time step Δt shortens from 1.4 s to 0.9 s to 0.5 s.

Scaling the problem to computationally feasible Reynolds numbers, $\mathcal{O}(10^4)$, opens up multiple and equally valid interpretations. These could involve viewing the system as a laboratory experiment with a boundary layer scaled to less than a meter, or alternatively, increasing the fluid viscosity by several orders of magnitude, which would shift the Kolmogorov scale to $100-1000$ cm. Regardless of the interpretation, the range of length scales in the Richardson cascade is shortened

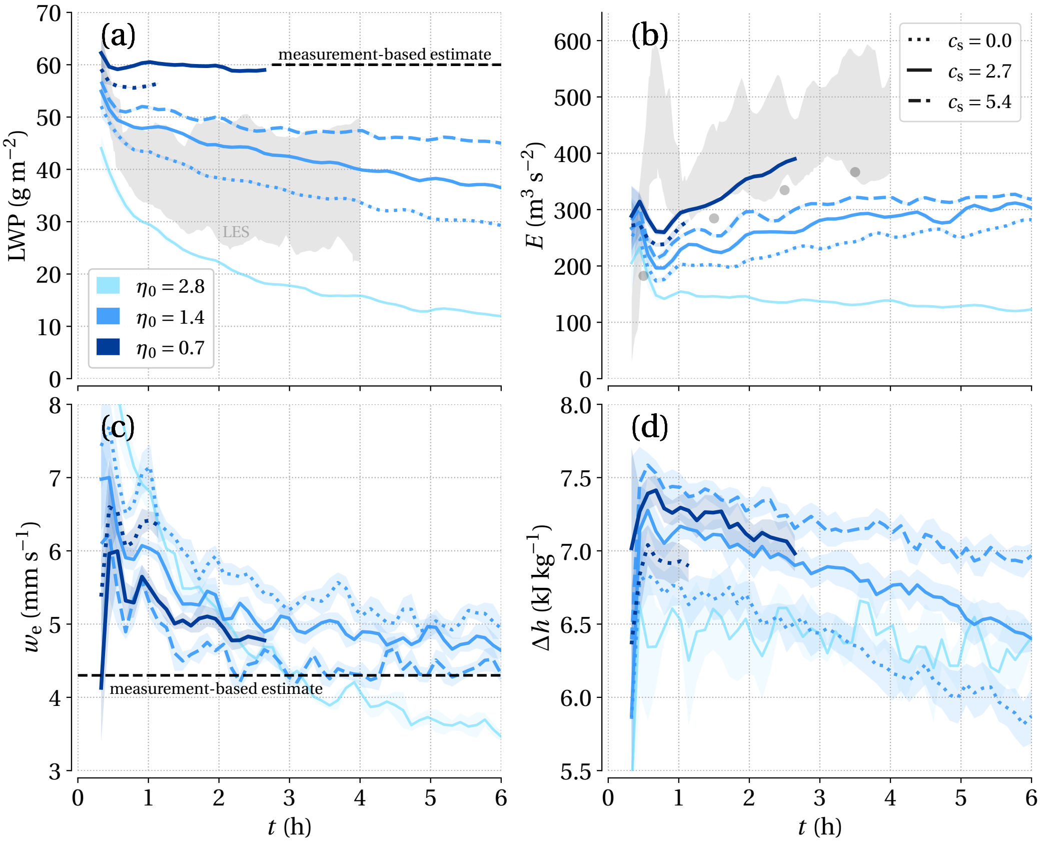

Figure A.2: (a) Temporal evolution of liquid water path (LWP) and (b) vertically integrated turbulence kinetic energy (E) for three different Kolmogorov numbers (equivalent to changes in the Reynolds number, see Table. 2) and three droplet sedimentation strengths. The gray region corresponds to the central half of the distribution of the LES ensemble in Stevens, 2005, while the dashed black line indicates measurement-based estimates. LES data for TKE includes subfilter as diagnosed in Stevens, 2005, while the gray markers indicate $(\langle u'^2\rangle + \langle v'^2\rangle + \langle w'^2\rangle)/2$ averaged for each of the first 4 hours. (c) Temporal evolution of mean entrainment velocity (w_e), or change in the inversion height defined as the minimum turbulent flux of liquid-water static energy h, and (d) the jump in h at the cloud-top inversion. For all cases, a running average over a 10 min window is applied, with the standard deviation indicated by a shaded region. The respective units in the legends are η_0: m and c_s: mm s^{-1}/(kg m^{-3})$^{2/3}$.

but remains fully resolved. DNS solves the Navier-Stokes equations without turbulence parameterizations or their ensuing uncertainties. Appendix A.8.1 shows that for a fixed Reynolds number, the results for LWP and the vertically integrated turbulence kinetic energy (E) are independent of the grid spacing.

Additional sensitivity studies concerning initial conditions and horizontal domain size are also provided in the Appendix A.8.1. We investigate how sensitive the system is to its initial conditions by running simulations that start with a specific sedimentation strength, c_s, and are then changed after 1.5 hours. We find that LWP responds more slowly than E. This lag occurs because the moisture flux from the ocean surface into the boundary layer is fixed. Secondly, numerical adjustments from doubling the horizontal extent have no noticeable effect on either the LWP or E, suggesting that our results are also robust to changes in domain size.

A.3 COMPARISON WITH OBSERVATIONS AND REYNOLDS NUMBER EFFECT

Before discussing the effect of sedimentation on STBL properties, this section compares our DNS results to available observations and previous LES studies. The aim is to understand how well the DNS data represents the effect of sedimentation, given the different modeling assumptions that we need to make and, in particular, the difference in Reynolds numbers between the simulations and the atmospheric conditions. For this purpose, we consider the LWP, the turbulence kinetic energy and the mean entrainment velocity, which are properties that we will also consider later on in the discussion of sedimentation effects.

Figure A.2a shows the temporal evolution of LWP for different sedimentation and Reynolds numbers. Following the initial spin-up phase during the first 20 minutes of simulation, we see that the sedimentation case $\eta_0 = 0.7$ m, corresponding to a grid spacing of 1.1 m, is quasi-steady over time and agrees particularly well to the measurement-based estimate of 60 g m^{-2}, without the need for parameter tuning. In contrast, LES studies (represented by the gray-shaded regions) need to be tuned by considering a grid aspect ratio between 5:1 and 10:1 and typically underestimate LWP (Mellado et al., 2018). This illustrates an advantage of DNS; the disadvantage is the high computational cost, as that particular simulation required 44 million-core hours, using 24,576 cores in SuperMUC-NG at the Leibniz Supercomputing Centre. As a result, the sedimentation case $\eta_0 = 0.7$ m could only be run up to 2.7 h due to constraints in the computational resources, whereas the no-sedimentation case $\eta_0 = 0.7$ m was also limited, running for only 1.1 h.

Figure A.2b shows that the temporal evolution of vertically integrated turbulence kinetic energy (E) in the DNS sedimentation case with $\eta_0 = 0.7$ m agrees more closely with LES studies (gray-shaded regions) than the corresponding comparison for LWP. The DNS cases with $\eta_0 = 1.4$ m have a significantly lower turbulence kinetic energy than the LES cases. An argument for this mismatch of E might be the horizontal domain size, as the LES used a domain measuring 3.36 km horizontally, whereas our domain spans 6.76 km in each direction. It is possible that certain domain sizes favor particular deep-convective structures. However, as already pointed to above, our analysis in Appendix A.8.1 shows no discernible difference from doubling the domain size in the DNS. The observed differences between the LES and DNS is then likely attributed to the role of the subgrid scale model and the LES tuning. To better understand this effect, we computed $E = (\langle u'^2 \rangle + \langle v'^2 \rangle + \langle w'^2 \rangle)/2$ using only the LES resolved fields and plotted the average for each of the first four available hours in Figure A.2b, where they fall between the $\eta_0 = 1.4$ m and $\eta_0 = 0.7$ m cases. This indicates that the subgrid scale contribution to the turbulence kinetic energy is comparable to the Reynolds number effect in the DNS, which is consistent with the idea that the subgrid scale model in LES can be interpreted as a low Reynolds number effect (Mellado et al., 2018). This analysis also shows that LES can capture some important properties like the turbulence kinetic energy correctly at a much lower computational cost than DNS, which is the goal and advantage of LES, but with the premise that it is correctly tuned. This is where DNS can help by providing reference data for cases where observations are not available.

The third property that we consider is the mean entrainment velocity. In accordance to Lilly, 1968, we define the mean entrainment velocity as

$$w_e = \frac{dz_i}{dt} - \langle w \rangle_{z_i} , \tag{10}$$

where z_i is the inversion height, angle brackets denote horizontal averages, and the subscript z_i indicates that the corresponding function is particularized at $z = z_i$. The mean vertical velocity is $\langle w \rangle = -\omega$, and $\omega = Dz$ is the subsidence velocity with a constant divergence $D = 3.75 \times 10^{-6}\ \mathrm{s}^{-1}$. Different definitions of the inversion height z_i can be considered. Even if the total sum is less contingent on the chosen z_i when the cloud-top region is in a quasi-steady state, Schulz and Mellado, 2018 showed that individual contributions to the mean entrainment velocity from different physical phenomena depend on z_i, making the specific choice of z_i important for comparing individual contributions across studies. In this study, we define z_i as the minimum turbulent flux of the liquid-water static energy, h.

To avoid the noise introduced when calculating the derivative of $z_i(t)$ in Eq. 10, we calculate the mean entrainment velocity from the entrainment-rate equation. Further details regarding this calculation will be provided in section A.5. Figure A.2c shows that, much like the LWP, the DNS case $\eta_0 = 0.7$ m tends to best reproduce observational data for w_e. Compared with measurements that estimate w_e to be in the range $3.9 - 4.7$ mm s^{-1} (Faloona et al., 2005; Stevens et al., 2003), our estimates lean towards the upper bound, with a value of 4.9 mm s^{-1} for the sedimentation case $\eta_0 = 0.7$ m (see Table. 2). To calculate w_e, we will see in section A.5 that we require the increment in mean properties at height z_i. Figure A.2d shows the temporal evolution of the increment in liquid water static energy at height z_i, Δh, which aligns with typical values for stratocumulus clouds ranging from $5 - 12$ kJ kg^{-1}.

The case $\eta_0 = 0.7$ m shows the best agreement with measurements in the vertical distribution of mean liquid water content (LWC) as seen in Figure A.3a, as well as in the variance, $\langle w'^2 \rangle$, and skewness, $\langle w'^3 \rangle$, of the vertical velocity w in Figs. A.3c-d. The positive buoyancy flux in Figure A.3b for the case $\eta_0 = 0.7$ m points to turbulence production in both the cloud layer and the subcloud layers. Lower Reynolds number cases (with Kolmogorov scales $\eta_0 = 2.8$ and $\eta_0 = 1.4$ m) tend to suppress $\langle w'^2 \rangle$ within the STBL and show minimal to no regions of negative $\langle w'^3 \rangle$. The case $\eta_0 = 0.7$ m with a grid spacing of 1.1 m comes closest to matching this region of negative skewness. LES simulations, by contrast, have

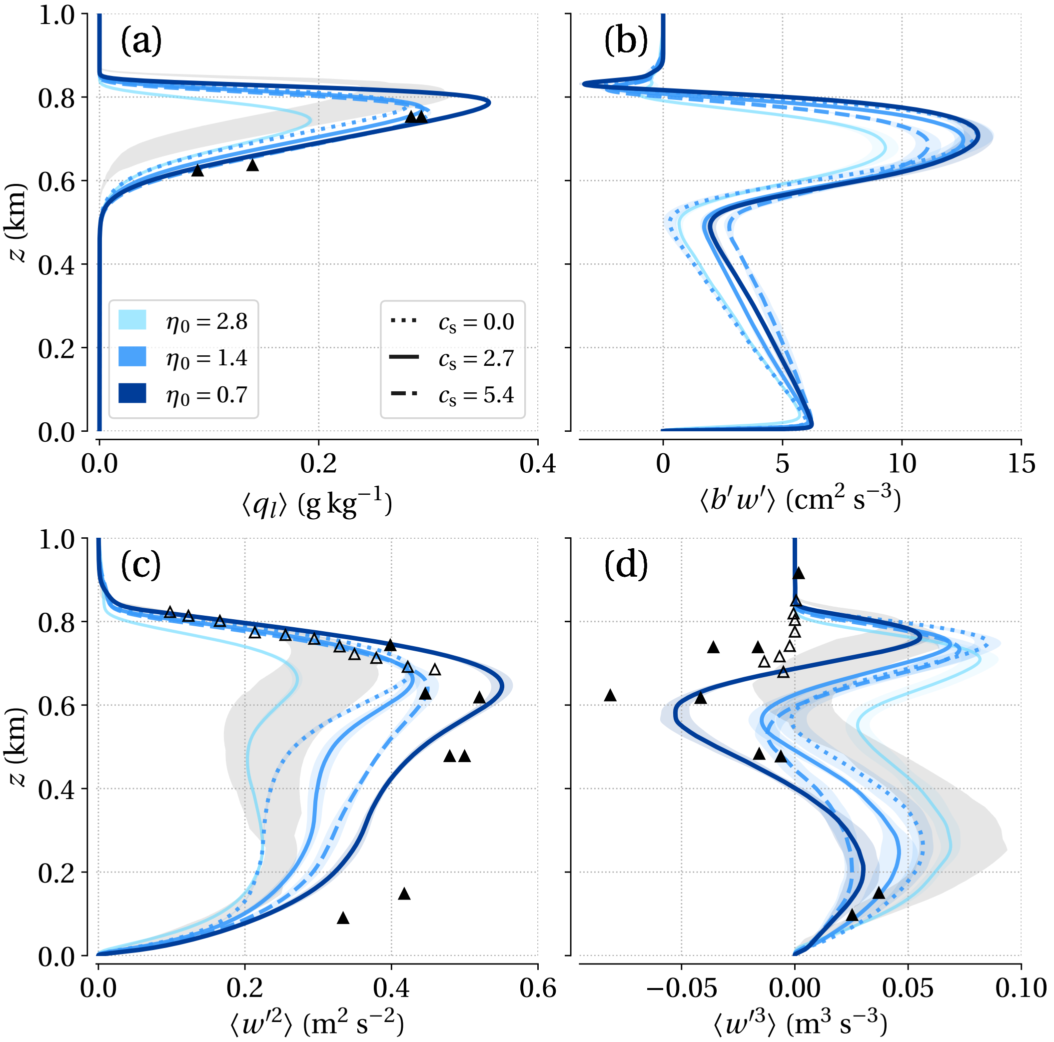

Figure A.3: Vertical profile of (a) liquid water content, (b) buoyancy flux, (c) the variance, and (d) the skewness of the vertical velocity, time-averaged from the first hour onward. Markers indicate measurements reported by Stevens, 2005, with hollow triangles representing radar data. For all cases, shaded regions indicate the standard deviation. The respective units in the legends are η_0: m and c_s: mm s^{-1}/(kg m^{-3})$^{2/3}$.

consistently reported positive skewness throughout the STBL, which is more characteristic of cumuliform convection.

Last, we consider Reynolds number effects. By comparing results at different Reynolds numbers in Figure A.2 and Figure A.3, we observe that the effect of the Reynolds number on all properties is substantial. In general, we find that increasing the Reynolds number increases LWP and cloud fraction (see Figure A.6a for vertical distribution of cloud fraction), which brings about stronger LW radiative cooling and more turbulence. This effect of the Reynolds number can be interpreted as reduced mixing in the cloud-top region (further discussion is presented in section A.5).

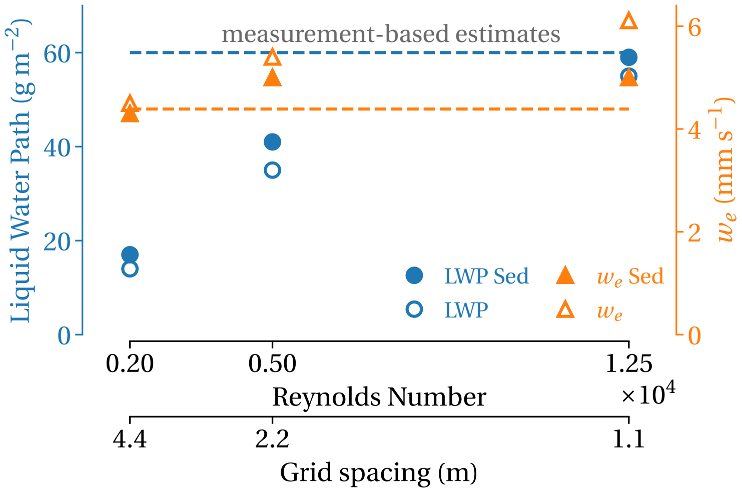

Figure A.4: Dependence of the cloud liquid water content and mean entrainment velocity on sedimentation strength and Reynolds number. Time averaged from the first hour onward for all simulations. Filled-in shapes are simulations with reference sedimentation strength from DYCOMS-II and hollow shapes with no sedimentation. Measurement-based estimates for LWP (dotted blue) and mean entrainment velocity w_e (dotted orange) are shown, with w_e taken as the average of the estimated range of $3.9 - 4.8$ mm s^{-1}.

Nevertheless, despite the substantial effect of the Reynolds number found in all properties, we begin to observe convergence for the large Reynolds number $\mathrm{Re}_0 = 12500$, or $\eta_0 = 0.7$ m. For clarity, we integrated the LWP from the first hour onward for each simulation to yield a single value per simulation, shown in Figure A.4. The same approach is applied to the mean entrainment velocity w_e from Figure A.2c. We see that the relative change in LWP and w_e between the cases $\eta_0 = 2.8$ m and $\eta_0 = 1.4$ m is larger than that between $\eta_0 = 1.4$ m and $\eta_0 = 0.7$ m. For simulations with sedimentation included (indicated by filled shapes in Figure A.4), both LWP and w_e gradually approach their respective measurement-based estimates as Re_0 increases. This convergence pattern suggests a progression toward Reynolds number similarity for LWP and more prominently for w_e, and allows for extrapolation of the results to the higher Reynolds numbers that are characteristic of atmospheric conditions.

Besides, we observe that the difference between simulations with and without sedimentation (indicated by filled and hollow shapes) for w_e grows with increasing Re_0. For lower Reynolds numbers ($\eta_0 = 1.4$ and $\eta_0 = 2.8$ m), the effect of sedimentation on w_e is less pronounced. But at meter-scale resolution ($\eta_0 = 0.7$ m), sedimentation causes at least a 20% decrease in mean entrainment velocity. Arguably more important, at higher Reynolds numbers, sedimentation-induced changes in w_e are comparable to or exceed those caused by Reynolds number effects. At $\eta_0 = 0.7$ m, the sedimentation effect outweighs Reynolds number effects for the mean entrainment velocity, giving us confidence that the DNS data can disentangle at least part of the interactions between sedimentation and turbulence.

The effect of sedimentation in Figure A.2a reveals a clear trend: increases in sedimentation strength result in higher LWP. The reduction in cloud-top evaporation, which was already proposed and observed by Bretherton et al., 2007; Ackerman et al., 2009, allows for greater distribution of liquid water across turbulent eddies throughout the STBL. Figure A.3a illustrates a thicker cloud deck and an increase in the maximum of the vertical LWC distribution. Overall, sedimentation lowers the mean cloud height and reduces the rate of evaporation at the cloud top.

The distribution of LWC within the STBL modulates buoyancy-driven and turbulent processes. Our results align with those of Bretherton et al., 2007; Ackerman et al., 2009, showing that convective intensity, measured by $\langle w'^2 \rangle$, increases with sedimentation strength across the entire STBL (Figure A.3c), and is correlated with greater cloud liquid water content. Whether LWP increases or decreases with sedimentation strength also depends on meteorological conditions, such as free-troposphere humidity and STBL stratification (Ackerman et al., 2004; Ackerman et al., 2009). In RF01, where the free troposphere was dry, LWP is maintained by deep circulations that continuously supply moisture to the cloud layer. To counteract the desiccating influence of the dry free troposphere, convective intensity, driven by radiative cooling and the evaporation of liquid water, must at least remain steady. In our simulations, convective intensity increases (see the time evolution of E in Figure A.2b), which we interpret as contributing to the growth of the boundary layer. Liquid water and water vapor are then redistributed throughout the boundary layer, organizing turbulence into more coherent large-scale structures.

Cloud-top negative values in the buoyancy flux profile (Figure A.3b) can be attributed to the downward entrainment of positively buoyant warm air. Near the cloud base, the buoyancy flux approaches negative values in the no-sedimentation case, suggesting a potential separation between the cloud and the subcloud layers (Nicholls, 1984; Bretherton and Wyant, 1997). In the sedimentation cases, by contrast, the buoyancy flux is prominently positive, indicating a more coupled state. This is consistent with Figure A.2c, which shows high sensitivity of the mean entrainment velocity to increases in sedimentation strength. The reduction in cloud-top entrainment in response to increased sedimentation strength supports a more coupled STBL, in agreement with previous local cloud-only studies (Lozar and Mellado, 2014; Lozar and Mellado, 2017; Schulz and Mellado, 2019). The somewhat surprising tendency of the mean entrainment velocity to decrease as turbulence increases, however, is discussed further in the following sections.

The vertical velocity skewness (Figure A.3d) points to the organization of moisture between ascending and descending motions, highlighting asymmetries around the mean distribution (Tillman, 1972; Moeng and Rotunno, 1990). Positive skewness signals strong and narrow updrafts, surrounded by weak and broad downdrafts, and vice versa for negative skewness. Our results uncover two local maxima of positive skewness: one in the subcloud layer, associated with the surface

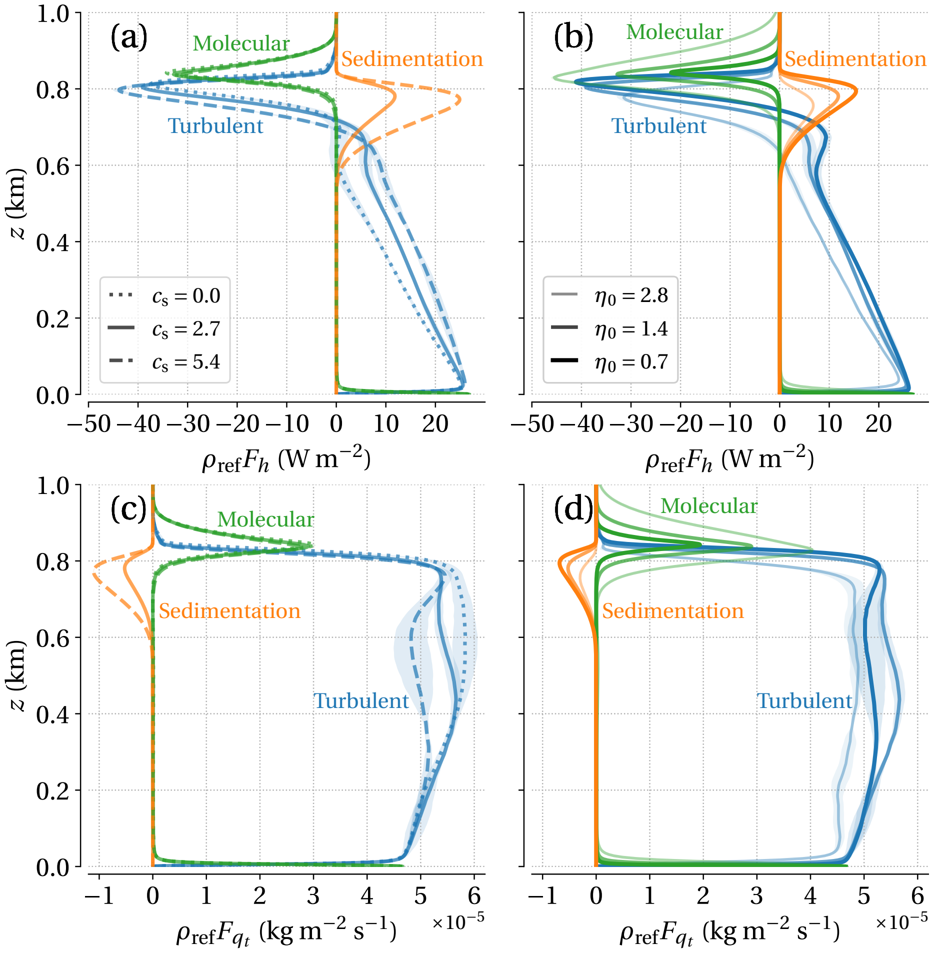

Figure A.5: Vertical profiles of the various flux contributions according to Eq. 12 of (a-b) liquid water static energy and (c-d) total water. In the left panels (effect of sedimentation), the Kolmogorov scale is set to $\eta_0 = 1.4$ m, while in the right panels (effect of Reynolds number), the sedimentation strength is kept constant at $c_s = 2.7$ mm s^{-1}/(kg m^{-3})$^{2/3}$. Different colors indicate flux contributions to the energy (Eq. 4) and total water (Eq. 5) equations. Line style indicates various sedimentation strengths, and opacity indicates different Reynolds numbers. All profiles are horizontally and time-averaged from the first hour onward, with the standard deviation indicated by a shaded region. The respective units in the legends are η_0: m and c_s: mm s^{-1}/(kg m^{-3})$^{2/3}$.

buoyancy flux, and another in the cloud layer, linked to latent heating from condensation. Between these, we observe a local minimum in the skewness, where the radiative and evaporative cooling tend to promote narrow downdrafts that compensate for the surrounding updrafts. Increasing sedimentation strength reduces the positive skewness in the subcloud layer, and the minimum around the cloud base becomes negative. This suggests that, as more moisture is available in the STBL when sedimentation increases, the downdrafts are stronger in the subcloud layer. Increasing sedimentation strength not only alters the intensity of turbulence but also reduces the asymmetry of vertical motions. Thus, both the amount and spatial distribution of moisture are important in driving mixing within the STBL.

While turbulence intensifies in the STBL, as indicated by the temporal evolution of E in Figure A.2b and $\langle w'^2 \rangle$ in Figure A.3c, it prompts the question of how this is possible when the mean entrainment velocity simultaneously decreases. To answer this, we look beyond the turbulent flux and use the entrainment-rate equation to understand the various contributions to the mean entrainment velocity.

The entrainment-rate equation provides an analytical expression for w_e and is derived by integrating the evolution equation for the fluid property ϕ from z_i upward. The fluid property per unit volume ϕ can be any of the 5 prognostic variables indicated in Section A.2; commonly, one considers the energy variable, the moisture content, or both. In this approach, the time rate-of-change of a control volume, specifically the entrainment zone, is decomposed into sources and fluxes — turbulent, molecular, radiative, and sedimentation. The fluxes tell how much mass, momentum, or energy is entering and exiting the entrainment zone. Following the work of Mellado, 2017 and Mellado et al., 2018, the entrainment-rate equation can be written as

$$w_e\big(\langle\phi\rangle_{z_i} - \phi_{bg,z_i}\big) = F_{\phi,z_i} - F_{\phi,z_\infty} + \int_{z_i}^{z_\infty} S_\phi \, dz + \frac{d}{dt}\int_{z_i}^{z_\infty} \big(\langle\phi\rangle_{z_i} - \phi_{bg,z_i}\big)\, dz \,, \qquad (11)$$

where F_ϕ is the average flux of ϕ at either the reference height of the inversion, $z = z_i$, or in the upper free troposphere where the properties correspond to a background state, $z = z_\infty$. S_ϕ serves as a source term. The final term measures the deformation of the mean profile $\langle\phi\rangle$ in a frame of reference that moves with z_i, and it becomes smaller than the other terms in the quasi-steady state, or the entrainment equilibrium state (Fedorovich et al., 2004); this is tested in Appendix A.8.2. The difference $\langle\phi\rangle_{z_i} - \phi_{bg,z_i}$ refers to the jump in the property ϕ at z_i as it ascends or descends. With DNS, all the terms in Eq. 11 are known and the resulting mean entrainment velocity has been shown in Figure A.2c. To a large extent, the entrainment-rate equation can be simplified to the form:

$$w_e\big(\langle\phi\rangle_{z_i} - \phi_{bg,z_i}\big) \approx F_{\phi,z_i} \,. \qquad (12)$$

The vertical fluxes of the liquid water static energy and total water are plotted in the top and bottom rows of Figure A.5, respectively. The left panels show the effect of varying c_s while keeping the reference Kolmogorov scale held fixed at $\eta_0 = 1.4$ m. In Figure A.5a, the individual contributions to the static energy are decomposed. As c_s increases, the droplet size distribution function shifts towards larger, heavier droplets that sediment further down from the cloud top. Since heavier droplets are less effectively transported upward by turbulent motions, sedimentation reduces the local liquid water content near the cloud top. Sedimentation ultimately leads to the "removal" of $\langle h \rangle$ from the STBL, as the remaining water vapor contains more energy than liquid water. In distinguishing the STBL interior from the entrainment zone, the sedimentation flux of h cools the STBL interior ($\partial_t\langle h\rangle < 0$, because $-\partial_z\langle h'w'\rangle < 0$) while warming the entrainment zone.

Crucially, the magnitudes of the turbulent and sedimentation contributions to the static energy flux are similar and opposite in sign. Given their potential to offset each other, they are deemed equally important in the energetics of the system. If the turbulent flux of h smooths the mean gradient of h, then the sedimentation flux of h reinforces it. The turbulent flux decreases incrementally by approximately -3 W m^{-2} between the no-sedimentation case and the sedimentation cases with $c_s = 2.7$ and $c_s = 5.4$ mm s^{-1}/(kg m^{-3})$^{2/3}$, dropping from -38 W m^{-2} to -44 W m^{-2}. Meanwhile, the sedimentation flux of h gains from 0 W m^{-2} to 12 W m^{-2}, and then to 25 W m^{-2}, producing a greater average increase in magnitude compared to the turbulent flux. This indicates that the turbulent and sedimentation fluxes of h at z_i scale differently with increasing c_s. What is important is not the total magnitude of each flux, but the incremental change associated with varying c_s. We now understand that the mean entrainment velocity decreases because the sedimentation flux of h compensates for the turbulent flux of h, with the former increasing more rapidly as sedimentation strength increases.

Let us consider the turbulent flux of q_t in Figure A.5c, representing the directional transfer of water vapor and liquid water combined. The turbulent flux of q_t decreases monotonically with increasing c_s, starting in the cloud layer and substantially more near cloud base. The variation in the turbulent flux profile of q_t comes from an increase in available liquid water and reorganization of the q_l and q_v components within the STBL. As sedimentation increases the availability of moisture in downdrafts that enter the subcloud layer, the predominantly upward turbulent flux of q_t weakens. The newly-emerged maximum in the turbulent flux of q_t in the cloud layer in sedimentation cases suggests a change in the downdraft component of the boundary-layer circulation, while conditions at the cloud top remain relatively unchanged. It is also remarkable that the turbulent flux of q_t decreases as c_s increases, even though E increases.

The effect of the Reynolds number is shown by fixing the sedimentation strength at $c_s = 2.7$ mm s^{-1}/(kg m^{-3})$^{2/3}$ (right panels of Figure A.5). For both static energy and total water, the molecular contribution in the cloud-top region is synonymous with the effect of the Reynolds number, as the molecular flux scales with the Reynolds number and the mean gradient. However, the mean profiles show weaker dependence on the Reynolds number. The most conspicuous result is the substantial molecular contribution to entrainment warming and drying, consistent with the strong dependence of LWP on the Reynolds number, as previously reported. This behavior is also shown by the vertical profile of the cloud fraction in Figure A.6a. The cloud reaches its peak fraction near the middle for the case $\eta_0 = 1.4$ m and increasingly occupies the regions toward the top and base with higher Reynolds numbers. Despite the strong dependence of entrainment fluxes on the Reynolds number, we observe that the molecular contribution diminishes rapidly with respect to the turbulent contribution when comparing the three cases with different Reynolds numbers. This further illustrates that we start to reach a certain degree of Reynolds number similarity, as molecular effects become increasingly small in some relevant properties of the system.

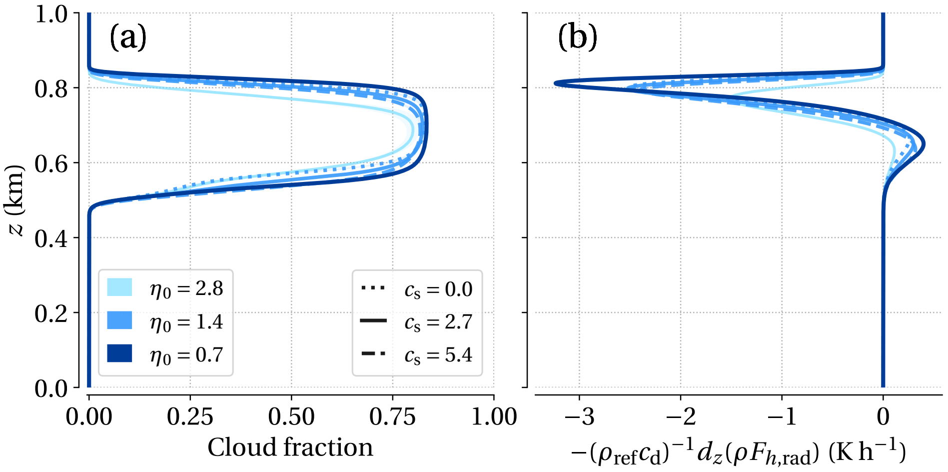

Figure A.6: Vertical profile of the (a) cloud fraction, defined by a threshold $q_l = 3 \times 10^{-6}$ g kg^{-1} and (b) radiative heating rate, time-averaged from the first hour onward, with the standard deviation indicated by a shaded region. The respective units in the legends are η_0: m and c_s: mm s^{-1}/(kg m^{-3})$^{2/3}$.

A.6 TURBULENCE AND MOISTURE ORGANIZATION

Why does turbulence intensity increase, if there is less evaporative cooling at the cloud top? We look at two possible mechanisms to explain the increase in turbulence, namely, cloud-top radiative cooling and the vertical distribution of moisture within the STBL.

Convection in stratocumulus clouds is primarily driven by longwave radiative cooling; however, as shown in Figure A.6b, the change in radiative heating rates due to sedimentation is negligible. A plausible explanation might be linked to the short optical length of cloudy air. While cloud thickness may increase with sedimentation strength, a substantial part of the cloud behaves akin to a black body for the case $c_s = 0$, and there is little impact on the overall radiative cooling effect when increasing c_s. In agreement with Bretherton et al., 2007; Ackerman et al., 2009; Lozar and Mellado, 2017, we rule out cloud-top radiative cooling as a mechanism for increased turbulence.

In analyzing the vertical distribution of moisture in the STBL, we first refer back to the buoyancy flux profile in Figure A.3b. We see that increasing sedimentation strength consistently reduces TKE buoyancy production in the cloud layer while elevating it in the subcloud layer. This shift in buoyancy production is partly attributed to reduced entrainment of warm and dry air into the cloud layer, which reduces evaporative cooling at cloud top and favors it elsewhere. The remainder of this section focuses on the latter — specifically, the vertical redistribution of liquid water and water vapor. The underlying idea is that, although the total water content in the system at a given time remains the same for different sedimentation strengths (as we fix the surface fluxes), variations in its partitioning between liquid water and water vapor can influence and reshape the organization of turbulence.

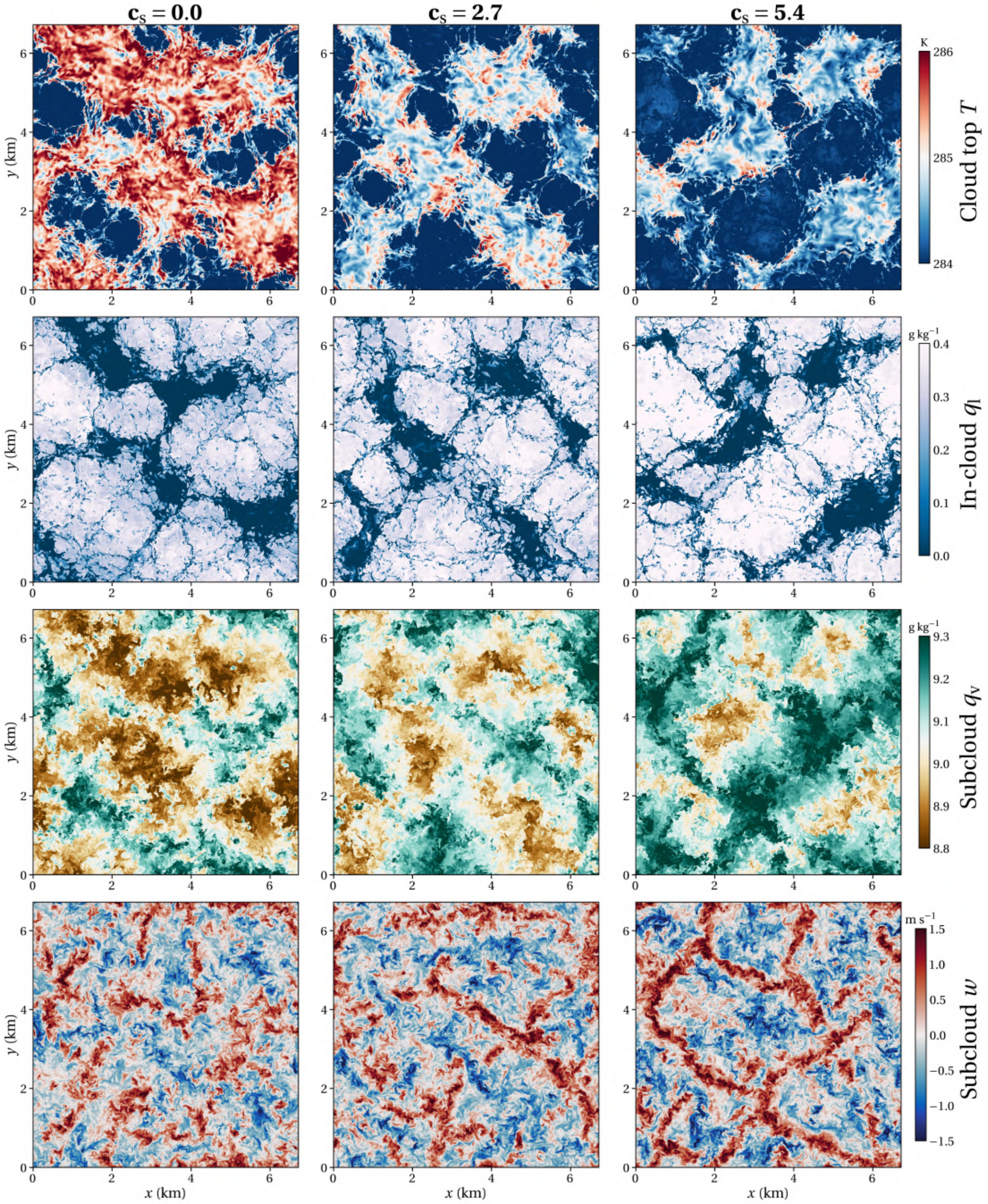

Figure A.7: Horizontal cross-sections of the temperature, liquid water and water vapor specific humidity, and vertical velocity are shown from top to bottom, respectively. Columns correspond to sedimentation strengths of $c_s = 0.0$, $c_s = 2.7$, and $c_s = 5.4$ mm $s^{-1}/(kg\ m^{-3})^{2/3}$. All cross-sections are obtained for $Re_0 = 5000$, or $\eta_0 = 1.4$ m, and at $t = 4$ h. Each variable is evaluated at a specific height, which varies with sedimentation strength, listed from left to right: temperature at the cloud top (defined by the inversion height z_i) at 847 m, 829 m, and 809 m; liquid water in the cloud layer (height of maximum q_l) at 793 m, 780 m, and 760 m; water vapor and vertical velocity in the subcloud layer (height of maximum $\langle w'^3 \rangle$ below the cloud) at 363 m, 386 m, and 365 m.

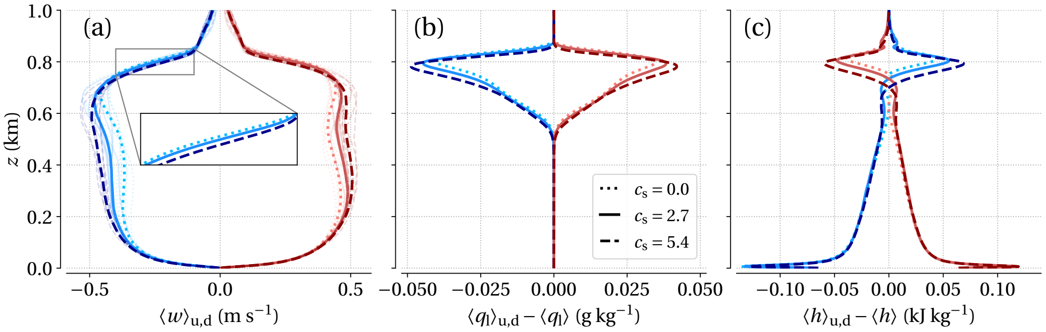

Figure A.8: Conditionally sampled vertical profiles of (a) vertical velocity, $\langle w \rangle_{u,d}$, (b) liquid water specific humidity anomaly, $\langle q_l \rangle_{u,d} - \langle q_l \rangle$, and (c) liquid water static energy anomaly, $\langle h \rangle_{u,d} - \langle h \rangle$, distinguished by updraft and downdraft regions. Consistent with the vertical velocity profiles in the last row of Figure A.7, blue lines represent downdrafts, while red lines indicate updrafts. Each simulation is conducted at a Reynolds number of $Re_0 = 5000$, or $\eta_0 = 1.4$ m. Profiles were taken at one-hour intervals (shown in the first panel with reduced opacity) and then averaged together. The units in the legend are c_s: mm $s^{-1}/(kg\ m^{-3})^{2/3}$.

We begin the analysis at the cloud top, where entrainment draws warm and dry air down from the free troposphere into the boundary layer; this process is particularly visible in the temperature cross-sections at the cloud top (see top row of Figure A.7). Sedimentation alters this process by reducing the entrainment of warm and dry air, and thus reducing the evaporation rate of water droplets near the temperature inversion.

The resulting increase in q_l with sedimentation is shown in the second row of Figure A.7 (and in Figure A.3a). This is further quantified by conditioning the fields into downdrafts and updrafts, as shown in Figure A.8. Looking at the core of the downdrafts inside the cloud, the second panel of Figure A.8 shows that, as sedimentation increases, the downdrafts contain less liquid water compared to the mean profile, $\langle q_l \rangle$ (the dry downdrafts become drier), as there is less evaporation at cloud top. While the puffy, cellular-like structure of the clouds remains consistent across all sedimentation strength scenarios, the clouds themselves grow denser with liquid water. The area of the cloud holes also remains largely unchanged, as sedimentation at this height primarily impacts the cloudy regions.

The increase in the difference of liquid content between cloudy puffs and dry holes with sedimentation strength is what fuels evaporative cooling at the sides of the holes and accelerates the downdrafts. As liquid water accumulates near the downdrafts and evaporates, the resulting negative buoyancy anomaly increases the buoyancy flux near cloud base (Figure A.3b) and serves as a source of TKE. This turbulence intensification is shown by the increase of the variance of w in Figure A.3c. Conditional analysis (Figure A.8a) shows that increasing sedimentation strength enhances downdrafts and updrafts within the subcloud layer, with a visibly larger effect on the downdrafts. The asymmetry in the vertical velocity profile is reflected by the skewness from Figure A.3d. The skewness in the subcloud layer transitions from a predominantly positive distribution to a more neutral one (less positive), further indicating a strengthening and acceleration of downdrafts.

Consistent with this turbulence intensification, the cloud holes, represented by the downdrafts in the third panel in Figure A.8, tend to contain more energy than the mean, $\langle h \rangle$. Overall, while the cloud layer cools due to reduced entrainment warming, the downdraft regions become more concentrated and energetic, as warm air is more effectively drawn in from the free troposphere through the cloud holes. The large changes in the liquid water static energy anomaly, $\langle h \rangle_{u,d} - \langle h \rangle$, help explain why sedimentation increases the entrainment turbulent flux of $\langle h \rangle$ at the cloud top (see Figure A.5a).

The reduction of entrainment drying and warming with increasing sedimentation strength results in an increase in water vapor in the subcloud layer (see third row of Figure A.7). The regions that are rich in water vapor coincide with the updrafts in the cross-section of the vertical velocity (see bottom row of Figure A.7). In particular, the cross-section of the vertical velocity taken at the subcloud layer organizes into a more connected configuration with increasing sedimentation strength, forming sheets of upward motion that interconnect into a honeycomb-like arrangement. As turbulence intensifies, the downdrafts more forcefully displace the warmer near-surface air, driving convective upward motion through the pressure gradient force (Bretherton et al., 2007; Ackerman et al., 2009; Lozar and Mellado, 2017).

These findings are summarized in Figure A.9. Droplet sedimentation pulls the cloud downwards, more at the cloud top because it is where the larger droplets are. This reduces entrainment and therefore the boundary layer is shallower. The reduction in entrainment warming and drying leads to a moister boundary layer, which manifests in more liquid water in the cloud and more water vapor in the subcloud layer. The reduction of evaporative cooling at the cloud top with increasing sedimentation also leads to a larger contrast in the cloud layer between the descending dry, warm air in the cloud holes and the moist, cold air in the cloudy puffs. This contrast enhances evaporative cooling at the boundary of the holes, accelerating the downdrafts, which increases the turbulence intensity in the boundary layer. Together, these dynamics help redistribute and circulate moisture more evenly throughout the STBL, and thereby reinforce the coupling with surface-driven buoyancy fluxes. Overall, sedimentation plays a key role in reshaping the vertical distribution of moisture and the organization of turbulence within the STBL, influencing both cloud and subcloud dynamics.

A.7 CONCLUSIONS

This study quantifies the effects of droplet sedimentation in a stratocumulus-topped boundary layer (STBL) using direct numerical simulations (DNS). Previous analyses reaching sub-meter scale resolution were confined to local cloud-top studies, whereas boundary-layer studies generally reached vertical resolutions of only 5 m, or potentially down to 2.5 m with lower-order numerics. Our evaluation

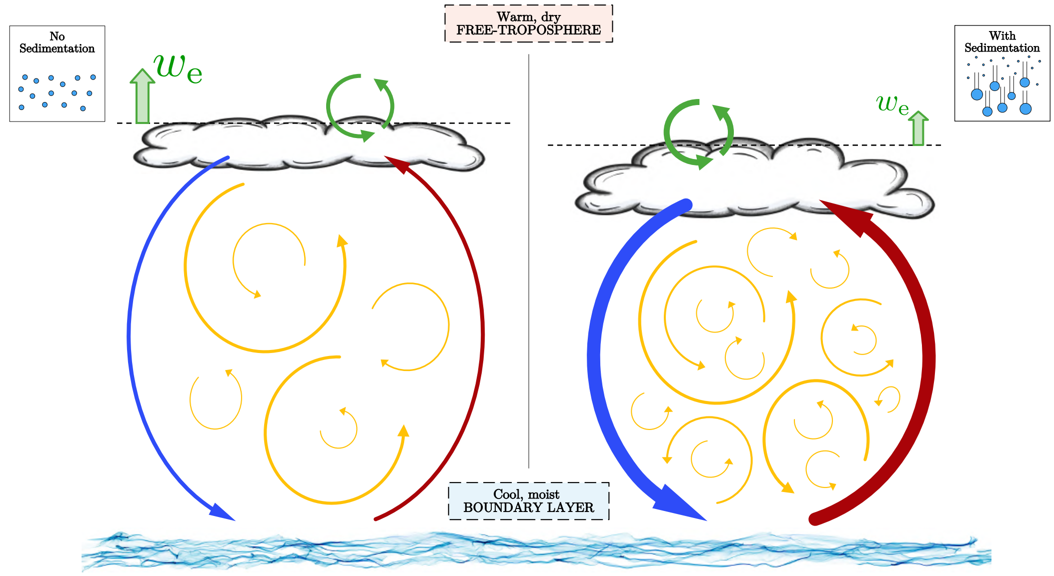

Figure A.9: The schematic illustrates the impact of droplet sedimentation on cloud amount (represented by cloud size), cloud-top height (dashed line), boundary layer turbulence (yellow arrows), mean entrainment velocity, w_e (indicated by the size of the symbol and the straight arrow connected to the cloud-top height line) and vertical velocity (blue arrows for downdrafts and red for updrafts). Line thickness indicates intensity. The entrainment turbulent flux of $\langle \mathrm{h} \rangle$ is depicted by green circular arrows.

of changes in liquid water content, and the subsequent changes in mean entrainment velocity and turbulence, involves sensitivity experiments that test varying sedimentation strengths and Reynolds numbers. Taking the first research flight of the DYCOMS-II field campaign as a reference, we find that retaining the observed bulk strength of droplet sedimentation reduces the mean entrainment velocity by at least 20% and increases the liquid water path (LWP) compared to the simulations without droplet sedimentation (as schematically summarized in Figure A.9). The magnitude of entrainment reduction is seen to increase with the Reynolds number and, for the Reynolds numbers tested here, falls between the values reported in local DNS studies conducted at sub-meter scale resolution and those from large-eddy simulation (LES) studies. We show that a vertical resolution of about 2 m is necessary to capture the signal of entrainment reduction by sedimentation with numerical algorithms of spectral-like resolution. Indeed, at a vertical resolution of about 1 m and without being tuned, our results for LWP and mean entrainment velocity start to match measurements.

Our findings challenge previous explanations of the mechanism behind reduced mean entrainment velocity by sedimentation, particularly the claim that less evaporation at the cloud top leads to reduced turbulence in the STBL. In reality, our experiments yielded a rise in both turbulence kinetic energy and the turbulent entrainment flux when the effect of droplet sedimentation is added. By means of integral analysis, we refer to the entrainment-rate equation which decomposes the mean entrainment velocity $w_\mathrm{e} = \mathrm{d}z_\mathrm{i}/\mathrm{d}t$ into its constituent fluxes: turbulent, molecular, radiative, and sedimentation fluxes. From the vertical mean fluxes of the liquid water static energy at the cloud top, we show that the sedimentation flux is commensurate in magnitude with the turbulent entrainment flux, as the former undergoes a more rapid increase with sedimentation strength. For Kolmogorov scales $\eta_0 = 1.4$ and 0.7 m, the change in sedimentation flux compensates the change in the turbulent flux, resulting in a lower mean entrainment velocity. Coarser resolutions tend to underestimate this compensation.

Sedimentation also moderates vertical motions, affecting the vertical distribution of moisture in both the cloud and subcloud layers. By decreasing the entrainment of warm, dry air from the free troposphere into the boundary layer, sedimentation reduces evaporation at the cloud top. This leads to a shallower and moister boundary layer. By conditionally sampling the updrafts and downdrafts, we show that the downdrafts become drier and warmer with increasing sedimentation strength. The sharper contrast between the warmer, drier downdrafts (cloud holes) and the cooler, moister cloud puffs promotes greater evaporative cooling within the STBL. This process, in which droplet sedimentation reduces cloud-top evaporation while concurrently permitting more evaporation at the sides of the downdrafts, ultimately drives turbulence generation. In the absence of sedimentation, cloud decoupling becomes more likely, as excessive evaporation during cloud-top entrainment events can destabilize the large-eddy circulation responsible for transporting moisture from the surface to the cloud layer. Our results show the importance of resolving both the cloud and subcloud layers at meter-scale resolution to properly understand the vertical distribution of moisture and the organization of turbulence.

Our findings show that microphysical effects—sedimentation in particular—hold equal importance to turbulent effects, and that meter-scale resolution is needed to correctly represent their influence on cloud-top entrainment. Extrapolating these findings to atmospheric conditions looks favorable, given the trend of multiple variables such as LWP and mean entrainment velocity towards Reynolds number similarity. Accounting for droplet sedimentation is a key component in understanding how stratocumulus clouds evolve over time, particularly in how changes in turbulence and moisture dynamics influence cloud amount. Advancing this understanding requires increased computational and observational efforts to improve droplet size distribution accuracy, particularly the distribution tail, due to the sedimentation flux's dependence on the fifth-order moment.

A.8 APPENDIX TO PAPER A

A.8.1 *Additional sensitivity experiments*

To estimate the sensitivity of the LWP and vertically integrated turbulence kinetic energy (E) to sedimentation strength, we considered the fields at 1.5 h in the reference case ($c_s = 2.7$ and Kolmogorov scale $\eta_0 = 1.4$ m) and continued two new cases with sedimentation strength $c_s = 0.0$ and $c_s = 5.4$. As seen in Figure A.10,

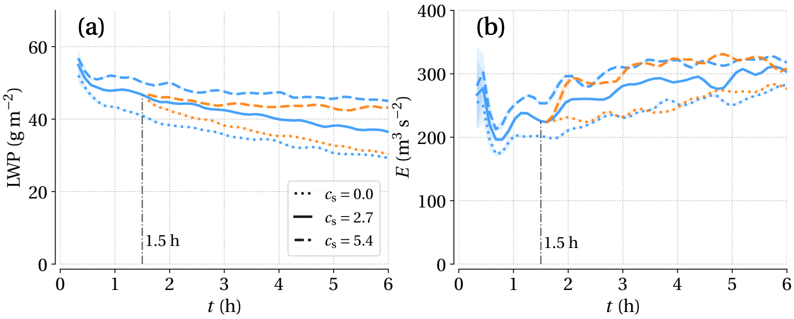

Figure A.10: Sensitivity of (a) liquid water path (LWP) and (b) vertically integrated turbulence kinetic energy (E) to changes in sedimentation strength. We consider two cases $c_s = 0.0$ and $c_s = 5.4$ mm s^{-1}/(kg m^{-3})$^{2/3}$ after 1.5 h, initialized with the simulation $\{\eta_0 = 1.4 \text{ m},\ c_s = 2.7 \text{ mm s}^{-1}/(\text{kg m}^{-3})^{2/3}\}$.

the time response of LWP to return to non-adjusted conditions is slower than that of E. This lag is attributed to the fixed moisture, or buoyancy, flux at the ocean surface. While E attempts to draw more moisture into the system, the total water flux, q_t, remains constrained. The E response occurs within less than an hour, while that of LWP takes until the remainder of the simulation. To ensure that the statistical properties are independent of the grid spacing once the Kolmogorov scales are sufficiently resolved, we examined the case $\{\eta_0 = 2.8 \text{ m},\ c_s = 2.7\}$ and halved the grid spacing from 4.4 m to 2.2 m. This new case corresponds to a grid size $3072^2 \times 768$, instead of $1536^2 \times 384$. Figure A.11 shows that the new paths of horizontally averaged and vertically integrated LWC (LWP) and TKE (E) align closely with those from larger grid spacing. This outcome justifies the distinguishing property of DNS that results should be grid-spacing independent when appropriate numerical schemes are implemented. We confirm that expanding the horizontal domain size by a factor of 4 does not noticeably alter variables like LWP and E. Figure A.11 compares two simulation runs at the Kolmogorov scale $\eta_0 = 2.8$ m, where one run has double the horizontal extent in both directions, requiring twice the number of grid points in each horizontal direction ($3072^2 \times 384$). We see smooth trajectories of LWP and E when the horizontal length L_x is sufficiently larger than the convective length scales, ensuring that the ratio between the two remains independent of L_x. This result supports our choice in the domain limits of our simulations, as increasing the domain size only marginally improves statistical convergence.

A.8.2 *Entrainment rate equation: deformation term*

The calculation of the mean entrainment velocity in Eq. 11 includes a deformation term (last term in Eq. 11) represented by a time derivative. As a first approximation of the mean entrainment velocity, we neglect this term. This simplification allows us to solve Eq. 10 for $z_i(t)$ and compare it to the actual evolution of z_i, which is determined directly from the change of the minimum turbulent flux of the liquid-water static energy (see Figure A.2c). Through this comparison, we investigate whether the deformation term becomes increasingly negligible over time, potentially lessening the dependence on expensive DNS simulations for determin-

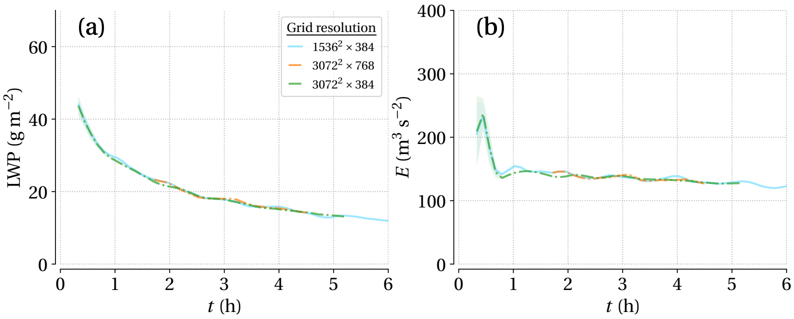

Figure A.11: Sensitivity of (a) liquid water path (LWP) and (b) vertically integrated turbulence kinetic energy (E) to changes in grid spacing and horizontal domain size, orange and green lines, respectively. We examine the case $\{\eta_0 = 2.8\ \mathrm{m},\ c_s = 2.7\}$ with twice the grid spacing ($3072^2 \times 768$) and twice the horizontal extent in both directions ($3072^2 \times 384$).

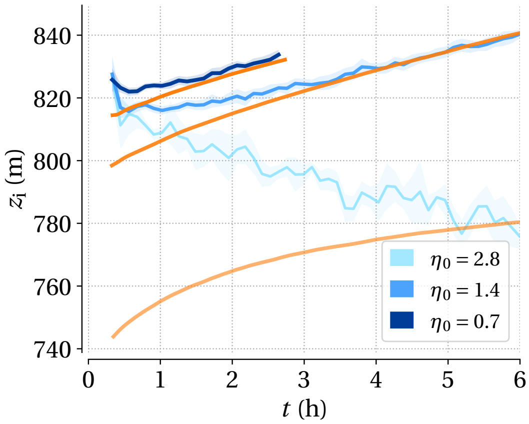

Figure A.12: Comparison of the temporal evolution of the inversion height, z_i, calculated using the entrainment rate equation without the deformation term (orange lines) and directly as the change in the minimum turbulent flux of liquid-water static energy, for three different Kolmogorov numbers (equivalent to different Reynolds numbers, see Table. 2).

ing the inversion height, z_i. Indeed, this simplification proves effective, as the difference between the two calculations decreases over time with increasing Reynolds numbers. We also test the sensitivity to varying Reynolds numbers, showing that the importance of the deformation term diminishes as the Reynolds number increases. For the Kolmogorov scales $\eta_0 = 0.7$ m and $\eta_0 = 1.4$ m, the results align particularly well.

DATA AVAILABILITY STATEMENT

Primary data and source code can be found at Pistor, 2025.

B

LINKING DROPLET SEDIMENTATION TO STRATOCUMULUS ADJUSTMENT MECHANISMS: A FINER LOOK

The work in this appendix is in preparation for publication as:

Pistor, R. & Mellado, J. P. Linking Droplet Sedimentation to Stratocumulus Adjustment Mechanisms: A Finer Look. *In preparation.*

Linking Droplet Sedimentation to Stratocumulus Adjustment Mechanisms: A Finer Look

Raphael Pistor[1] and Juan Pedro Mellado [2]

[1]International Max Planck Research School on Earth System Modelling, Max Planck Institute for Meteorology, Hamburg, Germany
[2]Meteorological Institute, University of Hamburg, Hamburg, Germany

ABSTRACT

We investigate how droplet sedimentation interacts with subtropical marine low-cloud adjustment mechanisms, using direct numerical simulations at Kolmogorov scales of 1.4 m. We conduct sensitivity experiments to isolate the effects of three mechanisms: (i) thermodynamic warming, (ii) reduced downwelling longwave radiation, and (iii) increased inversion strength. Responses are quantified as absolute and relative changes in mean entrainment velocity (w_e), liquid water path (LWP), vertically integrated turbulence kinetic energy (E), and inversion height (z_i). The simulations capture fine-scale structures, including the location of evaporative cooling events. Regardless of the environmental setup, stronger sedimentation consistently reduces w_e, increases LWP and E, and slightly lowers z_i. Sedimentation effects are comparable in magnitude to the adjustment mechanisms.

B.1 INTRODUCTION

The sensitivity of the climate system to perturbations in Earth's radiation balance–whether driven by anthropogenic sources or natural variability–remains at the forefront of climate research, given the potentially profound socio-economic impacts (Cooke et al., 2014; Rennert et al., 2022; Christensen et al., 2022). Particularly deserving of attention are low-latitude stratocumulus clouds, whose ubiquitous presence in the subtropical highs and strong albedo contribute to cooling the global-mean surface temperature (Klein and Hartmann, 1993; Wood, 2012). In a warming climate, the response of these clouds depends on adjustment mechanisms that either amplify (positive feedback) or mitigate (negative feedback) the initial radiative imbalance (Siebesma et al., 2020). For subtropical marine low-clouds, three dominant mechanisms have been identified: (a) a thermodynamic mechanism, wherein elevated sea surface temperatures (SST) enhance convective mixing and increase cloud-top entrainment of dry free-tropospheric air, thereby reducing cloud amount; (b) a radiative mechanism, wherein weaker longwave (LW) radiative cooling reduces vertical moisture transport, similarly resulting in less cloud; and (c) stability, where a stronger inversion promotes low-cloud formation. (Bretherton et al., 2013; Blossey et al., 2013; Bretherton and Blossey, 2014; Bretherton, 2015; Nuijens and Siebesma, 2019). Various lines of evidence, including observations and large-eddy simulations (LES), show the robustness of a positive feedback when these mechanisms are considered collectively (Qu et al., 2015; Schneider et al., 2019; Scott et al., 2020; Sherwood et al., 2020; Myers et al., 2021; Koshiro et al., 2022; Schiro et al., 2022; Forster et al., 2023). However, the extent to which these mechanisms are shaped by microphysical processes remains unclear. This question is particularly pressing for climate modelers, who must rely on high-resolution grids to represent the multiscale dynamics and sharp capping inversions characteristic of stratocumulus clouds. While a myriad of studies has examined microphysical effects and low-cloud adjustment mechanisms independently, their interplay remains unexplored and constitutes the focus of this study.

Interpreting the macrophysical behavior of clouds requires an understanding of their underlying microphysical processes. Among these, droplet sedimentation refers to the rate at which water droplets fall under gravity; larger droplets descend faster because their lower surface-area-to-weight ratios reduce air resistance. Previous studies have shown that stronger sedimentation strengths reduce the entrainment of dry, warm free-tropospheric air into the cloud layer, thereby extending cloud lifetime (Ackerman et al., 2004; Bretherton et al., 2007; Ackerman et al., 2009; Hill et al., 2009; Mellado, 2017; Lozar and Mellado, 2017; Schulz and Mellado, 2019; Williams and Igel, 2021; Chun et al., 2023; Pistor and Mellado, 2025). During this process, reduced evaporation at the cloud top leaves more liquid water available for evaporative cooling elsewhere (Stevens et al., 1998; Bretherton et al., 2007; Ackerman et al., 2009; Lozar and Mellado, 2017; Mellado et al., 2018; Chun et al., 2023), particularly at the boundaries between warm, dry downdrafts and cool, moist cloudy puffs. The resulting increased evaporative cooling accelerates the downdrafts and intensifies turbulence within the boundary layer and increases the overall moisture content in the cloud (liquid water) and subcloud (water vapor) layers (Pistor and Mellado, 2025). Given the impact of sedimentation on cloud-top entrainment, turbulence, and cloud fraction, further investigation is warranted—particularly regarding its interaction with the aforementioned adjustment mechanisms in the context of a changing climate. Indeed, changes in cloud properties induced by sedimentation can be of comparable magnitude to those driven by low-cloud adjustment mechanisms, suggesting potentially dampening or amplifying scenarios.

One recurring question in simulating low clouds is how to account for the uncertainty that stems from subgrid variability. Studies investigating low-cloud adjustment mechanisms often employ global climate models, cloud-resolving models, or LES, while sedimentation studies typically rely on LES. All of these approaches depend on turbulence parameterizations and, at best, achieve vertical resolutions of 5 m. In regions with sharp property gradients, subgrid diffusivity can introduce uncertainties of the order of one, affecting entrainment rates and cloud thickness in simulations (Stevens and Bretherton, 1999; Stevens, 2005; Cheng et al., 2010; Lozar and Mellado, 2017; Hoffmann and Feingold, 2019). The cloud-top temperature inversion is a prime example, where down-gradient mixing parameterizations of turbulence tend to lead to overestimated entrainment. These parameterizations can inadvertently transport liquid water upward, thereby counteracting droplet settling (Mellado et al., 2018). The resulting purely numerical dissipation causes cloud loss, mimicking the effects of a positive low-cloud feedback. Direct numerical simulations (DNS) offer a means to reduce these uncertainties by avoiding turbulence parameterizations altogether and adopting grid spacings fine enough to resolve small-scale turbulent processes. DNS studies confirm that meter-scale resolution is necessary to accurately represent turbulence at the cloud top and within the boundary layer (Mellado et al., 2018; Schulz and Mellado, 2019; Hoffmann et al., 2020; Pistor and Mellado, 2025). By leveraging DNS, we can quantify the effects of sedimentation with reduced diffusion-related bias and advance our process-level understanding of low-cloud adjustment mechanisms.

Our physically based, or 'reductionist,' approach (e.g., (Sherwood et al., 2020)) systematically tests dominant cloud-controlling factors under plausible boundary conditions. While the specific environmental changes examined here may not be the most relevant under future climate scenarios, this framework allows controlled evaluation of each mechanism. If a mechanism produces a large modeled impact but is unlikely to occur, its actual impact will be less than predicted. Put simply, the relative weight and proportion of different environmental perturbations in a future climate scenario remain speculative. Despite these uncertainties, our reductionist DNS framework provides a useful framework for interpreting cloud feedbacks as computational power and model resolution continue to improve.

In this study, we investigate how droplet sedimentation affects the response of stratocumulus clouds to adjustment mechanisms. By using DNS to explicitly resolve turbulent motions within the stratocumulus-topped boundary layer (STBL), we evaluate whether these high-resolution results produce results consistent with those of traditional LES, which rely on tuning. This study is motivated by recent findings from Pistor and Mellado, 2025, which indicate that sedimentation effects are on par with Reynolds number effects when grid spacings approach 1 m. To our knowledge, the sensitivity of low-cloud adjustments to sedimentation has not yet been systematically explored. Addressing this gap will improve our understanding in representing stratocumulus-cloud adjustments in climate models and projections.

B.2 SIMULATION SETUP

We investigate the effects of sedimentation and low-cloud adjustment mechanisms using a DNS approach. The set of governing equations used here and the formulation of the STBL is equivalent to Pistor and Mellado, 2025. The reference control case (CTL) matches the environmental conditions of the first research flight (RF01) of the DYCOMS-II observational campaign (Stevens, 2005). This case represents a non-precipitating, nocturnal marine stratocumulus layer in a warm subtropical region. Sedimentation is implemented in the model using a one-moment bulk microphysics scheme that assumes a log-normal droplet size distribution. The sedimentation flux, $\rho \mathbf{j}_{—}$, embeds the liquid-water specific humidity, q_l, as an independent variable, while the sedimentation strength is expressed by a single bulk sedimentation coefficient, c_s (units: m $s^{-1}/(\text{kg m}^{-3})^{2/3}$). The advantage of using a single coefficient is that it encompasses a range of parameter values, including the droplet number density and the geometric standard deviation ($\sigma_{gc} \equiv e^{\sigma}$), thereby streamlining the number of experiments and cutting down on computational costs. All simulations use a DYCOMS-II-based reference Kolmogorov scale of $\eta_0 = 1.4$ m, which corresponds to a reference Reynolds number $Re_0 = 5000$ and an isotropic grid spacing of approximately 2.2 m. Using 6,144 cores on the SuperMUC-NG at the Leibniz Supercomputing Centre, each simulation ran for $5-6$ simulated hours and required approximately 5!—!6 million core hours of computational time.

Low-cloud adjustment mechanisms are examined by comparing CTL to perturbed simulations representative of conditions expected in a warmer climate. Following the work of Blossey et al., 2013; Bretherton et al., 2013; Bretherton, 2015; Nuijens and Siebesma, 2019, the idealized climate change scenarios are simulated and categorized into three cases: P2, which involves a uniform 2 K increase sea-surface temperature (SST) along with moist-adiabatic warming of the entire air column above; P2FT, which applies an analogous warming to P2 but confines it to the free-troposphere (FT); and R10, which represents a 10% reduction in the radiative flux profile above the cloud layer due to increased concentrations of H_2O or CO_2. While both P2 and P2FT are associated to the thermodynamic adjustment mechanism, P2FT in reality acts as a stability mechanism; in contrast, R10 is related to the radiative adjustment mechanism. Each perturbed case is uniquely defined by different initial conditions, rather than by a set of imposed boundary conditions that evolve over time. As an example, in P2, the initial state sees a total water amount within the STBL increase from 9 to 10 g kg^{-1}, as expected due to Clausius-Clapeyron effects. P2 and P2FT show no change in relative humidity compared to CTL. The sensitivity experiments are outlined in Table 2.

B.3 RESULTS

B.3.1 *Validation*

Figure B.1 shows the temporal evolution of liquid water path (LWP), vertically integrated turbulence kinetic energy (E), and mean entrainment velocity (w_e) for all sedimentation strengths and environmental perturbations (P2, P2FT, R10). Each simulation is initialized with a fully saturated cloud deck and a measurement-based LWP of 60 g m^{-2}. After an initial spin-up phase, the LWP in Figure B.1a gradually decreases from this value due to coarse-resolution induced cloud-top mixing, even at the 2.2 m grid spacing used here. In a similar study, Pistor and Mellado, 2025 showed that meter-scale resolution ($Re_0 = 12500$) is necessary to achieve a quasi-steady state of LWP. Comparing to the LES ensemble from Stevens, 2005 (highlighted in gray in Figure B.1a), our CTL predicts LWP values slightly closer to measurement-based estimates. This gives us confidence that our moderate-Reynolds-number DNS simulations provide a trustworthy baseline for our analysis, as they reproduce the LES results without the uncertainties affiliated to tuning the models.

The temporal evolution of E (Figure B.1b) shows a spin-up phase followed by a gradual increase. This growth pattern likely reflects the transition from an ini-

Table 2: Table of experiments: Dependence of cloud properties on low-cloud adjustment mechanisms and sedimentation strength c_s.

Case	c_s $(\mathrm{m\ s^{-1}/(kg\ m^{-3})^{2/3}})$	w_e $(\mathrm{mm\ s^{-1}})$	LWP $(\mathrm{g\ m^{-2}})$	E $(\mathrm{m^3\ s^{-2}})$	z_i (m)	Δh $(\mathrm{kJ\ kg^{-1}})$
CTL	0	5.4	34.9	239	836	6.3
	2.7	5.1	42.4	267	816	6.9
	5.4	4.5	47.4	303	808	7.1
P2	0	5.0	29.9	231	825	6.4
	2.7	4.8	36.5	256	809	6.8
	5.4	4.3	41.3	267	804	7.2
P2FT	0	4.5	42.9	261	818	8.2
	2.7	4.2	48.9	281	796	8.7
	5.4	3.7	52.5	287	790	9.1
R10	0	4.8	29.0	176	817	6.4
	2.7	4.5	36.0	204	804	6.8
	5.4	4.6	47.4	278	805	7.2

For all simulations, the DYCOMS-II-based reference Kolmogorov scale $\eta_0 = 1.4$ m, with a corresponding reference Reynolds number $Re_0 = 5000$ and grid spacing $\Delta x = 2.2$ m. c_s is the sedimentation strength coefficient; a value of 2.7 $\mathrm{m\ s^{-1}/(kg\ m^{-3})^{2/3}}$ is representative of RF01 conditions from DYCOMS-II. The inversion height z_i is defined as the minimum turbulent flux of liquid-water static energy. The mean entrainment velocity (w_e), liquid water path (LWP), vertically integrated turbulence kinetic energy (E), inversion height (z_i), and jump in liquid-water static energy (Δh) are temporally averaged from the first hour onward. The grid dimensions (BxH) are $3072^2 \times 768$.

tially unorganized, chaotic flow field to one characterized by coherent large-scale updrafts and downdrafts. For this reason, turbulence levels are expected to level off and approach a near-constant value if the simulations were extended further. For the mean entrainment velocity (Figure B.1c), which is defined following Lilly, 1968 as

$$w_e = \frac{dz_i}{dt} - \langle w \rangle_{z_i} , \tag{13}$$

where z_i denotes the inversion height, defined by the minimum turbulent flux of liquid-water static energy, and $\langle w \rangle$ is the horizontally-averaged large-scale subsidence velocity, expressed as $-Dz$ with $D = 3.75 \times 10^{-6}\ \mathrm{s^{-1}}$. The simulations of w_e generally approach a quasi-steady state, and tend to exceed the measurement-based estimate of 4.4 mm $\mathrm{s^{-1}}$. The effect of sedimentation is captured at the moderate Reynolds number used in this study ($Re_0 = 5000$). While the magnitude of this effect is already substantial, previous studies have shown that it increases even more for higher Reynolds numbers (Pistor and Mellado, 2025).

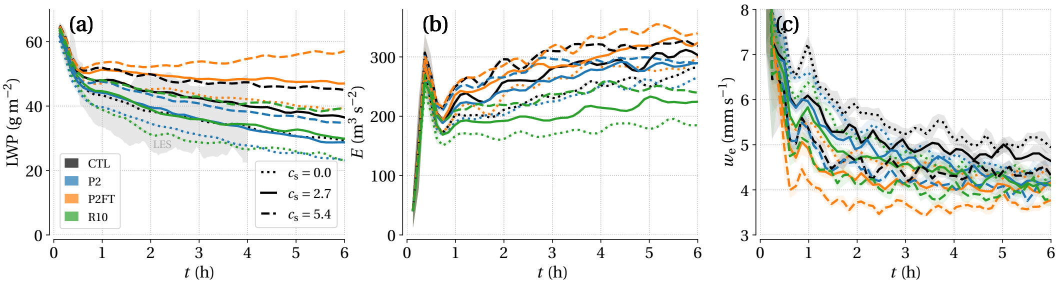

Figure B.1: Temporal evolution of (a) liquid water path, LWP, (b) vertically integrated turbulence kinetic energy, E, and (c) mean entrainment velocity, w_e, defined as the rate of change in inversion height based on the minimum turbulent flux of mean liquid-water static energy, $\langle h \rangle$. Results are shown for the CTL, P2, P2FT and R10 cases under two sedimentation strengths (see Table. 2). The gray region corresponds to the LES ensemble in Stevens, 2005, while the dashed black line indicates measurement-based estimates. For all cases, a running average over a 10 min window is applied, with the standard deviation indicated by the respective shaded colored region. The legend units for c_s: mm s^{-1}/(kg m^{-3})$^{2/3}$.

To facilitate comparisons among LWP, E, and w_e, we compute time-averaged values from the first hour of the simulation onward. We also include inversion height (z_i) as an additional variable. Figure B.2 shows that, regardless of the environmental setup (CTL, P2, P2FT, R10), increasing sedimentation strength leads to a reduction in w_e, an increase in LWP and E, and a lowering of the time-averaged inversion height. These qualitative changes are consistent with findings from Pistor and Mellado, 2025. The largest changes are observed in w_e, LWP, and E, while those in z_i are comparatively smaller.

Before analyzing the adjustment mechanisms, we switch from an absolute value overview to a relative change perspective. Figure B.3 presents the percentage changes induced by both sedimentation and the environmental perturbations. Sedimentation-induced changes (shown as symbols) are calculated as the difference between simulations with and without sedimentation for each environmental case. Effects of changing the environment are calculated by comparing each perturbed case to CTL, with results shown separately for simulations with and without sedimentation (represented by lined and dotted bars, respectively). Note that for any given variable, the difference between the CTL symbol (black circle) and any other symbol corresponds to the sensitivity of the adjustment mechanisms for that variable (i.e., the difference between the dotted and lined bars). At first glance, sedimentation effects are considerable, with magnitudes similar to those of the low-cloud adjustment mechanisms in this study. For this reason, compensatory effects between these two are possible. For example, comparing the LWP of CTL and P2 shows that P2 with sedimentation is approximately equal to CTL without sedimentation. Thus, neglecting microphysical processes such as droplet sedimentation could skew the assessment of whether the net cloud response manifests as thinning or thickening, and should be accounted for when evaluating the sign and magnitude of low-cloud feedbacks.

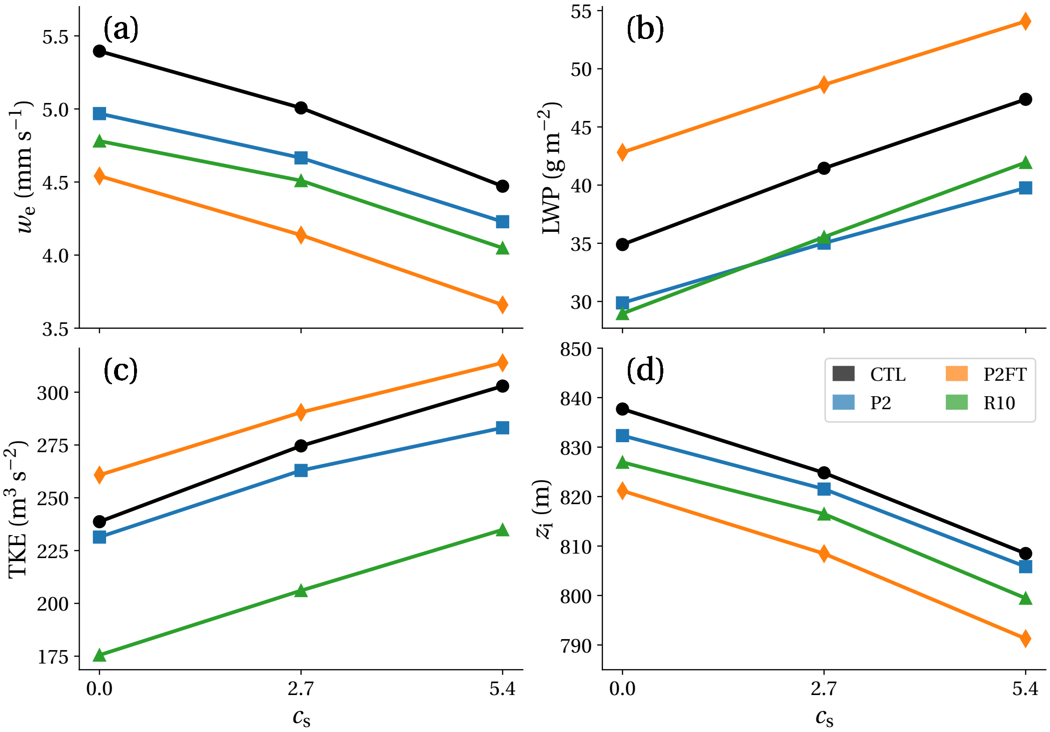

Figure B.2: Time-averaged values from the first hour onward of (a) mean entrainment velocity, w_e, (b) liquid water path, LWP, (c) vertically integrated turbulence kinetic energy, E, and (d) inversion height, z_i, for the CTL, P2, P2FT and R10 cases with varying sedimentation strengths (c_s; see Table. 2). The percentage values to the right of each line indicate the change attributable to sedimentation.

B.3.2 *Physical Mechanisms*

In what follows, we outline and interpret the physical processes of the three adjustment mechanisms in this study (P2, P2FT, R10). We then describe the sensitivity of these adjustments to sedimentation, followed by an analysis of their magnitudes.

The thermodynamic adjustment mechanism (P2) is implemented by uniformly heating the full vertical column by 2 K. The corresponding increase in total water specific humidity, as expected from Clausius-Claperyon effects, is prescribed directly by the initial conditions to ensure constant relative humidity throughout the column. The absolute humidity increases more within the STBL than in the FT, so that the moisture gradient is greater between the cloud top and overlying air when compared to CTL. At the same time, the inversion strength remains unchanged, meaning that vertical mixing is not suppressed. This combination of a larger moisture gradient and an unchanged inversion strength increases cloud-top evaporation (entrainment drying), and significantly reduces LWP (see also the vertical profile of liquid water content in Figure B.4a). The radiative heating rate (Figure B.4b) decreases proportionally to the reduced liquid water, suggesting that the cloud remains optically thick.

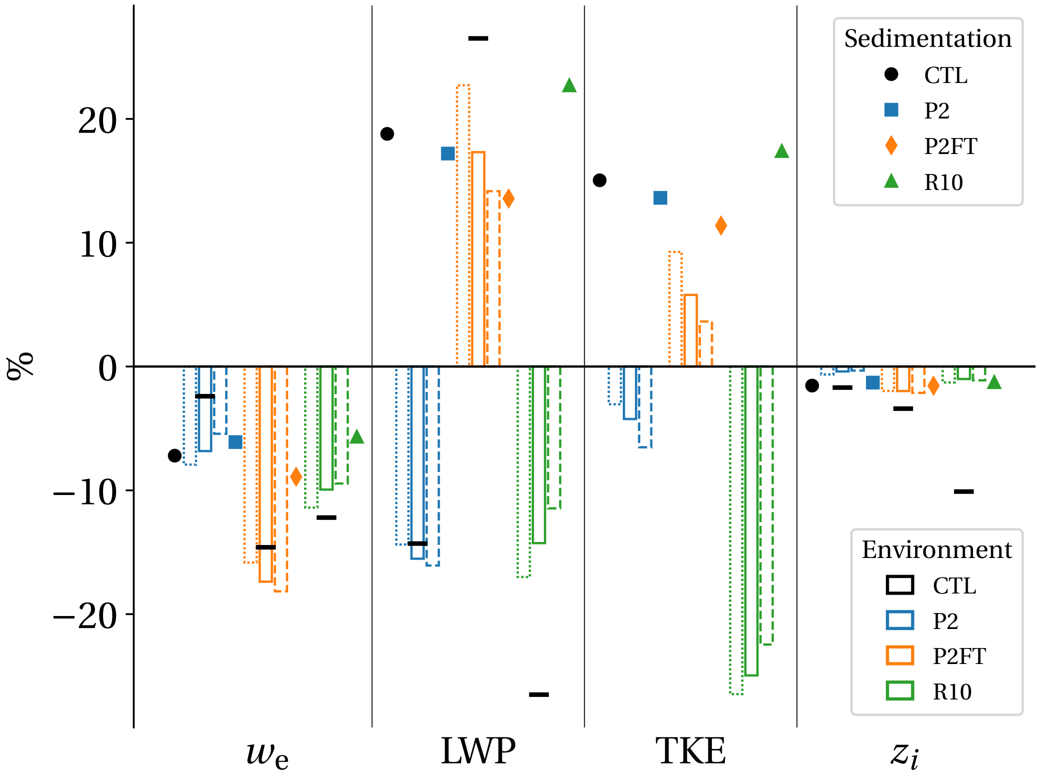

Figure B.3: Relative changes in the time-averaged values of (a) mean entrainment velocity, w_e, (b) liquid water path, LWP, (c) vertically integrated turbulence kinetic energy, E, and (d) inversion height, z_i, for the CTL, P2, P2FT and R10 cases with varying sedimentation strengths (c_s; see Table. 2). The bar plots show changes in the perturbed environments (P2, P2FT, R10) relative to CTL. Dotted bars indicate cases without sedimentation, while lined bars indicate cases with sedimentation. Symbols denote percentage changes due to varying c_s within each environment (as shown in Figure B.2). The black lines show the relative change of the multi-day mean for w_e, LWP, and z_i with sedimentation from LES simulations using the SAM model in Bretherton et al., 2013. Note, the comparison for P2FT is not exact, as their LES study also includes a 10% reduction in subsidence (P2SFT).

The altered thermodynamic structure of P2 also affect the entrainment dynamics. How, then, does the mean entrainment velocity (w_e in Figure B.3) and the turbulent entrainment of dry, warm air (not shown) decrease in P2 despite increased cloud-top evaporation? While the larger moisture gradient at the cloud top increases evaporation and the cooling of air parcels, this cooling is localized uniformly across the whole cloud-top area. The negatively buoyant air parcels that are produced on small-scales tend to slightly counteract the larger updrafts responsible for the growth of the boundary layer. Therefore, a larger moisture gradient between the STBL and FT can suppress entrainment by diffusing the stronger vertical motions that typically promote mixing at the cloud top. Evidence for this comes from the observation that cloud-layer turbulence levels decrease (Figure B.4c) and that downdrafts weaken in P2 (as deduced from the skewness of vertical velocity in Figure B.4d). Near the surface, turbulence levels increase

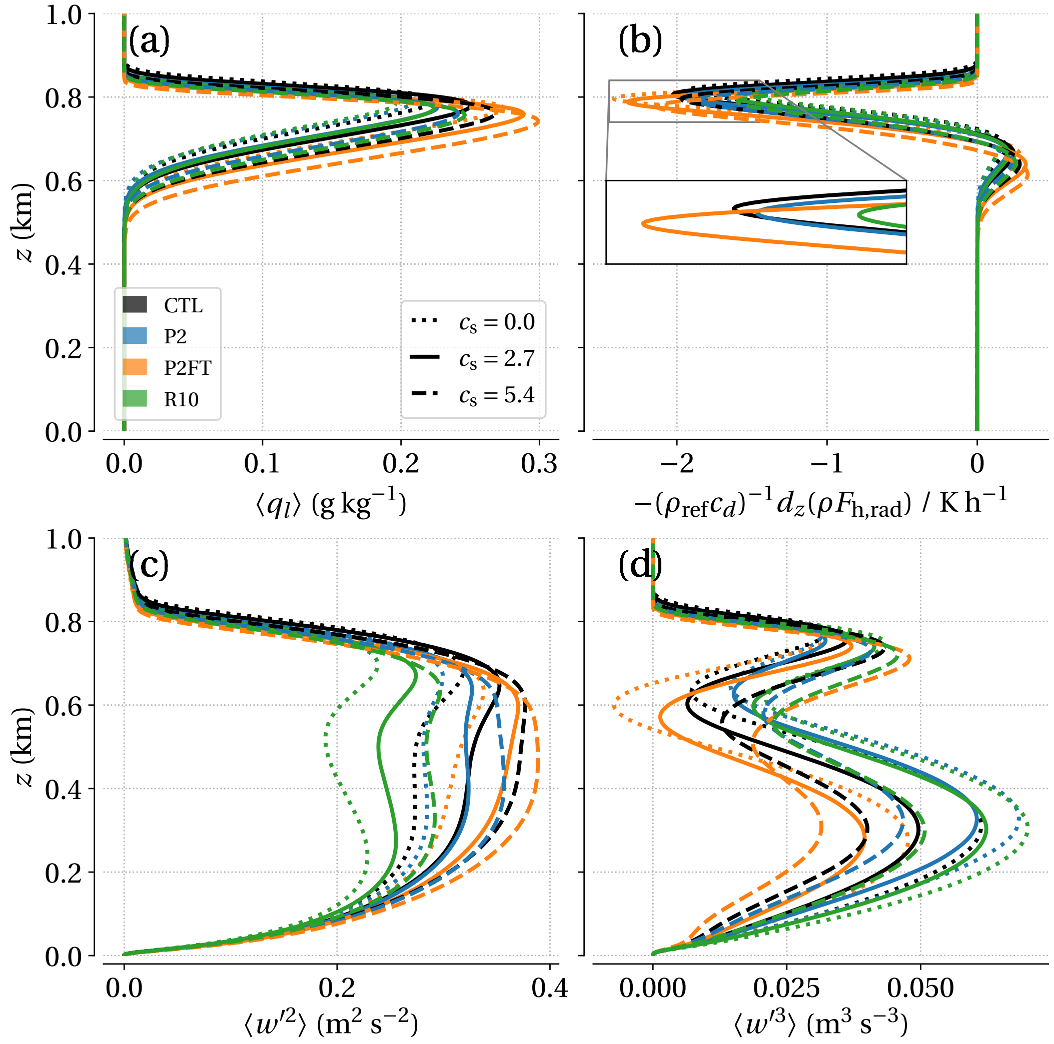

Figure B.4: Vertical profile of (a) liquid water content, (b) radiative heating rate, (c) the variance w'^2, and (d) the skewness w'^3, time-averaged from the first hour onward. The legend units for c_s: mm $s^{-1}/(kg\ m^{-3})^{2/3}$.

(Figure B.4c), which can be interpreted as the activation of thermals and a minor shift in STBL dynamics from cloud-top-driven turbulence to one where surface convection plays a larger role. Overall, the net turbulence (E) decreases mildly compared to CTL.

For the stability adjustment mechanism (P2FT), the role of a strengthened temperature inversion is tested by warming only the FT by 2 K. It bears mentioning that comparisons to previous studies are not exact, as LES experiments typically included a 10% reduction in subsidence (referred to as P2SFT), which is not applied here. Warming the FT air creates a more stable lid that suppresses vertical mixing across the inversion, as reflected by the increased molecular flux of ⟨h⟩ (not shown). This stronger stability enhances moisture transport cycle within the STBL. As LWP accumulates, LW radiative cooling becomes more effective at generating turbulence (see Figure B.4c). The less positive skewness of vertical velocity further indicates the presence of stronger, narrower downdrafts (Figure B.4d). High-resolution DNS modeling is critical here because the precise location of evaporative cooling matters for cloud dynamics. Unlike P2, where the largest change in the moisture gradient spans the entire inversion, in this case the most evaporative cooling occurs at the gradient between moist cloudy regions and downdrafts containing dry FT air— accelerating those downdrafts and increases turbulence. Finally, although both E and the turbulent entrainment of dry FT air into the cloud layer increase, the strengthened inversion still slows w_e, thereby limiting boundary-layer growth. Overall, the P2FT response resembles that produced by increasing the sedimentation strength, with both showing a reduction in w_e alongside increases in turbulence and LWP.

The radiative adjustment mechanism (R10) examines a more emissive FT, caused by elevated $\mathrm{CO_2}$ or $\mathrm{H_2O}$ concentrations, by imposing a $10\ \mathrm{W\ m^{-2}}$ reduction in the radiative flux above the cloud layer. This perturbation primarily affects cloud-top processes, while secondary effects propagate through the cloud and subcloud layers. First, the reduction in cloud-top LW radiative cooling decreases the generation of buoyancy-driven turbulence, as indicated by the E bar plots in Figure B.3 and vertical velocity variance in Figure B.4c. This turbulence reduction is substantial compared to the other adjustment mechanisms, exceeding -20%, with indications of cloud decoupling from negative values in the buoyancy flux profile (not shown). Second, despite the unchanged inversion strength, less turbulent plumes cause a slight decrease in the turbulent entrainment of warm, dry air, which reduces evaporative cooling and thus causes turbulence to lessen further. This is reflected in the weakening of downdrafts caused by fewer convective instabilities forming at the cloud top, as indicated by the increased skewness of vertical velocity (Figure B.4d). Lastly, with less turbulent mixing to drive the cloud layer upward, w_e is reduced. The time-averaged inversion height is only marginally affected. The upward transport of water vapor is also limited, culminating in reduced LWP and cloud thinning. Although R10 yields LWP reductions similar to P2, it shows a much larger decrease in E and in cloud-top radiative cooling (Figure B.4b), stressing the nonlinear influence of initial environmental conditions on cloud dynamics. Although well established, these small-scale processes require DNS modeling to confirm their qualitative behavior and quantify their impacts without the uncertainties of model tuning.

B.3.3 *Sensitivity Analysis and Comparison with Prior Studies*

The sensitivity of low-cloud adjustment mechanisms to sedimentation is particularly discernible in Figure B.3, indicated by differences between the dotted and lined bars. This sensitivity reveals whether the effects of these mechanisms are dampened, amplified, or even reversed. On first impression, P2FT shows the largest sensitivity to sedimentation, with clear dampening of LWP and E when sedimentation strength increases. However, LWP (and to some extent E) may not serve as the most reliable sensitivity metric, since the cloud saturates at approximately $60\ \mathrm{g\ m^{-2}}$. Once near this saturation threshold, additional increases in LWP are less impactful than in cases with a lower initial LWP. Given this limitation, w_e serves as a more physically meaningful metric, as its time-dependent variability better reflects changes in STBL dynamics that saturated, bulk-integrated measures like LWP may obscure. We find that the reduction in w_e for P2FT is intensified with sedimentation, while it softens for P2 and R10. Taken together, the sensitivity of low-cloud adjustment mechanisms to sedimentation is generally modest, with no indication of sign reversal. Nevertheless, for higher sedimentation strengths, the magnitude of the response can still change substantially; in P2, it could even be full offset. As discussed further below, the strength of this effect also depends on the Reynolds number.

Figure B.3 also includes a comparison to LES results from Bretherton et al., 2013, showing the magnitudes of relative changes for w_e, LWP, and z_i, indicated by the black horizontal lines. The comparison is made for simulations that include sedimentation, consistent with the log-normal droplet size distribution setup used in Bretherton et al., 2013; Ackerman et al., 2009. There is full agreement in the sign of the relative changes, and in most cases, the magnitudes are approximate. All three adjustment mechanisms produce a relative change in LWP of approximately 15% when sedimentation is included (positive for P2FT; negative for P2 and R10). The most notable difference is that our simulations predict smaller changes in LWP and z_i for R10, with magnitudes more closely resembling those of P2. One possible explanation is that the turbulence reduction reported by Bretherton et al., 2013 may have been overly strong, potentially due to insufficient resolution of eddies smaller than 5 m. This could have caused excessive decay of turbulent motions, resulting in an overestimated reduction in LWP in R10. The LWP in P2FT from Bretherton et al., 2013 is also considerably larger than in our simulations, though this is likely due to the 10% reduction in subsidence used in that study; without this reduction, the cloud top would not rise as much, and LWP would likely be lower.

A more relevant discrepancy appears in P2 for w_e, where our simulations show a reduction more than twice that reported by Bretherton et al., 2013. Such differences may stem from variations in environmental conditions. In our CTL case, the background conditions are fitted to RF01 observations from the DYCOMS-II field campaign ((Stevens, 2005)) and are broadly consistent with those used in Bretherton et al., 2013, which represent prototype well-mixed stratocumulus clouds under typical summer conditions in the northeast Pacific Ocean near California. In both studies, major deviations from CTL should occur only in the adjustment mechanism experiments (thermodynamic, stability, and radiation) or from microphysical changes such as sedimentation strength. Beyond these large-scale conditions, cloud behavior is also sensitive to the Reynolds number, Re, and thus to model resolution; for fixed reference length and velocity scales, the Reynolds number is inversely proportional to the molecular viscosity. Increasing Re substantially raises LWP in simulations, with convergence toward measurement-based values typically reached at grid spacings of 1 m or finer. At such scales, sedimentation effects become comparable in magnitude to Reynolds number effects (Pistor and Mellado, 2025), and importantly, the sedimentation-induced reduction in w_e increases, reaching up to 20% at $\mathrm{Re}_0 = 12500$. It is reasonable to expect that the w_e reductions in Figure B.3 would be further amplified at higher Re, implying that both sedimentation effects and adjustment mechanisms exert an even stronger force on STBL dynamics under more realistic turbulent conditions.

B.4 CONCLUSIONS

This study explores how droplet sedimentation modulates adjustment mechanisms in stratocumulus clouds. For the first time, sedimentation and adjustment-mechanism effects are combined using direct numerical simulations (DNS) at a moderate Reynolds number ($\mathrm{Re}_0 = 5000$, corresponding to a Kolmogorov scale of $\eta_0 = 1.4$ m). Our control case (CTL) and sedimentation parameters are based on observations from the first research flight of the DYCOMS-II field campaign. Perturbations represent climate-change-relevant adjustments in column temperature (P2), inversion strength (P2FT), and incoming longwave radiation (R10). We analyze temporal averages of liquid water path (LWP), vertically integrated turbulent kinetic energy (E), mean entrainment velocity (w_e), and inversion height (z_i) to quantify absolute and relative changes across cases, including their sensitivity to sedimentation.

Our DNS reproduces the sign and, in most cases, the magnitude of low-cloud adjustment responses reported in LES studies such as Bretherton et al., 2013. DNS becomes computationally feasible, while omitting the uncertainties of tuned turbulence parameterizations. Summing the contributions from the adjustment mechanisms yields a net reduction in cloudiness, indicating a positive feedback. Correspondingly, w_e, E, and z_i all show negative relative changes, regardless of whether sedimentation is included. By resolving fine spatial structures, DNS provides new mechanistic insight; for example, the scale and location of evaporative cooling, whether broadly distributed across the inversion or localized in sharp gradients, affects the magnitude of the adjustment mechanisms.

Across all environmental setups (CTL, P2, P2FT, and R10), increasing sedimentation strength consistently reduces w_e, increases LWP and E, and slightly lowers z_i. The magnitude of sedimentation effects is comparable to that of the thermodynamic, stability, and radiative adjustment mechanisms, suggesting potential compensation or amplification between them. For w_e, adjustment mechanisms are moderately sensitive to sedimentation, but this sensitivity increases with sedimentation strength; for example, strong sedimentation could neutralize the reduction in w_e induced by a 2 K SST warming (P2). Given that these results depend on the Reynolds number Re, further increases in Re are expected to amplify the reductions in w_e and the associated changes in LWP.

DATA AND TOOLS

I gratefully acknowledge the Gauss Centre for Supercomputing e.V. for providing computing time on the GCS Supercomputer SuperMUC-NG at the Leibniz Supercomputing Centre, and the German Climate Computing Center DKRZ for access on the Levante supercomputer.

I want to give credit to Juan Pedro Mellado for developing the numerical model TLab (Mellado, 2025) used for the direct numerical simulations in this dissertation.

Figure. 2.3 was assembled by Denise Müller-Dum, while the individual plots were created by myself.

I used ChatGPT (OpenAI, 2023) for grammar correction and suggestions on sentence reformulation and style. ChatGPT was not involved in the scientific research presented in this dissertation.

This dissertation was typeset using the `classicthesis` template developed by Ivo Pletikosić and André Miede (`https://bitbucket.org/amiede/classicthesis/`).

BIBLIOGRAPHY

Ackerman, A. S. et al. (2000). "Effects of aerosols on cloud albedo: Evaluation of Twomey's parameterization of cloud susceptibility using measurements of ship tracks." In: *Journal of the Atmospheric Sciences* 57.16, pp. 2684–2695.

Ackerman, A. S. et al. (2004). "The impact of humidity above stratiform clouds on indirect aerosol climate forcing." In: *Nature* 432.7020, pp. 1014–1017.

Ackerman, A. S. et al. (2009). "Large-eddy simulations of a drizzling, stratocumulus-topped marine boundary layer." In: *Monthly Weather Review* 137.3, pp. 1083–1110.

Albrecht, B. A. (1989). "Aerosols, cloud microphysics, and fractional cloudiness." In: *Science* 245.4923, pp. 1227–1230.

Albrecht, B. A., R. S. Penc, and W. H. Schubert (1985). "An observational study of cloud-topped mixed layers." In: *Journal of Atmospheric Sciences* 42.8, pp. 800–822.

Arrhenius, S. (1908). *Worlds in the making: the evolution of the universe*. Harper.

Bilal, A. and D. R. Känzig (2024). *The macroeconomic impact of climate change: Global vs. local temperature*. Tech. rep. National Bureau of Economic Research.

Blossey, P. N. et al. (2013). "Marine low cloud sensitivity to an idealized climate change: The CGILS LES intercomparison." In: *Journal of Advances in Modeling Earth Systems* 5.2, pp. 234–258.

Bony, S. and J.-L. Dufresne (2005). "Marine boundary layer clouds at the heart of tropical cloud feedback uncertainties in climate models." In: *Geophysical Research Letters* 32.20.

Bony, S. et al. (2004). "On dynamic and thermodynamic components of cloud changes." In: *Climate dynamics* 22.2, pp. 71–86.

Bretherton, C. S. (2015). "Insights into low-latitude cloud feedbacks from high-resolution models." In: *Philosophical Transactions of the Royal Society A: Mathematical, Physical and Engineering Sciences* 373.2054, p. 20140415.

Bretherton, C. S. and P. N. Blossey (2014). "Low cloud reduction in a greenhouse-warmed climate: Results from Lagrangian LES of a subtropical marine cloudiness transition." In: *Journal of Advances in Modeling Earth Systems* 6.1, pp. 91–114.

Bretherton, C. S., P. N. Blossey, and C. R. Jones (2013). "Mechanisms of marine low cloud sensitivity to idealized climate perturbations: A single-LES exploration extending the CGILS cases." In: *Journal of Advances in Modeling Earth Systems* 5.2, pp. 316–337.

Bretherton, C. S., P. N. Blossey, and J. Uchida (2007). "Cloud droplet sedimentation, entrainment efficiency, and subtropical stratocumulus albedo." In: *Geophysical research letters* 34.3.

Bretherton, C. S. and M. C. Wyant (1997). "Moisture transport, lower-tropospheric stability, and decoupling of cloud-topped boundary layers." In: *Journal of the atmospheric sciences* 54.1, pp. 148–167.

Bretherton, C. S. et al. (1999). "An intercomparison of radiatively driven entrainment and turbulence in a smoke cloud, as simulated by different numerical models." In: *Quarterly Journal of the Royal Meteorological Society* 125.554, pp. 391–423.

Bretherton, C. (1997). "Convection in stratocumulus-topped atmospheric boundary layers." In: *The physics and parameterization of moist atmospheric convection*, pp. 127–142.

Bronsther, J. and Y. Xu (2025). "The social costs of solar radiation management." In: *npj Climate Action* 4.1, p. 69.

Caldwell, P. and C. S. Bretherton (2009). "Response of a subtropical stratocumulus-capped mixed layer to climate and aerosol changes." In: *Journal of Climate* 22.1, pp. 20–38.

Ceppi, P. et al. (2017). "Cloud feedback mechanisms and their representation in global climate models." In: *Wiley Interdisciplinary Reviews: Climate Change* 8.4, e465.

Cheng, A., K.-M. Xu, and B. Stevens (2010). "Effects of resolution on the simulation of boundary-layer clouds and the partition of kinetic energy to subgrid scales." In: *Journal of Advances in Modeling Earth Systems* 2.1.

Christensen, M. W., W. K. Jones, and P. Stier (2020). "Aerosols enhance cloud lifetime and brightness along the stratus-to-cumulus transition." In: *Proceedings of the National Academy of Sciences* 117.30, pp. 17591–17598.

Christensen, M. W. and G. L. Stephens (2011). "Microphysical and macrophysical responses of marine stratocumulus polluted by underlying ships: Evidence of cloud deepening." In: *Journal of Geophysical Research: Atmospheres* 116.D3.

Christensen, M. W. et al. (2022). "Opportunistic experiments to constrain aerosol effective radiative forcing." In: *Atmospheric chemistry and physics* 22.1, pp. 641–674.

Chun, J.-Y. et al. (2023). "Microphysical, macrophysical, and radiative responses of subtropical marine clouds to aerosol injections." In: *Atmospheric Chemistry and Physics* 23.2, pp. 1345–1368.

Coakley Jr, J. A. and C. D. Walsh (2002). "Limits to the aerosol indirect radiative effect derived from observations of ship tracks." In: *Journal of the Atmospheric Sciences* 59.3, pp. 668–680.

Cooke, R. et al. (2014). "Value of information for climate observing systems." In: *Environment Systems and Decisions* 34, pp. 98–109.

De Roode, S. R. et al. (2016). "Large-eddy simulations of EUCLIPSE–GASS Lagrangian stratocumulus-to-cumulus transitions: Mean state, turbulence, and decoupling." In: *Journal of the Atmospheric Sciences* 73.6, pp. 2485–2508.

Deardorff, J. W. (1972). "Parameterization of the planetary boundary layer for use in general circulation models." In: *Monthly Weather Review* 100.2, pp. 93–106.

— (1980). "Stratocumulus-capped mixed layers derived from a three-dimensional model." In: *Boundary-layer meteorology* 18.4, pp. 495–527.

Deardorff, J. W. et al. (1970). "Convective velocity and temperature scales for the unstable planetary boundary layer and for Rayleigh convection." In: *J. atmos. Sci* 27.8, pp. 1211–1213.

Diamond, M. S. et al. (2020). "Substantial cloud brightening from shipping in subtropical low clouds." In: *AGU Advances* 1.1, e2019AV000111.

Diamond, M. S. et al. (2022). "Physical Science Checkpoints and Exit Ramps for Marine Cloud Brightening Research." In: *American Meteorological Society Meeting Abstracts*. Vol. 102, J4–1.

Dussen, J. Van der, S. De Roode, and A. Siebesma (2016). "How large-scale subsidence affects stratocumulus transitions." In: *Atmospheric Chemistry and Physics* 16.2, pp. 691–701.

Erfani, E. et al. (2022). "Simulating aerosol lifecycle impacts on the subtropical stratocumulus-to-cumulus transition using large-eddy simulations." In: *Journal of Geophysical Research: Atmospheres* 127.21, e2022JD037258.

Faloona, I. et al. (2005). "Observations of entrainment in eastern Pacific marine stratocumulus using three conserved scalars." In: *Journal of the atmospheric sciences* 62.9, pp. 3268–3285.

Fedorovich, E., R. Conzemius, and D. Mironov (2004). "Convective entrainment into a linearly stratified atmosphere: Bulk models reevaluated through large eddy simulations." In: *Journal of the atmospheric sciences* 61.3, pp. 281–295.

Feingold, G. et al. (2010). "Precipitation-generated oscillations in open cellular cloud fields." In: *Nature* 466.7308, pp. 849–852.

Feingold, G. et al. (2024). "Physical science research needed to evaluate the viability and risks of marine cloud brightening." In: *Science advances* 10.12, eadi8594.

Fodor, K., J. P. Mellado, and A. Haghshenas (2022). "On the Non-monotonic Variation of the Entrainment Buoyancy Flux with Wind Shear." In: *Boundary-Layer Meteorology* 184.3, pp. 463–477.

Forster, P. et al. (2023). *The Earth's Energy Budget, Climate Feedbacks and Climate Sensitivity*. Ed. by V. Masson-Delmotte et al. Cambridge University Press, 923–1054. DOI: `10.1017/9781009157896.009`.

Gerber, H et al. (2005). "Holes and entrainment in stratocumulus." In: *Journal of the atmospheric sciences* 62.2, pp. 443–459.

Glassmeier, F. et al. (2021). "Aerosol-cloud-climate cooling overestimated by ship-track data." In: *Science* 371.6528, pp. 485–489.

Grabowski, W. W. and G. C. Abade (2017). "Broadening of cloud droplet spectra through eddy hopping: Turbulent adiabatic parcel simulations." In: *Journal of the Atmospheric Sciences* 74.5, pp. 1485–1493.

Gristey, J. J. and G. Feingold (2025). "Stratospheric aerosol injection would change cloud brightness." In: *Geophysical Research Letters* 52.6, e2024GL113914.

Gryspeerdt, E. et al. (2019). "Constraining the aerosol influence on cloud liquid water path." In: *Atmospheric Chemistry and Physics* 19.8, pp. 5331–5347.

Haghshenas, A. and J. P. Mellado (2019). "Characterization of wind-shear effects on entrainment in a convective boundary layer." In: *Journal of Fluid Mechanics* 858, pp. 145–183.

Hartmann, D. L., M. E. Ockert-Bell, and M. L. Michelsen (1992). "The effect of cloud type on Earth's energy balance: Global analysis." In: *Journal of Climate*, pp. 1281–1304.

Hartmann, D. L. and D. A. Short (1980). "On the use of earth radiation budget statistics for studies of clouds and climate." In: *Journal of Atmospheric Sciences* 37.6, pp. 1233–1250.

Haywood, J. M. et al. (2023). "Climate intervention using marine cloud brightening (MCB) compared with stratospheric aerosol injection (SAI) in the UKESM1 climate model." In: *Atmospheric Chemistry and Physics* 23.24, pp. 15305–15324.

Heinze, R. et al. (2017). "Large-eddy simulations over Germany using ICON: A comprehensive evaluation." In: *Quarterly Journal of the Royal Meteorological Society* 143.702, pp. 69–100.

Held, I. M. and B. J. Soden (2006). "Robust responses of the hydrological cycle to global warming." In: *Journal of climate* 19.21, pp. 5686–5699.

Hill, A. A., G. Feingold, and H. Jiang (2009). "The influence of entrainment and mixing assumption on aerosol–cloud interactions in marine stratocumulus." In: *Journal of the Atmospheric Sciences* 66.5, pp. 1450–1464.

Hoffmann, F., Y.-S. Chen, and G. Feingold (2024). "On the Processes Determining the Slope of Cloud-Water Adjustments in Non-Precipitating Stratocumulus." In: *EGUsphere* 2024, pp. 1–21.

Hoffmann, F. and G. Feingold (2019). "Entrainment and mixing in stratocumulus: Effects of a new explicit subgrid-scale scheme for large-eddy simulations with particle-based microphysics." In: *Journal of the Atmospheric Sciences* 76.7, pp. 1955–1973.

Hoffmann, F. et al. (2020). "Liquid water path steady states in stratocumulus: Insights from process-level emulation and mixed-layer theory." In: *Journal of the Atmospheric Sciences* 77.6, pp. 2203–2215.

Hogan, R. J. et al. (2009). "Vertical velocity variance and skewness in clear and cloud-topped boundary layers as revealed by Doppler lidar." In: *Quarterly Journal of the Royal Meteorological Society: A journal of the atmospheric sciences, applied meteorology and physical oceanography* 135.640, pp. 635–643.

Igel, A. L. (2024). "Processes controlling the entrainment and liquid water response to aerosol perturbations in nonprecipitating stratocumulus clouds." In: *Journal of the Atmospheric Sciences* 81.9, pp. 1605–1616.

Kallis, G. et al. (2025). "Post-growth: the science of wellbeing within planetary boundaries." In: *The lancet planetary health* 9.1, e62–e78.

Khain, A. P. and M. Pinsky (2018). *Physical processes in clouds and cloud modeling*. Cambridge University Press.

Klein, S. A. and D. L. Hartmann (1993). "The seasonal cycle of low stratiform clouds." In: *Journal of Climate* 6.8, pp. 1587–1606.

Klein, S. A. et al. (2018). "Low-cloud feedbacks from cloud-controlling factors: A review." In: *Shallow clouds, water vapor, circulation, and climate sensitivity*, pp. 135–157.

Kopec, M. K., S. P. Malinowski, and Z. P. Piotrowski (2016). "Effects of wind shear and radiative cooling on the stratocumulus-topped boundary layer." In: *Quarterly Journal of the Royal Meteorological Society* 142.701, pp. 3222–3233.

Koshiro, T., H. Kawai, and A. T. Noda (2022). "Estimated cloud-top entrainment index explains positive low-cloud-cover feedback." In: *Proceedings of the National Academy of Sciences* 119.29, e2200635119.

Kotz, M., A. Levermann, and L. Wenz (2024). "The economic commitment of climate change." In: *Nature* 628.8008, pp. 551–557.

Krueger, S. K. (1993). "Linear eddy modeling of entrainment and mixing in stratus clouds." In: *Journal of Atmospheric Sciences* 50.18, pp. 3078–3090.

Kuo, H.-C. and W. H. Schubert (1988). "Stability of cloud-topped boundary layers." In: *Quarterly Journal of the Royal Meteorological Society* 114.482, pp. 887–916.

Kurowski, M., S. Malinowski, and W. Grabowski (2009). "A numerical investigation of entrainment and transport within a stratocumulus-topped boundary layer." In: *Quarterly Journal of the Royal Meteorological Society: A journal of the atmospheric sciences, applied meteorology and physical oceanography* 135.638, pp. 77–92.

Larson, V. E., K. E. Kotenberg, and N. B. Wood (2007). "An analytic longwave radiation formula for liquid layer clouds." In: *Monthly weather review* 135.2, pp. 689–699.

Latham, J. (1990). "Control of global warming?" In: *Nature* 347.6291, pp. 339–340.

Lebsock, M. D., G. L. Stephens, and C. Kummerow (2008). "Multisensor satellite observations of aerosol effects on warm clouds." In: *Journal of Geophysical Research: Atmospheres* 113.D15.

LeMone, M. A. et al. (2019). "100 years of progress in boundary layer meteorology." In: *Meteorological Monographs* 59, pp. 9–1.

Lilly, D. K. (1968). "Models of cloud-topped mixed layers under a strong inversion." In: *Quarterly Journal of the Royal Meteorological Society* 94.401, pp. 292–309.

Lozar, A. de and J.-P. Mellado (2014). "Cloud droplets in a bulk formulation and its application to buoyancy reversal instability." In: *Quarterly Journal of the Royal Meteorological Society* 140.682, pp. 1493–1504.

— (2015a). "Evaporative cooling amplification of the entrainment velocity in radiatively driven stratocumulus." In: *Geophysical Research Letters* 42.17, pp. 7223–7229.

— (2015b). "Mixing driven by radiative and evaporative cooling at the stratocumulus top." In: *Journal of the Atmospheric Sciences* 72.12, pp. 4681–4700.

— (2017). "Reduction of the entrainment velocity by cloud droplet sedimentation in stratocumulus." In: *Journal of the Atmospheric Sciences* 74.3, pp. 751–765.

Malinowski, S. P. et al. (2013). "Physics of Stratocumulus Top (POST): turbulent mixing across capping inversion." In: *Atmospheric Chemistry and Physics* 13.24, pp. 12171–12186.

Manavi, S. E. et al. (2025). "Atmospheric aerosol spatial variability: Impacts on air quality and climate change." In: *One Earth* 8.3.

Meehl, G. et al. (2020). *Context for interpreting equilibrium climate sensitivity and transient climate response from the CMIP6 Earth system models, Sci. Adv., 6, eaba1981.*

Mellado, J. P. (2010). "The evaporatively driven cloud-top mixing layer." In: *Journal of fluid mechanics* 660, pp. 5–36.

— (2017). "Cloud-top entrainment in stratocumulus clouds." In: *Annual Review of Fluid Mechanics* 49, pp. 145–169.

— (2025). *TLab.* URL: `https://github.com/turbulencia/tlab`.

Mellado, J. P. et al. (2018). "DNS and LES for simulating stratocumulus: Better together." In: *Journal of Advances in Modeling Earth Systems* 10.7, pp. 1421–1438.

Moeng, C.-H. et al. (1996). "Simulation of a stratocumulus-topped planetary boundary layer: Intercomparison among different numerical codes." In: *Bulletin of the American Meteorological Society* 77.2, pp. 261–278.

Moeng, C.-H. and R. Rotunno (1990). “Vertical-velocity skewness in the buoyancy-driven boundary layer.” In: *Journal of Atmospheric Sciences* 47.9, pp. 1149–1162.

Moin, P. and K. Mahesh (1998). “Direct numerical simulation: a tool in turbulence research.” In: *Annual review of fluid mechanics* 30.1, pp. 539–578.

Monin, A. S. and A. M. Yaglom (2013). *Statistical fluid mechanics, volume II: mechanics of turbulence*. Vol. 2. Courier Corporation.

Muhlbauer, A., I. L. McCoy, and R. Wood (2014). “Climatology of stratocumulus cloud morphologies: microphysical properties and radiative effects.” In: *Atmospheric Chemistry and Physics* 14.13, pp. 6695–6716.

Myers, T. A. et al. (2021). “Observational constraints on low cloud feedback reduce uncertainty of climate sensitivity.” In: *Nature Climate Change* 11.6, pp. 501–507.

NASA (2012). *A Glorious View - NASA Goddard Photo and Video*. URL: `https://www.flickr.com/photos/gsfc/7551317226`.

Neumann, P. et al. (2019). “Assessing the scales in numerical weather and climate predictions: will exascale be the rescue?” In: *Philosophical Transactions of the Royal Society A* 377.2142, p. 20180148.

Nicholls, S (1984). “The dynamics of stratocumulus: Aircraft observations and comparisons with a mixed layer model.” In: *Quarterly Journal of the Royal Meteorological Society* 110.466, pp. 783–820.

Nicholls, S and J. Turton (1986). “An observational study of the structure of stratiform cloud sheets: Part II. Entrainment.” In: *Quarterly Journal of the Royal Meteorological Society* 112.472, pp. 461–480.

Nuijens, L. and A. P. Siebesma (2019). “Boundary layer clouds and convection over subtropical oceans in our current and in a warmer climate.” In: *Current Climate Change Reports* 5, pp. 80–94.

OpenAI (2023). *ChatGPT: Large Language Model*. Version 4.1.

Orszag, S. A. and G. Patterson Jr (1972). “Numerical simulation of three-dimensional homogeneous isotropic turbulence.” In: *Physical review letters* 28.2, p. 76.

Ovchinnikov, M. et al. (2022). “Effects of horizontal resolution, domain size, boundary conditions, and surface heterogeneity on coarse LES of a convective boundary layer.” In: *Monthly Weather Review* 150.6, pp. 1397–1415.

Paluch, I. and D. Lenschow (1991). “Stratiform cloud formation in the marine boundary layer.” In: *Journal of Atmospheric Sciences* 48.19, pp. 2141–2158.

Payne, R. E. (1972). “Albedo of the sea surface.” In: *Journal of Atmospheric Sciences* 29.5, pp. 959–970.

Pincus, R. and M. B. Baker (1994). “Effect of precipitation on the albedo susceptibility of clouds in the marine boundary layer.” In: *Nature* 372.6503, pp. 250–252.

Pistor, R. (2025). “Resolving Droplet Sedimentation Effects in Stratocumulus Clouds.” In: (Version 3.0) [Dataset]. Edmond. URL: `https://doi.org/10.17617/3.9V1H4Y`.

Pistor, R. and J. P. Mellado (2025). “Resolving droplet sedimentation effects in stratocumulus clouds.” In: *Journal of Advances in Modeling Earth Systems* 17.8, e2025MS004966.

Possner, A. et al. (2020). “Deconvolution of boundary layer depth and aerosol constraints on cloud water path in subtropical stratocumulus decks.” In: *Atmospheric Chemistry and Physics* 20.6, pp. 3609–3621.

Pressel, K. G. et al. (2017). “Numerics and subgrid-scale modeling in large eddy simulations of stratocumulus clouds.” In: *Journal of advances in modeling earth systems* 9.2, pp. 1342–1365.

Qu, X. et al. (2015). “Positive tropical marine low-cloud cover feedback inferred from cloud-controlling factors.” In: *Geophysical Research Letters* 42.18, pp. 7767–7775.

Quaas, J. et al. (2022). “Robust evidence for reversal in the aerosol effective climate forcing trend.” In: *Atmospheric Chemistry and Physics Discussions* 2022, pp. 1–25.

Randall, D. et al. (1984). “Outlook for research on subtropical marine stratiform clouds.” In: *Bulletin of the American Meteorological Society* 65.12, pp. 1290–1301.

Randall, D. A. (1980). “Conditional instability of the first kind upside-down.” In: *Journal of Atmospheric Sciences* 37.1, pp. 125–130.

Rennert, K. et al. (2022). “Comprehensive evidence implies a higher social cost of CO2.” In: *Nature* 610.7933, pp. 687–692.

Richardson, L. F. (1920). “The supply of energy from and to atmospheric eddies.” In: *Proceedings of the Royal Society of London. Series A, Containing Papers of a Mathematical and Physical Character* 97.686, pp. 354–373.

Richter, I. (2015). “Climate model biases in the eastern tropical oceans: Causes, impacts and ways forward.” In: *Wiley Interdisciplinary Reviews: Climate Change* 6.3, pp. 345–358.

Rogallo, R. S. and P. Moin (1984). “Numerical simulation of turbulent flows.” In: *Annual review of fluid mechanics* 16, pp. 99–137.

Rosenfeld, D. et al. (2019). “Aerosol-driven droplet concentrations dominate coverage and water of oceanic low-level clouds.” In: *Science* 363.6427, eaav0566.

Sandu, I. et al. (2008). “Aerosol impacts on the diurnal cycle of marine stratocumulus.” In: *Journal of the Atmospheric Sciences* 65.8, pp. 2705–2718.

Satoh, M. et al. (2019). “Global cloud-resolving models.” In: *Current Climate Change Reports* 5.3, pp. 172–184.

Savic-Jovcic, V. and B. Stevens (2008). “The structure and mesoscale organization of precipitating stratocumulus.” In: *Journal of the Atmospheric Sciences* 65.5, pp. 1587–1605.

Schalkwijk, J. et al. (2015). “Weather forecasting using GPU-based large-eddy simulations.” In: *Bulletin of the American Meteorological Society* 96.5, pp. 715–723.

Schär, C. et al. (2020). “Kilometer-scale climate models: Prospects and challenges.” In: *Bulletin of the American Meteorological Society* 101.5, E567–E587.

Schiro, K. A. et al. (2022). “Model spread in tropical low cloud feedback tied to overturning circulation response to warming.” In: *Nature Communications* 13.1, p. 7119.

Schlemmer, L. and C. Hohenegger (2014). “The formation of wider and deeper clouds as a result of cold-pool dynamics.” In: *Journal of the Atmospheric Sciences* 71.8, pp. 2842–2858.

Schneider, T., C. M. Kaul, and K. G. Pressel (2019). “Possible climate transitions from breakup of stratocumulus decks under greenhouse warming.” In: *Nature Geoscience* 12.3, pp. 163–167.

Schulz, B. and J. P. Mellado (2018). "Wind shear effects on radiatively and evaporatively driven stratocumulus tops." In: *Journal of the Atmospheric Sciences* 75.9, pp. 3245–3263.

— (2019). "Competing effects of droplet sedimentation and wind shear on entrainment in stratocumulus." In: *Journal of Advances in Modeling Earth Systems* 11.6, pp. 1830–1846.

Schween, J. H. et al. (2022). "Life cycle of stratocumulus clouds over 1 year at the coast of the Atacama Desert." In: *Atmospheric Chemistry and Physics* 22.18, pp. 12241–12267.

Scott, R. C. et al. (2020). "Observed sensitivity of low-cloud radiative effects to meteorological perturbations over the global oceans." In: *Journal of Climate* 33.18, pp. 7717–7734.

Shaw, R. A. (2003). "Particle-turbulence interactions in atmospheric clouds." In: *Annual Review of Fluid Mechanics* 35.1, pp. 183–227.

Sherwood, S. C., S. Bony, and J.-L. Dufresne (2014). "Spread in model climate sensitivity traced to atmospheric convective mixing." In: *Nature* 505.7481, pp. 37–42.

Sherwood, S. C. et al. (2020). "An assessment of Earth's climate sensitivity using multiple lines of evidence." In: *Reviews of Geophysics* 58.4, e2019RG000678.

Shima, S.-i. et al. (2009). "The super-droplet method for the numerical simulation of clouds and precipitation: A particle-based and probabilistic microphysics model coupled with a non-hydrostatic model." In: *Quarterly Journal of the Royal Meteorological Society: A journal of the atmospheric sciences, applied meteorology and physical oceanography* 135.642, pp. 1307–1320.

Siebesma, A. P. et al. (2020). *Clouds and climate: Climate science's greatest challenge.* Cambridge University Press.

Soden, B. J. and I. M. Held (2006). "An assessment of climate feedbacks in coupled ocean–atmosphere models." In: *Journal of climate* 19.14, pp. 3354–3360.

Stevens, B. (2005). "Atmospheric moist convection." In: *Annu. Rev. Earth Planet. Sci.* 33, pp. 605–643.

Stevens, B. and G. Feingold (2009). "Untangling aerosol effects on clouds and precipitation in a buffered system." In: *Nature* 461.7264, pp. 607–613.

Stevens, B. et al. (1998). "Large-eddy simulations of strongly precipitating, shallow, stratocumulus-topped boundary layers." In: *Journal of the atmospheric sciences* 55.24, pp. 3616–3638.

Stevens, B. et al. (2003). "On entrainment rates in nocturnal marine stratocumulus." In: *Quarterly Journal of the Royal Meteorological Society: A journal of the atmospheric sciences, applied meteorology and physical oceanography* 129.595, pp. 3469–3493.

Stevens, B. et al. (2005). "Evaluation of large-eddy simulations via observations of nocturnal marine stratocumulus." In: *Monthly weather review* 133.6, pp. 1443–1462.

Stevens, D. et al. (2000). "Small-scale processes and entrainment in a stratocumulus marine boundary layer." In: *Journal of the atmospheric sciences* 57.4, pp. 567–581.

Stevens, D. and C. Bretherton (1999). "Effects of resolution on the simulation of stratocumulus entrainment." In: *Quarterly Journal of the Royal Meteorological Society* 125.554, pp. 425–439.

Tillman, J. (1972). "The indirect determination of stability, heat and momentum fluxes in the atmospheric boundary layer from simple scalar variables during dry unstable conditions." In: *Journal of Applied Meteorology and Climatology* 11.5, pp. 783–792.

Toll, V. et al. (2019). "Weak average liquid-cloud-water response to anthropogenic aerosols." In: *Nature* 572.7767, pp. 51–55.

Twomey, S. (1974). "Pollution and the planetary albedo." In: *Atmospheric Environment (1967)* 8.12, pp. 1251–1256. ISSN: 0004-6981. DOI: `https://doi.org/10.1016/0004-6981(74)90004-3`. URL: `https://www.sciencedirect.com/science/article/pii/0004698174900043`.

Twomey, S. (1977). "The influence of pollution on the shortwave albedo of clouds." In: *Journal of Atmospheric Sciences* 34.7, pp. 1149–1152.

Vecchi, G. A. and B. J. Soden (2007). "Global warming and the weakening of the tropical circulation." In: *Journal of Climate* 20.17, pp. 4316–4340.

Wang, Q. and B. A. Albrecht (1994). "Observations of cloud-top entrainment in marine stratocumulus clouds." In: *Journal of Atmospheric Sciences* 51.11, pp. 1530–1547.

Wang, S., Q. Wang, and G. Feingold (2003). "Turbulence, condensation, and liquid water transport in numerically simulated nonprecipitating stratocumulus clouds." In: *Journal of the atmospheric sciences* 60.2, pp. 262–278.

Webb, M. J. et al. (2006). "On the contribution of local feedback mechanisms to the range of climate sensitivity in two GCM ensembles." In: *Climate dynamics* 27.1, pp. 17–38.

Williams, A. S. and A. L. Igel (2021). "Cloud Top Radiative Cooling Rate Drives Non-Precipitating Stratiform Cloud Responses to Aerosol Concentration." In: *Geophysical Research Letters* 48.18, e2021GL094740.

Wood, R. (2007). "Cancellation of aerosol indirect effects in marine stratocumulus through cloud thinning." In: *Journal of the atmospheric sciences* 64.7, pp. 2657–2669.

— (2012). "Stratocumulus clouds." In: *Monthly weather review* 140.8, pp. 2373–2423.

— (2021). "Assessing the potential efficacy of marine cloud brightening for cooling Earth using a simple heuristic model." In: *Atmospheric Chemistry and Physics Discussions* 2021, pp. 1–52.

Wyngaard, J. C. (2010). *Turbulence in the Atmosphere*. Cambridge university press.

Xue, H. and G. Feingold (2006). "Large-eddy simulations of trade wind cumuli: Investigation of aerosol indirect effects." In: *Journal of the atmospheric sciences* 63.6, pp. 1605–1622.

Yamaguchi, T. and D. A. Randall (2008). "Large-eddy simulation of evaporatively driven entrainment in cloud-topped mixed layers." In: *Journal of the Atmospheric Sciences* 65.5, pp. 1481–1504.

— (2012). "Cooling of entrained parcels in a large-eddy simulation." In: *Journal of the Atmospheric Sciences* 69.3, pp. 1118–1136.

Yin, C. et al. (2024). “Simulation of marine stratocumulus using the super-droplet method: numerical convergence and comparison to a double-moment bulk scheme using SCALE-SDM 5.2. 6-2.3. 1.” In: *Geoscientific Model Development* 17.13, pp. 5167–5189.

Zelinka, M. D. et al. (2020). “Causes of higher climate sensitivity in CMIP6 models.” In: *Geophysical Research Letters* 47.1, e2019GL085782.

Eidesstattliche Versicherung
Declaration on Oath

Hiermit erkläre ich an Eides statt, dass ich die vorliegende Dissertationsschrift selbst verfasst und keine anderen als die angegebenen Quellen und Hilfsmittel benutzt habe. Sofern im Zuge der Erstellung der vorliegenden Dissertationsschrift generative Künstliche Intelligenz (gKI) basierte elektronische Hilfsmittel verwendet wurden, versichere ich, dass meine eigene Leistung im Vordergrund stand und dass eine vollständige Dokumentation aller verwendeten Hilfsmittel gemäß der Guten wissenschaftlichen Praxis vorliegt. Ich trage die Verantwortung für eventuell durch die gKI generierte fehlerhafte oder verzerrte Inhalte, fehlerhafte Referenzen, Verstöße gegen das Datenschutz- und Urheberrecht oder Plagiate.

I hereby declare and affirm that this doctoral dissertation is my own work and that I have not used any aids and sources other than those indicated. If electronic resources based on generative artificial intelligence (gAI) were used in the course of writing this dissertation, I confirm that my own work was the main and value-adding contribution and that complete documentation of all resources used is available in accordance with good scientific practice. I am responsible for any erroneous or distorted content, incorrect references, violations of data protection and copyright law or plagiarism that may have been generated by the gAI.

Hamburg, September 29, 2025

Raphael Pistor

ERKLÄRUNG

Ich versichere, dass dieses gebundene Exemplar der Dissertation und das in elektronischer Form eingereichte Dissertationsexemplar (über den Docata-Upload) und das bei der Fakultät zur Archivierung eingereichte gedruckte gebundene Exemplar der Dissertationsschrift identisch sind.

I, the undersigned, declare that this bound copy of the dissertation and the dissertation submitted in electronic form (via the Docata upload) and the printed bound copy of the dissertation submitted to the faculty (responsible Academic Office or the Doctoral Office Physics) for archiving are identical.

Hamburg, September 29, 2025

Raphael Pistor

Hinweis / Reference

Die gesamten Veröffentlichungen in der Publikationsreihe des MPI-M
„Berichte zur Erdsystemforschung / Reports on Earth System Science“,
ISSN 1614-1199

sind über die Internetseiten des Max-Planck-Instituts für Meteorologie erhältlich:
https://mpimet.mpg.de/forschung/publikationen

All the publications in the series of the MPI -M
„Berichte zur Erdsystemforschung / Reports on Earth System Science“,
ISSN 1614-1199

are available on the website of the Max Planck Institute for Meteorology:
https://mpimet.mpg.de/en/research/publications